

**EXPERIMENTAL AND NUMERICAL INVESTIGATION
OF MULTIPHASE FLOW CHARACTERISTICS IN T-
SHAPED MICROCHANNELS**

Thesis

Submitted in partial fulfilment of the requirements for the degree of

DOCTOR OF PHILOSOPHY

By

VENKATA SAI TEJA MADANA

(Registration No: 177069CH001)



DEPARTMENT OF CHEMICAL ENGINEERING
NATIONAL INSTITUTE OF TECHNOLOGY KARNATAKA,
SURATHKAL, MANGALURU - 575025

November 2024

DECLARATION

I hereby *declare* that the Research Thesis entitled “**Experimental and Numerical Investigation of Multiphase Flow Characteristics in T-shaped Microchannels**” which is being submitted to the National Institute of Technology Karnataka, Surathkal in partial fulfillment of the requirements for the award of the Degree of **Doctor of Philosophy** in the **Department of Chemical Engineering**, is a *bonafide report of the research work carried out by me*. The material contained in this Research Thesis has not been submitted to any University or Institution for the award of any degree.

V. U. Smita

VENKATA SAI TEJA MADANA

Registration No: 177069CH001

Department of Chemical Engineering

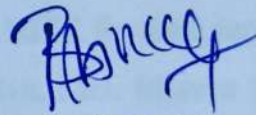
NITK Surathkal

Place: Surathkal

Date: *04-11-2024*

CERTIFICATE

This is to certify that the Research Thesis entitled "Experimental and Numerical Investigation of Multiphase Flow Characteristics in T-shaped Microchannels" submitted by Mr. Venkata Sai Teja Madana (Registration No: 177069CH001) as the record of the research work carried out by him, is *accepted as the Research Thesis submission* in partial fulfilment of the requirements for the award of the degree of Doctor of Philosophy.



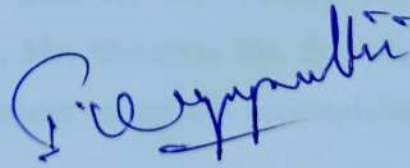
Research Guide

Dr. B. Ashraf Ali

Associate Professor

Dept. of Chemical Engineering

NITK, Surathkal



Chairman- DRPC

Dr. I. Regupathi

Professor & HOD

Dept. of Chemical Engineering

NITK, Surathkal

Head of the Department

विभागाध्यक्ष

Department of Chemical Engineering

रासायनिक अभियांत्रिकी विभाग

National Institute of Technology Karnataka - Surathkal

राष्ट्रीय प्रौद्योगिकी संस्थान कर्नाटक, सुगत्कल

PO Srinivasnagar, Mangalore - 575025 Karnataka

पी.ओ. श्रीनिवासनगर, मंगलौर - ५७५०२५ कर्नाटक

ACKNOWLEDGEMENTS

First and foremost, I express my heartfelt thanks and gratitude to my Research Supervisor, **Dr. B Ashraf Ali** for his invaluable guidance and constant support without which I could not have finished my Research work. In addition to the technical guidance, his constant motivation, compassion and encouragement were behind the successful completion of my PhD thesis. I am extremely thankful to Research Progress Assessment Committee Members, **Prof. Vidya Shetty K**, Department of Chemical Engineering, NITK and **Dr. Anish S**, Department of Mechanical Engineering, NITK, for their valuable insights and critical suggestions, which strengthened my research work.

I express my sincere gratitude to the **Director**, NITK Surathkal for providing me the funds to carry out this research work. I wish to thank **Prof. I Regupathi**, Head of the Department, Chemical Engineering, **Prof. Raj Mohan B** (Former H.O.D), **Prof. Hari Mahalingam** (Former H.O.D), **Prof. Prasanna B D** (Former H.O.D) and **Prof. Jagadeeshbabu P E** (Former H.O.D) for providing me necessary facilities, funding and support during my Ph.D. I would also like to thank all the faculty members of the Department of Chemical Engineering, NITK for their support and encouragement. I would also like to acknowledge Mr. Sadashiva, Mrs. Bhavya Shree, Mrs. Vijetha, Mr. Suresh, Mrs. Sandhya and all other non-teaching staff for their support during my research.

I would like to express my gratitude to my senior, **Dr. Lister H Falleiro** for his invaluable support and guidance during my research. The expertise shared by him had helped me in successfully completing my research work. I would also like to thank **Bharathesh, Manish B, Sriniketh A, Santhosh, Sunil Kumar, Arnab Roy, Sujay S, Muskan P, Karthika B, Dr. Kishore, Dr. Vishnu M, Dr. Shankramma, Dr. Deekshitha, Dr. Rohit Kalnake, Mr. Shourya, Ms. Sophia, Mr. Suyash Harsh, Mr. Ramesh P** and all my friends without whom this accomplishment would not have been possible.

Finally, I lovingly acknowledge my family for their invaluable support and cooperation during this successful journey of my Ph.D. I am grateful for the trust they have in me.

J. V. Smitij

VENKATA SAI TEJA MADANA

Dedicated

To

My Mother and Father

ABSTRACT

Microfluidics play an essential role in process intensification. These devices facilitate safe environment for reaction, better process control, high heat and mass transfer rates. The performance of these devices depend on the flow behaviour, flow regimes, macro and micromixing. Hence, in this work, the hydrodynamics, macro mixing, single-phase flow regimes, micromixing and crystallization in the T-shaped microchannel are investigated numerically and experimentally. First, the hydrodynamics and macro mixing in the microchannel are predicted using CFD simulations and are validated with experiments. To improve the flow field and macro mixing, rectangular and trapezoidal baffle configurations are introduced in the flow channel. The macro mixing in the microchannel is characterized through Residence Time Distribution (RTD). The extent of axial and lateral mixing are quantified to find an optimum baffle configuration that supports flow field and macro mixing in T-shaped microchannel. As introduction of these baffles in the flow channel induces higher pressure drop, various single phase flow regimes in T-shaped microchannel are identified in terms of flow Reynolds number. In engulfment flow regime, mixing is found to be high and this flow regime occurs when flow Reynolds number is 300. To obtain engulfment flow regime at low Re (75) convergent – divergent inlets are proposed. The extent of macro mixing at different flow regimes are numerically quantified by injecting buoyant tracer particles and computing their trajectories through Lagrangian approach. This is qualitatively analyzed through Poincarè maps and quantified with Shannon's entropy. The role of micromixing on reaction between 1-naphthol and di-azotized sulphanilic acid is numerically analyzed for different flow regimes. The micromixing performance is found to be low in vortex flow regime and high in engulfment flow regime. The extent of micromixing is found to be superior when convergent – divergent inlets (C:D = 9:1) are introduced. As an application study, antisolvent crystallization of NaCl is considered in the microchannel. The crystal size distribution (CSD) and growth are predicted using Population Balance Model (PBM). The crystal growth and CSD are predicted using discrete method of PBM. The CSD is found to be narrow when flow Reynolds number increases. To improve crystal growth, CSD and crystal yield, various dosing modes are proposed and optimum conditions are

identified (phase lag = 180° , frequency = 20 Hz, amplitude = 0.05 m/s) for high crystal yield and narrow CSD.

Keywords: Microchannel, Hydrodynamics, Engulfment flow regime, Micromixing, Antisolvent crystallization, CFD, Population Balance Model (PBM)

NOMENCLATURE

B	nucleation rate ($\#/m^3$)
c	tracer concentration ($kmol/m^3$)
C_{avg}	tracer concentration under fully mixed condition ($kmol/m^3$)
C_i	tracer concentration in i^{th} element ($kmol/m^3$)
C*	solubility of NaCl in water-ethanol mixture (g/100g of water)
C	concentration of NaCl (g/100g of water)
C_{A0}	initial concentration of reactant A at the inlet ($kmol/m^3$)
C_D	drag coefficient
C_R	concentration of product R ($kmol/m^3$)
C_S	concentration of product S ($kmol/m^3$)
D	diffusivity of the tracer (m^2/s)
d_p	diameter of buoyant particles (m)
E(θ)	normalized exit age distribution
F_D	drag force per unit mass (m/s^2)
F_x	external force acting on the particle per unit mass (m/s^2)
F_{d,j}	drag force on j^{th} phase (m/s^2)
G	growth rate (m/s)
G_V	growth rate based on crystal volume (m/s)
\vec{J}_i	diffusive mass flux of species i, ($kg/m^2.s$)
k₁	rate constant of reaction - 1 (l/mol.s)
k₂	rate constant of reaction – 2 (l/mol.s)
k_{ls}	interphase momentum exchange coefficient
k_v	volumetric shape factor

L	size of the crystal (m)
m	mass fraction of ethanol in solvent mixture
\dot{m}_{jk}	interphase mass exchange (mol/s)
MI	mixing index
M	number of bins
N	number of elements
$n(V, t)$	number density of crystals with volume V at time t ($\#/m^3$)
n_v	initial number density of crystals ($\#/m^3$)
P	total number of discrete phase particles
Pe	Peclet number
p	pressure (Pa)
p_s	solid pressure (Pa)
p_k	probability of finding particles in k^{th} bin
R_{jk}	interphase force exchange (m/s^2)
r_i	rate of generation of species i due to reaction (mol/l.s)
Re	Reynolds number
S	Shannon's Entropy
Se	Selectivity of desired product R over undesired product S
SS	relative super saturation
s_i	rate of addition of species i from bulk fluid (mol/l.s)
t	time (s)
\mathbf{u}_j	velocity of j^{th} phase (m/s)
u	fluid velocity (m/s)
\mathbf{u}_p	particle velocity (m/s)

x_k number of particles in k^{th} bin

X_i mass fraction of species i

Y yield of desired product R

Greek letters

α_j volume fraction of j^{th} phase

Γ liquid circulation rate (mm^2/s)

ρ fluid density (kg/m^3)

ρ_j density of j^{th} phase (kg/m^3)

ρ_p density of the tracer particles (kg/m^3)

σ standard deviation

σ_θ time normalized standard deviation

τ mean residence time (s)

μ fluid viscosity (Pa.s)

ν kinematic viscosity of the fluid (m^2/s)

TABLE OF CONTENTS

ABSTRACT.....	i
NOMENCLATURE	iii
LIST OF FIGURES	xi
LIST OF TABLES	xv
1. INTRODUCTION.....	1
1.1. Background	1
1.2. Types of Microchannels	1
1.3. Materials for Fabrication.....	2
1.4. Applications of Microchannels	4
1.4.1. Chemical Synthesis.....	4
1.4.2. Liquid-Liquid Extraction	4
1.4.3. Nanoparticle Synthesis.....	5
1.5. Importance of CFD.....	6
2. LITERATURE REVIEW	7
2.1. Hydrodynamics and Mixing in Microchannels.....	7
2.2. Single-Phase Flow Regimes in Microchannels.....	10
2.3. Micromixing in Microchannels.....	12
2.4. Crystallization in Microchannels	12
3. SCOPE AND OBJECTIVES OF THE WORK	15
3.1. Scope.....	15

3.2. Objectives	15
3.3. Organization of Thesis	16
4. RESEARCH METHODOLOGY	17
4.1. Geometry.....	17
4.2. Experimental Methodology	18
4.2.1. Experimental Setup.....	18
4.2.3. Experimental Procedure.....	18
4.3. Computational Methodology	19
4.3.1. Transport equations.....	19
4.3.2. Simulation Setup.....	24
5. RESULTS AND DISCUSSION.....	27
5.1. Grid & Time Independence Studies	27
5.2. Hydrodynamics & Mixing	29
5.2.1. Hydrodynamics	29
5.2.2. Mixing.....	31
5.2.3. Reaction	39
5.3. Single Phase Flow Regimes	41
5.3.1. Flow Regimes	41
5.3.2. Inlet Modifications.....	45
5.3.2. Poincaré and Shannon's Entropy	48
5.4. Micromixing in T-shaped Microchannels	52

5.4.1.	Effect of Reynolds number on Micromixing	52
5.4.2.	Effect of Inlet Modifications on Micromixing.....	54
5.4.3.	Fluid Particle Interactions	59
5.5.	Antisolvent Crystallization.....	61
5.5.1.	Effect of Reynolds Number	62
5.5.2.	Antisolvent Dosing	70
6.	SUMMARY AND CONCLUSIONS	75
6.1.	Future Scope.....	767
	REFERENCES	79
	APPENDIX – I	91
	APPENDIX – II	95
	RESEARCH OUTCOME.....	99
	SCI – Indexed Journal Publications	99
	Conferences.....	99
	BIODATA.....	101

LIST OF FIGURES

Figure 1.1 Different types of microchannels reported in literature. (a) T-junction microchannel , (b) Y-junction microchannel, (c) cross junction microchannel, (d) serpentine microchannel and (e) split and recombine microchannel (Bhagat et al., 2007; Zhang et al., 2017)	2
Figure 2.1. Passive mixing techniques in microchannels (Lee et al. 2011b).....	7
Figure 2.2 Schematics of various passive mixing techniques in microchannels. (a) Lamination type channels, (b) intersecting channels, (c) zig-zag channels, (d) serpentine channels, (e) embedded obstacles, (f) split & recombine channels and (g) twisted channels. (Lee et al. 2011a; Cai et al. 2017)	8
Figure 2.3. Active mixing techniques in microchannels (Lee et al. 2011b)	9
Figure 2.4. Tracer concentration at the centre plane of microchannel for (a) Stratified flow (Re = 50), (b) Vortex flow (Re = 120) and (c) Engulfment flow (Re = 160).....	11
Figure 2.5. Antisolvent Crystallization of NaCl in Water-Ethanol mixture	13
Figure 4.1. (a) Schematic of T-shaped Microchannel and (b) Microchannel fabricated in PMMA.	17
Figure 4.2 Experimental setup. (1) high speed microscope camera, (2) microscope, (3) microchannel, (4) syringe infusion pumps and (5) computer	18
Figure 5.1. Velocity profile near the outlet for various grid sizes	27
Figure 5.2 Temporal variation of velocity magnitude at a point (x = 0 μm , y = 100 μm , z = 0 μm) for different Δt	28
Figure 5.3 Contours of velocity magnitude for Re = 20. (a) t = 0 s, (b) t = 0.001 s, (c) t = 0.15 s and (d) t = 1 s	29
Figure 5.4 Streamlines of velocity magnitude Re = 20. (a) t = 0 s, (b) t = 0.001 s, (c) t = 0.15 s and (d) t = 1 s	29

Figure 5.5 Spatial variation of velocity magnitude along a horizontal line ($x = 30$ mm, $y = 0.1$ mm and $Re = 1$)	30
Figure 5.6 Effect of Reynolds number on liquid circulation rate	31
Figure 5.7 Effect of Re on mixing index	32
Figure 5.8 Schematic of proposed geometric modifications with (a) consecutive side baffles, B1 (b) alternate trapezoidal baffles, B2	32
Figure 5.9 Contours of Velocity Magnitude for different baffle configurations	33
Figure 5.10 Effect of baffle configurations on Pressure drop.....	34
Figure 5.11 Effect of baffle configurations on Liquid Circulation.....	34
Figure 5.12 Effect of various baffle configurations on normalized RTD function	35
Figure 5.13 Effect of Reynolds number on mixing index for various geometric configurations	37
Figure 5.14 Contours of mass fraction of tracer along the length of the microchannel for $Re = 20$	38
Figure 5.15 Temporal variation of NaOH conversion for various baffle configurations	39
Figure 5.16 Effect of baffle configuration on conversion of NaOH.....	40
Figure 5.17. Contours of normalized velocity magnitude for (a) stratified flow regime ($Re = 20$), (b) vortex flow regime ($Re = 100$) and (c) engulfment flow regime ($Re = 300$).....	41
Figure 5.18. Streamlines and vectors corresponding to (a) stratified flow regime, (b) vortex flow regime and (c) engulfment flow regime	42
Figure 5.19 Spatial variation of tracer at T-junction for different flow regimes (a) Simulation and (b) Experiment.....	43
Figure 5.20 Effect of flow regimes on mixing index.....	43

Figure 5.21 Contours of tracer mass fraction at different flow regimes near the entrance and exit of the microchannel.....	44
Figure 5.22 Schematic of proposed geometric modifications at the microchannel inlet. (C – convergent section length, D – divergent section length and T – throat width) ..	45
Figure 5.23 Streamlines and vectors corresponding to (a) without modification, (b) C/D = 1:1, (c) C/D = 3:1 and (d) C/D = 9:1 at Re = 75.....	47
Figure 5.24 Spatial variation of tracer at different flow regimes for modified inlet configuration (C:D = 9:1). (a) Simulation and (b) Experiment	47
Figure 5.25 The effect of convergent – divergent inlets on mixing index.....	49
Figure 5.26 Poincaré map in the engulfment region for (a) no modification, (b) C/D = 1:1, (c) C/D = 3:1 and (d) C/D = 9:1	50
Figure 5.27 (a) Contours of normalized vorticity at a horizontal plane ($y = 100 \mu\text{m}$) and (b) contours of normalized vorticity along with velocity vectors at a vertical plane ($x = 100 \mu\text{m}$) near the entrance of the microchannel for different flow regimes	52
Figure 5.28 Effect of flow regimes on selectivity and percentage yield of R	53
Figure 5.29 Contours of normalized vorticity at a horizontal plane ($y = 100 \mu\text{m}$) for (a) microchannel without modification and (b) microchannel with 9:1 convergent divergent inlets.....	54
Figure 5.30 Contours of normalized vorticity along with velocity vectors at a vertical plane ($x = 100 \mu\text{m}$) near the entrance of the microchannel for (a) microchannel without modification and (b) microchannel with 9:1 convergent divergent inlets	55
Figure 5.31 Comparison of pressure drop (a) and liquid circulation rate (b) at the entrance for microchannel without modification and with 9:1 convergent - divergent inlets.....	56

Figure 5.32 Comparison of selectivity and yield of R for microchannel without modification and with 9:1 Convergent - Divergent inlets	57
Figure 5.33 Effect of reactant molar ratio on (a) selectivity and (b) yield of R	58
Figure 5.34 Effect of flow regimes on collision rate of buoyant fluid particles in the microchannel.....	59
Figure 5.35 Crystal size distribution for various grid sizes (in μm).	61
Figure 5.36 Solubility of NaCl in Water-Ethanol Mixture	62
Figure 5.37 Contours of NaCl mass fraction at different Reynolds numbers at $y = 100 \mu\text{m}$ (top) and $x = 100 \mu\text{m}$ (bottom).....	63
Figure 5.38 Effect of C-D inlets on crystal size distribution	63
Figure 5.39 Effect of Re on crystal size distribution	65
Figure 5.40 The effect of Re on (a) nucleation rate and (b) growth rate	66
Figure 5.41 Effect of Re on pressure drop and crystal yield	67
Figure 5.42 Contours of NaCl supersaturation for various ethanol mass fractions at $y = 100 \mu\text{m}$. (a) 1, (b) 0.9, (c) 0.8, (d) 0.7 and (e) 0.6.....	68
Figure 5.43 Effect of antisolvent mass fraction on crystal size distribution.....	68
Figure 5.44 Effect of ethanol mass fraction on (a) nucleation rate and (b) growth rate	69
Figure 5.45 The effect of (a) phase lag and (b) frequency of pulse on CSD	71
Figure 5.46 The effect of amplitude (m/s) of pulse on CSD	72
Figure 5.47 The effect of Re on (a) CSD; (b) crystal yield and mean crystal size at optimum pulse flow conditions.....	73

LIST OF TABLES

Table 1.1 Various Materials used for Fabrication of Microchannels	3
Table 1.2 Synthesis of nanoparticles in Microchannels.....	5
Table 2.1 Crystallization in microchannels	14
Table 5.1 Maximum velocity achieved for different grid sizes	28
Table 5.2 Effect of baffle configurations on mean residence time, variance and Pe...36	
Table 5.3 Flow regimes present in the T-shaped microchannel	41
Table 5.4. Effect of geometric modifications on $Re_{critical}$ and pressure drop	46
Table 5.5. Effect of geometric modifications on pressure drop and Shannon's entropy	48
Table 5.6 Flow regimes in the modified microchannel configuration (C:D = 9:1)	54
Table 5.7 Effect of reactant molar ratio on Selectivity and Conversion of R.....	58
Table 5.8 Crystal yield and mean crystal size for various grid sizes.	61
Table 5.9 Effect of C-D inlets on mean crystal size and yield	64
Table 5.10 Effect of Reynolds number on crystal size distribution.....	65
Table 5.11 Effect of antisolvent mass fraction on crystal size distribution	69
Table 5.12 Effect of phase lag between inlet pulses on mean crystal size and yield...70	
Table 5.13 Effect of frequency of inlet pulses on mean crystal size and yield.....	70
Table 5.14 Effect of amplitude of pulse flow on mean crystal size and yield.....	72

1. INTRODUCTION

1.1. Background

Process Intensification (PI) through different methods has found many applications in chemical process industries. The enhancement of heat and mass transfer rates, cost reduction through innovative processes, safety in dealing with highly exothermic reactions have been made possible by PI through miniaturisation in process industries. In the chemical process industry, this is desirable as it enables a reduction in inventory and thereby helps in the safe operation of chemical plants. Microfluidic systems are one of the solutions generated by the intensification of reactor design. Microfluidic systems because of their small dimensions have a high surface to volume ratio that helps in improving heat and mass transfer rates significantly. This lead to lot of research activity in understanding flow behaviour in microfluidic systems.

Microfluidic devices have dimensions in the range of 10 μm – 1000 μm (Kandlikar and Grande 2003; Kockmann 2008; Mehendale et al. 2000). These low dimensions offer various advantages over conventional type reactors notably better control of the process (Burns and Ramshaw 1999), energy efficient and usage of less chemicals (Kashid and Kiwi-Minsker 2009), small sized analysis systems, on-site synthesis of chemicals and easy scale up by using multiple devices in parallel (Voloshin et al. 2007). Due to these advantages microfluidics have found many applications in micro total analysis systems, lab-on-chip applications, micromixers, liquid-liquid extraction, microbubble columns, microdroplet generators and microreactors.

The smaller hydraulic diameter and comparatively low flow rates in the microchannel leads to a meager Reynolds number sometimes even less than one, which makes the flow highly viscous dominated leading to a laminar flow field. Since the flow is in the laminar regime, transport of species is driven by molecular diffusion only (a slow process).

1.2. Types of Microchannels

Different types of microchannels were designed and studied by the researchers. The most commons type of microchannels are straight (Javaid Afzal et al., 2022), T-junction (van der Graaf et al., 2006), Y-junction (Hu et al., 2008), arrow shaped (Aoki

et al., 2013), cross junction (Nisisako and Torii, 2008), spiral (Bhagat et al., 2008) and serpentine microchannels (Javaid et al., 2018). The schematics of these microchannel types are depicted in Figure 1.1.

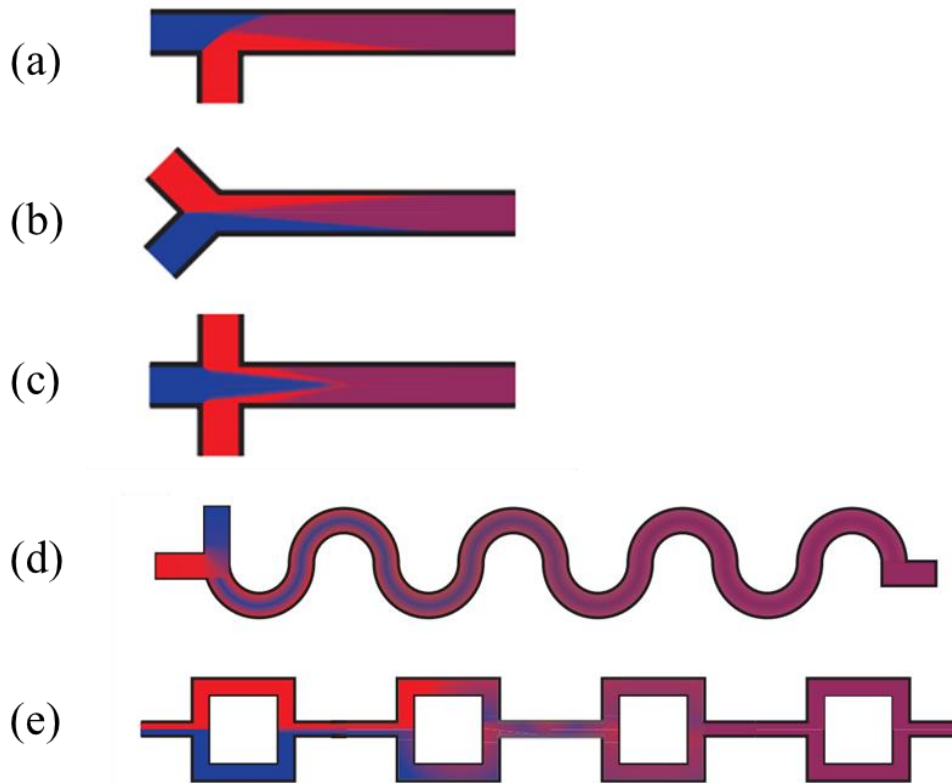


Figure 1.1 Different types of microchannels reported in literature. (a) T-junction microchannel , (b) Y-junction microchannel, (c) cross junction microchannel, (d) serpentine microchannel and (e) split and recombine microchannel (Bhagat et al., 2007; Zhang et al., 2017)

1.3. Materials for Fabrication

Microchannels can be fabricated using a wide range of materials like glass, silicon, polymers, paper and metals (Jensen, 2017; Suryawanshi et al., 2018; Nishat et al., 2021). The selection of materials depends on operating conditions, physical properties of working fluids, throughput of products, ease of fabrication and cost (Suryawanshi et al., 2018). The advantages and disadvantages of various materials used for microchannel fabrication are listed in Table 1.1 (Suryawanshi et al., 2018; Nishat et al., 2021).

Table 1.1 Various Materials used for Fabrication of Microchannels

Material	Advantages	Disadvantages
Glass	<ul style="list-style-type: none"> • Cheap • Visualization of flow • Withstands high operating pressures • Superior chemical compatibility 	<ul style="list-style-type: none"> • Difficult to make high aspect ratio channels • Difficult to make complex geometric structures
Silicon	<ul style="list-style-type: none"> • High precision milling is possible • Ease of fabrication • Chemical & thermal compatibility 	<ul style="list-style-type: none"> • Requirement of clean room • Expensive fabrication methods
Polymers	<ul style="list-style-type: none"> • Cheap • Multiple options of polymers • Easy fabrication techniques • Disposable microchannels can be made • Ease of making complex geometric structures 	<ul style="list-style-type: none"> • Limited chemical compatibility • Can't be used for high temperature applications
Paper	<ul style="list-style-type: none"> • Very cheap • Easy fabrication techniques 	<ul style="list-style-type: none"> • Only disposable microchannels are possible • High aspect ratio channels are not possible • Variable porosity of channel
Metals	<ul style="list-style-type: none"> • Durable • Easy fabrication techniques • Better thermal compatibility 	<ul style="list-style-type: none"> • Not compatible with all solvents • Flow can't be visualized

1.4. Applications of Microchannels

Microchannels due to their small dimensions and high surface to volume ratio have several chemical, pharmaceutical and biological applications (Yao et al., 2015). Some of the applications are total analysis systems, antibody detection chips, nanomaterial synthesis, on-site chemical synthesis etc.

1.4.1. Chemical Synthesis

In chemical industries, microchannels can be used for the synthesis of speciality chemicals (Floyd et al., 2000), organic compounds (Fletcher et al., 2002) and pharmaceutical assays (Maeki, 2019). Highly efficient catalytic reactions can be performed in microchannels due to their huge interfacial areas (Mawatari et al., 2012). Hisamoto et al. (2001) performed a phase-transfer synthesis in a microchannel and achieved close to 100% conversion with a residence time of 2.3 seconds compared to 80% conversion with one-hour residence time in conventional reactors. Kobayashi et al. (2004) performed catalyzed hydrogenation reaction in microchannels with reaction times of 2 min. El Zanati et al. (2017) used microreactors to perform esterification reaction of 2- ethyl hexanoic acid and achieved conversions greater than 99% without the help of a catalyst. Wang et al. (2022) developed an advanced flow reactor for continuous production of 3,5,5-trimethylhexanoyl chloride. By optimizing the operating conditions, they were able to achieve high conversion as well as reduced the operating time from 25 hours to 2.9 hours. Hafeez et al. (2022) studied different microchannel configurations for the production of hydrogen from formic acid in the presence of Pd/C catalyst. They compared packed bed microreactor with membrane microreactor and found that membrane microreactor significantly improved the conversion of formic acid.

1.4.2. Liquid-Liquid Extraction

Liquid-liquid extraction (LLE) is one of the most common methods to remove industrial pollutants (Shayesteh et al., 2021). Conventional LLE processes are time taking and require huge amounts of solvent. The use of microchannels for LLE will overcome these limitations due to short diffusion scales and low solvent consumption (Morshedaski et al., 2023). Singh et al. (2015) compared LLE in microchannel with conventional extractor. They observed better extraction rates in microchannels over conventional extractors demonstrating the potential of microchannels. Raji et al. (2023)

reviewed the effect of various geometric parameters on extraction efficiency in microchannels. Morshedaski et al. (2023) studied the extraction of crystal violet from hexane in T and Y-shaped microchannels. They found that Y-shaped microchannel showed better extraction performance over T-shaped one.

1.4.3. Nanoparticle Synthesis

Nanoparticles have gained significant attention in the past few decades due to their shape and size dependent properties (Ran et al., 2023). However, preparing nanoparticles of desired size distribution is challenging using conventional methods. The properties of nanoparticles are dependent on the size and structure. Microchannels can help in improving the synthesis of nanoparticles due to their fast heat and mass transfer rates. A list of some of the nanoparticles synthesized using microchannel devices is shown in Table 1.2.

Table 1.2 Synthesis of nanoparticles in Microchannels

Microchannel Type	Material	Size (nm)	Reference
T-shaped Microchannel	BaSO ₄	10-40	Li et al. (2008)
Spiral Microchannel	Ag	>10	Ravi Kumar et al. (2012)
Y-shaped Microchannel	Ag	≤ 5	Patil et al. (2012)
Y-shaped Microchannel	ZnO	3.6-5.2	Schejn et al. (2014)
T-shaped Microchannel	Au	2	Rahman and Rebrov (2014)
T-shaped Microchannel	Cu	4.25	Xu et al. (2015)
T-shaped Microchannel	Zn/Fe ₃ O ₄	≤ 5	Simmons et al. (2015)
Y-shaped Microchannel	Pt	<5	Suryawanshi et al. (2016)
Corning Advanced-Flow Reactor	Ag	4 - 10	Yang et al. (2021)

Serpentine Microchannel	Ru	-	Srivastava (2023)
Helical Millichannel	Ag	40	Kaabipour and Hemmati (2023)
Helical Microchannel	Ru	2 - 3	El-Kadi et al. (2024)

1.5. Importance of CFD

Since the dimensions of microchannels are very small, it is difficult to experimentally characterize the flow, mixing and reaction performance in the microchannel. Computational fluid dynamics (CFD) is a powerful tool that helps in overcoming these difficulties. The design of the microchannel can be optimized easily using CFD. The flow patterns and mixing can be studied at any desired location in the microchannel. In addition, multiphase applications can be analyzed and the effect of various parameters on them can be effectively predicted. Thus, CFD is used in this thesis to investigate single and multiphase flow characteristics in T-shaped microchannels.

2. LITERATURE REVIEW

2.1. Hydrodynamics and Mixing in Microchannels

The fast mixing times in micro T-mixers are first investigated by Bökenkamp et al. (1998). Roberge et al. (2005) stated that 50% of reactions in the fine chemical and pharmaceutical industry can benefit from the microreactor technology. Hessel et al. (2004) experimentally investigated a novel interdigital type micromixer with alternating feed channel to create multilamella. Gouillet et al. (2006) & Mansur et al. (2008) have reported that T-shaped microchannel has better mixing compared to Y and crossflow T-shaped microchannel. This is because in a T-shaped microchannel both the inlets contact in a counter-current pattern and the fluid has to pass around a sharp 90° bend. Mixing in microchannels can be induced using two techniques, passive and active (Lee et al. 2011b, 2016). In passive techniques, mixing is enhanced by making some geometric modifications to create disturbance in the streamline flow. With the active techniques, mixing is enhanced by giving the external source of energy to the system. Various passive and active mixing techniques proposed in literature are shown in Figure 2.1 & Figure 2.3. The schematics of various passive mixing techniques are depicted in Figure 2.2.

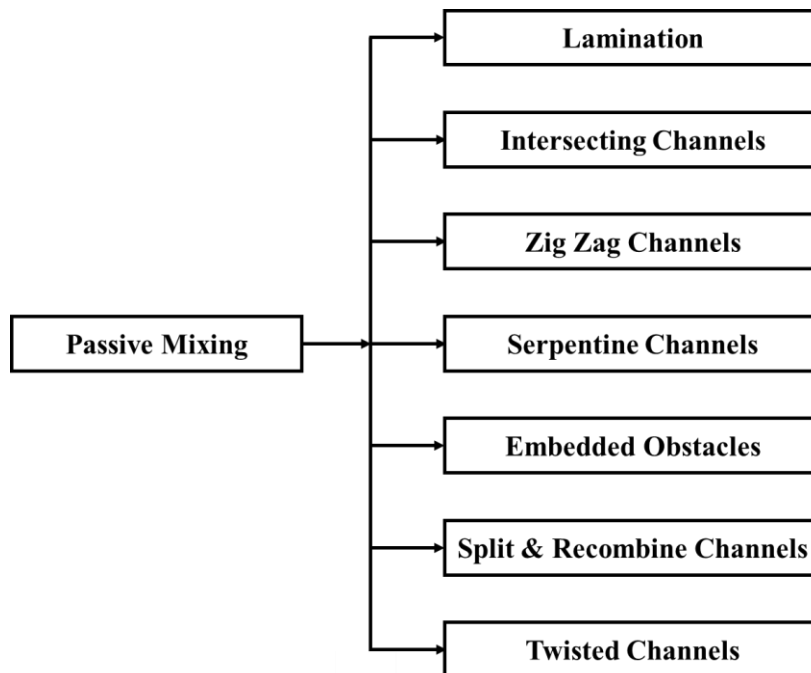


Figure 2.1. Passive mixing techniques in microchannels (Lee et al. 2011b)

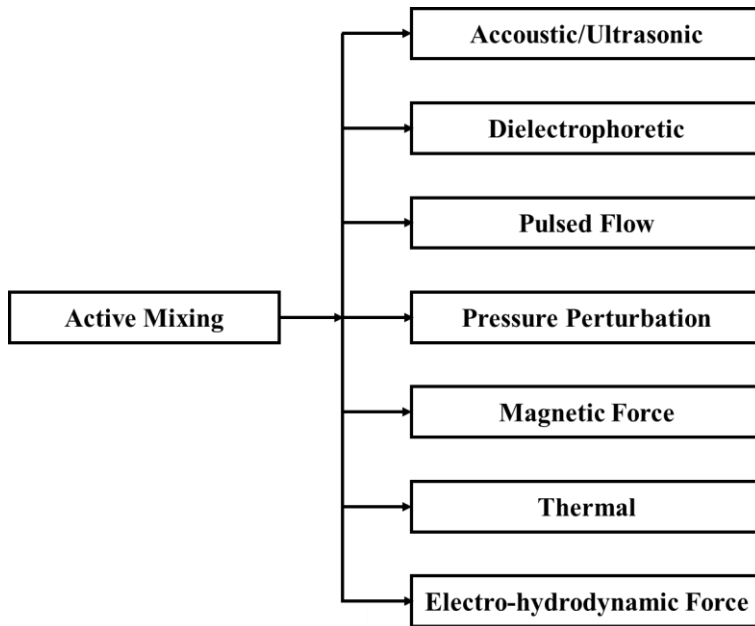


Figure 2.3. Active mixing techniques in microchannels (Lee et al. 2011b)

However, these active mixing techniques are not cost effective and sometimes not possible to implement due to some operating limitations. These techniques will have moving parts, which will make it extremely difficult to fabricate at micro level. Pulsating flow techniques are not possible when the dimensions are very small because of strong backflow. Compared to active mixing techniques passive techniques are simple and involve only one-time modification and does not contain any moving parts.

Liu et al. (2004) numerically studied the mixing performance of serpentine and herringbone mixers. They found that the mixing was mostly due to diffusion at Reynolds number of 1. As they increased the Reynolds number to 10, the mixing performance of serpentine mixer was improved and deteriorated for herringbone mixer. Lin et al. (2007) reported enhancement of single phase mixing using j-shaped baffles inside the micromixer. Sahu et al. (2012, 2013) investigated the effect of lateral obstacles on mixing performance and found out that staggered arrangement of obstacles improved mixing in microchannel. Afzal and Kim (2012) reported that split and recombination micromixers with convergent and divergent walls enhanced mixing significantly though the pressure drop was found to be higher. Alam et al. (2014) & Alam and Kim (2012) investigated mixing in a curved microchannel with rectangular and circular obstacles and reported that circular obstacles showed better mixing.

Duryodhan et al. (2017) reported that spiral microchannels enhanced mixing significantly.

2.2. Single-Phase Flow Regimes in Microchannels

T-shaped microchannels exhibit various flow regimes when operated at different Reynolds numbers called stratified, vortex and engulfment flows (Bothe et al., 2006; Soleymani et al., 2008). The stratified flow is observed at low Re, where the streamlines remain segregated. The mixing in stratified flow regime occurs due to diffusion. Galletti et al. (2012) observed symmetric vortex flow regime when Re increases. The vortex flow regime consists of four counter-rotating vortices and they are formed as a result of the instabilities caused by the centrifugal forces. They found that interaction among these vortices is weak. Further increase in Re beyond the symmetric vortex flow, asymmetric engulfment flow regime is observed. The asymmetric engulfment flow regime is characterized by a pair of asymmetric vortices (Fani et al., 2013). Mariotti et al. (2018) observed that the interaction among these asymmetric vortices is strong and improves the mixing in the microchannel. Zhang et al. (2019b) found that the mixing in engulfment flow regime is improved by the periodic oscillation of vortices. As the Reynolds number is increased further, Shestakov (2019) observed unsteady engulfment flow regime. The experimental tracer concentration at different flow regimes reported by Mariotti et al. (2018) is depicted in Figure 2.4.

Soleymani et al. (2008) defined the critical Reynolds number ($Re_{critical}$) at which vortex flow changes to engulfment flow. Soleymani et al. (2008, 2009) computationally investigated various flow regimes in a T-junction microchannel and proposed a correlation to predict $Re_{critical}$ for various aspect ratios. However, Reddy Cherlo and Pushpavanam (2010) found that the proposed correlation by Soleymani et al. (2008) is not valid for microchannels when width to depth ratio is less than one.

The effect of fluid properties and inlet flow conditions on engulfment flow regime was extensively studied by researchers. Galletti et al. (2012) computationally predicted the effect of microchannel inlet length on engulfment flow. They found a delay in achieving engulfment flow when the flow through the microchannel inlet is underdeveloped. Lobasov et al. (2016) numerically investigated the effect of viscosity on flow regimes. They found that the increase in viscosity has delayed the onset of

engulfment. They also observed that the mixing efficiency improved when the viscosity of one of the fluid stream increases. Lobasov and Shebeleva (2017) and Siconolfi et al. (2018) reported the effect of non-isothermal flow conditions on flow regimes and found that higher temperature gradient promotes engulfment flow regime.

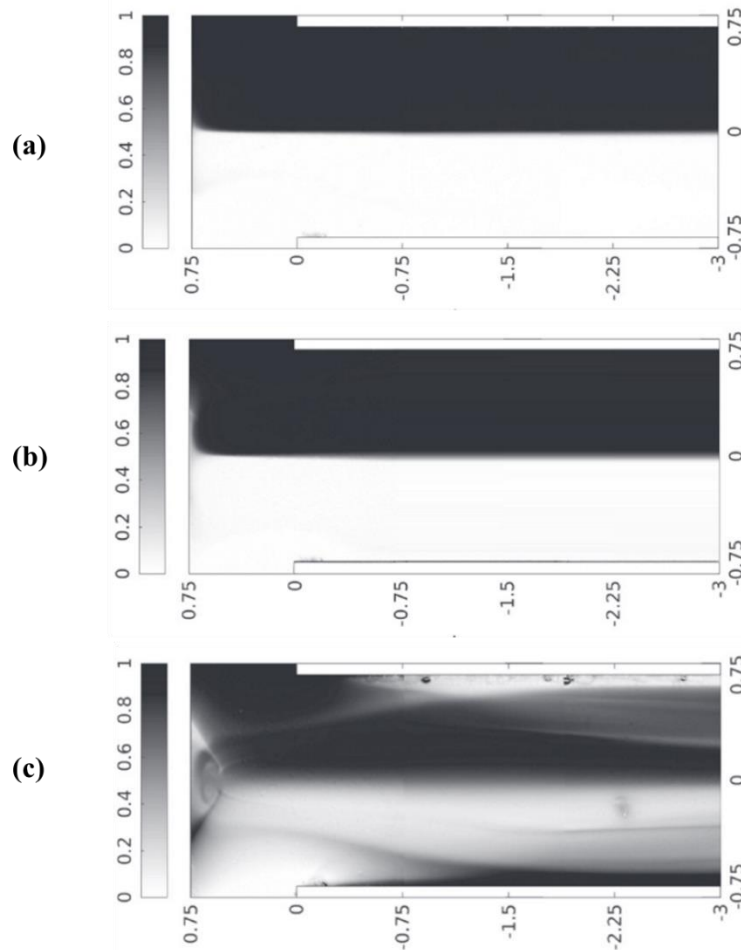


Figure 2.4. Tracer concentration at the centre plane of microchannel for (a) Stratified flow ($Re = 50$), (b) Vortex flow ($Re = 120$) and (c) Engulfment flow ($Re = 160$)

Galletti et al. (2017) analyzed the engulfment flow regime for binary liquid mixtures. They achieved engulfment flow regime at low Re for mixtures having positive fluidity (viscosity of the liquid mixture is higher than its components). Lobasov and Minakov (2017, 2018) predicted the effect of density and viscosity on the engulfment flow regime in a T-junction microchannel. They observed that the density change does not have a significant effect on engulfment flow regime and early onset of engulfment occurs when the viscosity ratio of liquids is increased. Kravtsova et al. (2018) analyzed the effect of inlet flow perturbations on flow regimes. They found that

the extent of mixing improved by 33% in engulfment flow regime for the perturbation frequencies of 500 Hz and 825 Hz. Lobasov et al. (2018) investigated engulfment flow for different non-Newtonian fluids in a T-junction microchannel. They observed that flow transition occurs at higher Re as the power-law exponent increases from 0.3 to 1. Dundi et al. (2019) achieved engulfment flow at low Re by introducing swirling effect at the inlets.

2.3. Micromixing in Microchannels

The mass transfer and reaction performance of a microchannel depends on the extent of micromixing in the system. The micromixing performance can be investigated through consecutive competitive reactions (Fournier et al. 1996). Chu et al. (2007) and Zhang et al. (2010) used Villiermaux - Dushman reaction to characterize micromixing in batch reactors. Bourne (2003) reviewed various parallel and series reaction schemes to quantify the extent of micromixing in batch reactors.

Krupa et al. (2014) analyzed micromixing in a microchannel by considering the reaction between 1-naphthol and di-azotized sulphanilic acid. They found that the selectivity was constant at higher Reynolds numbers. Cheng et al. (2019) investigated micromixing in microreactor using Villiermaux – Dushman reaction. Mariotti et al. (2021) recently investigated the micromixing in a microchannel using a parallel reaction between methylene blue and ascorbic acid catalyzed by HCl. The performance of the reaction was found to be limited by the residence time of fluid elements.

2.4. Crystallization in Microchannels

Crystallization is one of the major downstream operations in pharmaceutical and speciality chemical industries. Crystallization can be achieved by various techniques such as cooling crystallization, evaporative crystallization, anti-solvent crystallization and reactive crystallization (Mersmann, 2001). Among these, cooling crystallization and anti-solvent crystallization offer better control on the process compared to other two. In pharmaceutical industries, the quality and size of the crystals is critical. Thus, anti-solvent crystallization is majorly used. The quality of crystals depends on various factors such as mixing, mode of operation, antisolvent concentration, super-saturation, aggregation and breakage (Ashraf Ali and Falleiro,

2022; de Souza et al., 2021). In antisolvent crystallization, a saturated solution of solute is taken. As soon as antisolvent is added to the solution, the solubility of the solute in the solvent mixture decreases leading to supersaturation. This results in the crystallization of solute. An example of NaCl crystallization in water-ethanol system is shown in Figure 2.5. The amount of antisolvent added to the solution controls the nucleation and growth of the crystals (Wu et al., 2020). Adding higher concentrations of antisolvent will lead to high crystal nucleation and low crystal growth. Thus, an optimum amount of antisolvent should be added to obtain desired crystal size.

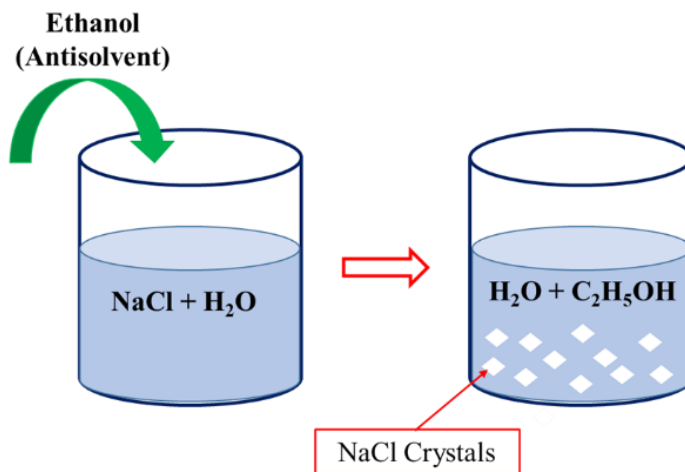


Figure 2.5. Antisolvent Crystallization of NaCl in Water-Ethanol mixture

Microchannels due to their small dimensions, high surface to volume ratio and fast mixing times offer better controllability of crystallization process. With the help of micro-crystallizers, high quality crystals with narrow crystal size distribution (CSD) can be obtained continuously. The quality of crystals in antisolvent crystallization depends on hydrodynamics, micromixing, antisolvent concentration and supersaturation (Mersmann, 2001). Microcrystallizers gained popularity in the recent years due to their ability to produce high quality crystals in micro and nano scale. Microcrystallizers also offer better control on morphology and size of the crystals. Various crystallization methods used in microchannels in the recent years are shown in Table 2.1.

Table 2.1 Crystallization in microchannels

Authors	Crystallization Method	Remarks
Wu et al. (2007)	Reactive crystallization (barium sulphate)	Nanocrystals of high quality were obtained in microchannels.
Du et al. (2013)	Reactive crystallization (barium sulphate)	BaSO ₄ nanocrystals of 40 nm size were obtained by introducing microbubbles into the microchannel
Valeh-e-Sheyda et al. (2015)	Anti-solvent crystallization (curcumin)	Larger confluence angle of microchannel inlets supported mixing and produced smaller crystals.
Bhamidi et al. (2015)	Anti-solvent crystallization (glycine)	The morphology of the glycine crystals was controlled effectively using microcrystallizers.
Melzig et al. (2019)	Anti-solvent crystallization (fenofibrate)	Faster mixing times produced smaller crystals with narrow CSD and vice versa.
Fatemi et al. (2019)	Cooling crystallization (paracetamol)	The addition of surfactant inhibited the nucleation of crystals in a gas-liquid crystallization system.
Nishigaki et al. (2020)	Anti-solvent crystallization (paracetamol)	The morphology of the paracetamol crystals was controlled effectively by varying the flow rates.
Doki and Masaaki (2021)	Anti-solvent crystallization (pyrene)	The crystal size decreased with increase in flow rate and solution concentration.
Yan et al. (2023)	Anti-solvent crystallization (triphenylmethanol)	Studied crystallization in a droplet based microcrystallizer. Improved crystal size distribution by using surfactant and higher antisolvent concentration.
Robertson et al. (2022)	Cooling crystallization (paracetamol)	Used a smooth temperature gradient method to cool the solution and controlled the nucleation of paracetamol crystals in the microcrystallizer. Using this method, they were able to grow large single crystals instead of multiple small crystals.
Jang et al. (2024)	Anti-solvent crystallization (sodium chlorate)	The size and chirality of the crystals formed were effectively controlled using the microchannels.

3. SCOPE AND OBJECTIVES OF THE WORK

3.1. Scope

In the published literature, several passive mixing techniques (obstacles, lamination, intersecting channels, zig-zag channels, serpentine channels, twisted channels, herringbone channels) were used to improve the flow patterns, macro and micromixing in microchannels. However, the investigations into the effect of inlet modifications of the microchannel are relatively limited in the literature. Inlet modifications can significantly improve mixing in the microchannel without the need for complex geometric structures along the mixing length. Hence, in the present work, geometric modifications at the inlet were proposed and their effect on flow patterns, flow regimes, macromixing, micromixing and antisolvent crystallization phenomena was addressed.

3.2. Objectives

The objectives of the research work are

1. To characterize the flow field, mixing and reactions in the T-shaped microchannel.
2. To study single-phase flow regimes prevailing in the T-shaped microchannel and achieve engulfment flow at low Reynolds number.
3. To characterize the micromixing performance of microchannel using a consecutive - competitive reaction.
4. To predict crystal growth and crystal size distribution for antisolvent crystallization of NaCl in the microchannel.

3.3. Organization of Thesis

Chapter 1: A brief introduction to microchannels and their applications.

Chapter 2: Overview of the literature on hydrodynamics, mixing, single-phase flow regimes, micromixing and crystallization in microchannels.

Chapter 3: Scope & Objectives of the research work.

Chapter 4: The experimental and numerical methodology along with appropriate numerical schemes employed.

Chapter 5: Results and discussion (hydrodynamics, mixing, single-phase flow regimes, micromixing and crystallization).

Chapter 6: Summary and conclusions.

4. RESEARCH METHODOLOGY

4.1. Geometry

The schematic of T-shaped microchannel considered and the microchannel fabricated in PMMA are depicted in Figure 4.1 (a) & (b) respectively. The cross-section of both the inlets and the channel was $200\ \mu\text{m}$ wide and $200\ \mu\text{m}$ deep. The length of both the inlets was $3\ \text{mm}$ and the mixing channel was $50\ \text{mm}$. Both the inlets were perpendicular to the mixing channel.

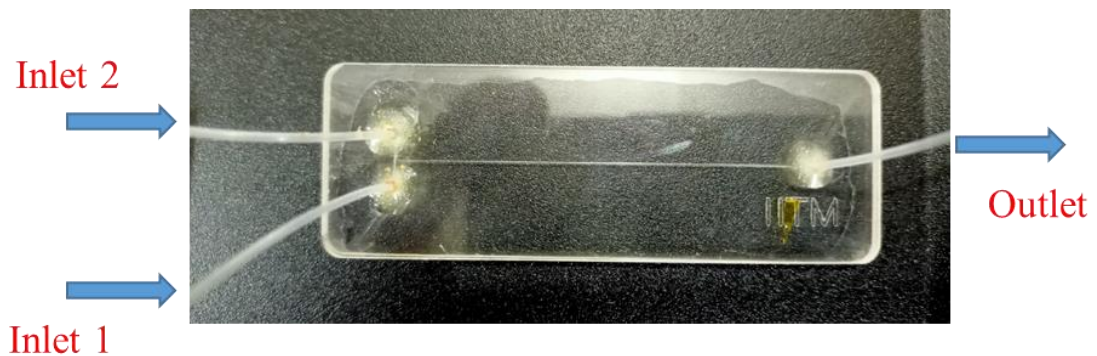
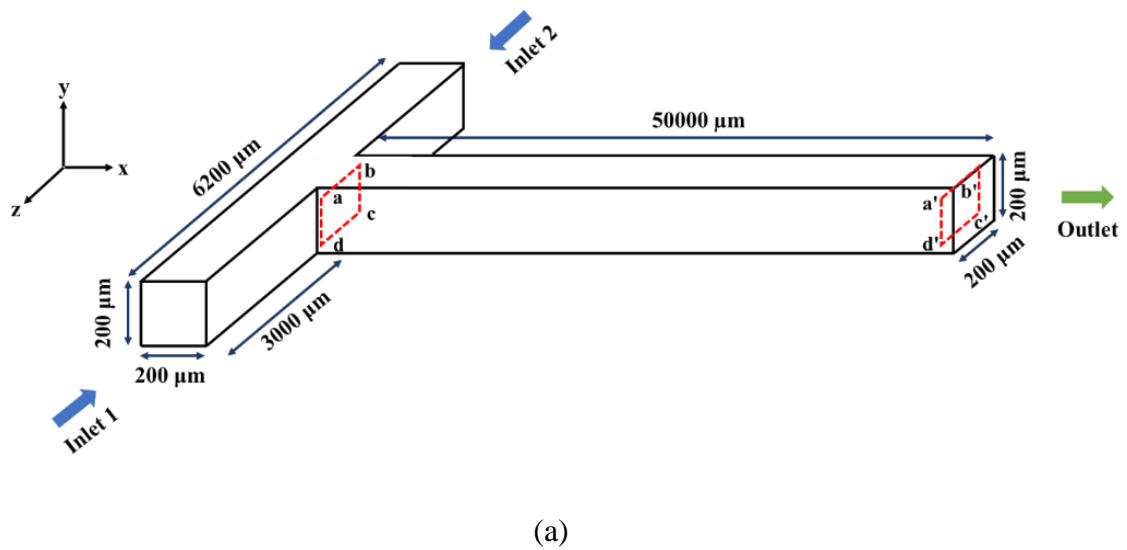


Figure 4.1. (a) Schematic of T-shaped Microchannel and (b) Microchannel fabricated in PMMA.

4.2. Experimental Methodology

4.2.1. Experimental Setup

The experimental setup used for flow visualization in microchannel is shown in Figure 4.2. The microchannel was fabricated using polymethyl methacrylate (PMMA). The liquid was injected through the inlets using syringe infusion pumps (R100, Ravel Hitek India). The microchannel inlets and syringes were connected using Teflon tubes. An upright microscope (Labomed, USA) mounted with a high-speed microscope camera (672 x 512 pixels, Basler, Germany) was used to capture the images of the microchannel. The field of view was 0.79 mm x 0.2 mm near the outlet. These images were processed using image processing toolbox (MATLAB 2019b).

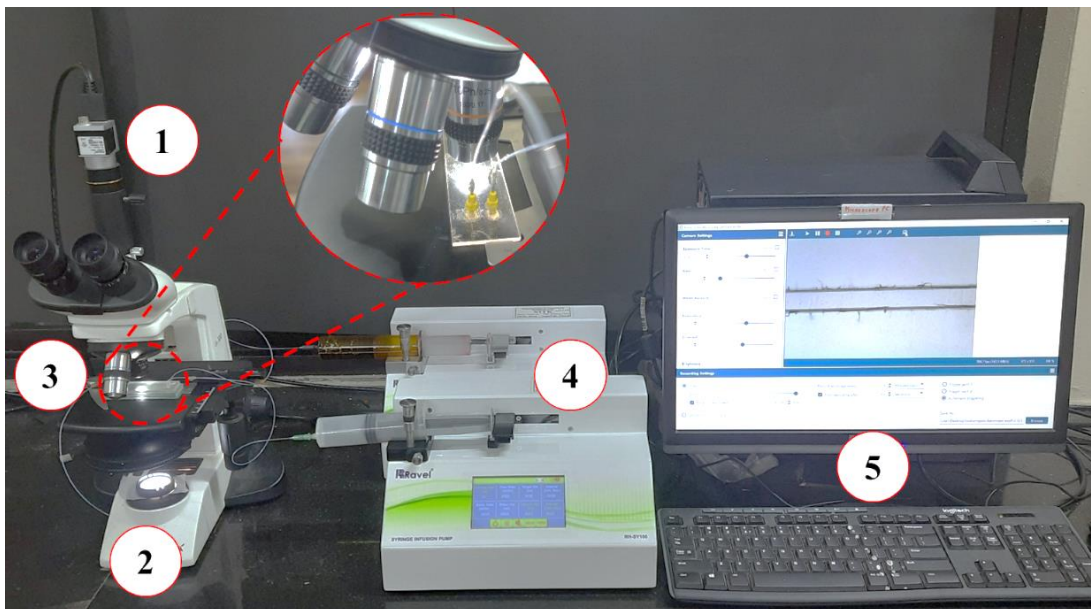


Figure 4.2 Experimental setup. (1) high speed microscope camera, (2) microscope, (3) microchannel, (4) syringe infusion pumps and (5) computer

4.2.3. Experimental Procedure

4.2.3.1. Flow Field

To visualize the flow field in our system, distilled water was used. Here, water was seeded with tiny, neutrally buoyant polystyrene particles (average size = 1 μm , $\rho = 1055 \text{ kg/m}^3$, Sigma Aldrich). Two hundred images were taken at 500 frames per second (fps) for the inlet velocity of 2.5 mm/s. These images were processed using

PIVlab (Thielicke and Stamhuis, 2014) in MATLAB to obtain velocity field through Ghost Particle Velocimetry (GPV) technique (Buzzaccaro et al., 2013).

4.2.3.2. RTD & Mixing

The mixing in the system was analyzed through RTD studies with Rhodamine B (Sigma Aldrich) as a tracer. At first, water was injected through both the inlets. A pulse of tracer (3.04 mM Rhodamine B) was introduced at one of the inlets after flow field attained steady state in a time-averaged sense. To measure the concentration of the tracer, images (at $x = 40$ mm) were taken using high-speed microscope camera at a rate of 200 fps until tracer was completely recovered from the microchannel. These images were processed using MATLAB to quantify the concentration of tracer.

4.2.3.3. Single Phase Flow Regimes

To validate flow regimes, tracer was injected from one inlet of the microchannel and distilled water from the other. Then the images of flow regimes at the T-junction were captured for different Reynolds number. These images were then compared with simulation predictions.

4.3. Computational Methodology

4.3.1. Transport equations

4.3.1.1. Hydrodynamics

The flow field in a microchannel is predominantly governed by surface and viscous forces. Since gravitational and buoyancy effects are minimal in our system, the flow is essentially laminar. Here, fluid was considered as incompressible. Meng et al. (2014) have found that surface tension has a negligible effect on the flow field in microchannels with a hydraulic diameter greater than 0.1 mm. Thus, surface tension effects was not taken into consideration for single phase flows. Thus, the flow field in the microchannel is described by continuity and Navier – Stokes equation. (Ferziger & Peric, 2002). The continuity and momentum equations are given as,

$$\nabla \cdot \mathbf{u} = 0 \quad (4.1)$$

$$\rho \left(\frac{\partial \mathbf{u}}{\partial t} + \mathbf{u} \cdot \nabla \mathbf{u} \right) = -\nabla p + \mu \nabla^2 \mathbf{u} \quad (4.2)$$

To predict mixing performance in a microchannel, species transport equation

was used (Bird et al., 2006)

$$\frac{\partial c}{\partial t} = D\nabla^2 c - \mathbf{u}\nabla c \quad (4.3)$$

The diffusion coefficient ($D = 4.0 \times 10^{-10} \text{ m}^2/\text{s}$) of Rhodamine B tracer in water was obtained from Gendron et al., (2008). The intensity of mixing in the microchannel was quantified using the mixing index (MI) given by

$$\text{MI} = 1 - \frac{1}{2\bar{X}} \sqrt{\frac{1}{N} \sum_{i=1}^N (X_i - \bar{X})^2} \quad (4.4)$$

where, \bar{X} was mean concentration (or) intensity for fully segregated condition, X_i was concentration (or) intensity in i^{th} element (or) pixel and N was number of elements or pixels. Mixing index is a measure of the degree to which tracer is dispersed in the fluid. Here, MI value of 0.5 indicates complete segregation and 1 indicates uniform mixing.

To study the implications of microchannel on reactions, a fast neutralization reaction between sodium hydroxide (NaOH) and hydrochloric acid (HCl) was considered. This reaction is chosen in such a way that the reaction time is less than mixing time. Hence, the conversion of reactants is dependent on the mixing of species and independent of reaction kinetics. Here, the microreactor performance was influenced by flow behaviour and micro-mixing. The reaction scheme is shown in equation 4.5.



The rate of reaction of species is governed by equation 4.6. The rate constant for this reaction was taken as, $k = 1.4 \times 10^8 \text{ m}^3/\text{mol}\cdot\text{s}$ (Fournier et al., 1996).

$$\frac{\partial(\rho x_i)}{\partial t} + \nabla \cdot (\rho \mathbf{u} x_i) = -\nabla \cdot \vec{J}_i + r_i + s_i \quad (4.6)$$

4.3.1.2. Single Phase Flow Regimes

To identify single phase flow regimes, the flow field was predicted at various Reynolds numbers using equations 4.1 and 4.2. To analyse mixing of tracer in these flow regimes, species transport equation was used (equation 4.3). To qualitatively characterize the mixing in various flow regimes, Poincaré maps (Krishnaveni et al.,

2017) were used. To generate Poincaré maps, buoyant tracer particles were introduced into the system through Lagrangian manner. The trajectories of these particles were computed through the discrete phase model (DPM). The discrete phase model follows Euler-Lagrangian approach where fluid is treated as continuous phase and buoyant tracer particles as discrete phase. To predict the particle trajectories, the force balance on each and every particle was formulated using Newton's second law of motion (Ashraf Ali and Pushpavanam, 2011). The force balance on each discrete particle is written as

$$\frac{d\mathbf{u}_p}{dt} = F_D(\mathbf{u} - \mathbf{u}_p) + F_x \quad (4.7)$$

Once velocity is predicted using Eqn 4.7, the trajectories of discrete particles are computed. The drag force acting on the buoyant tracer particles is given by

$$F_D = \frac{18\mu C_D Re}{\rho_p d_p^2} \frac{C_D Re}{24} \quad (4.8)$$

The calculation of drag force involves relative Reynolds number and it is given by

$$Re = \frac{\rho d_p |\mathbf{u}_p - \mathbf{u}|}{\mu} \quad (4.9)$$

In addition to the drag force, lift force (Saffman, 1965) and the pressure gradient force were considered in the present investigation. The details of these additional forces were obtained from the literature (Ashraf Ali and Pushpavanam, 2011b; ANSYS, 2019).

These generated Poincaré maps were quantified using Shannon's entropy (Camesasca et al., 2006; Krishnaveni et al., 2017). The region of interest in the microchannel was subdivided into several equally sized sections called bins. The Shannon's entropy (S) & probability distribution (p_k) of particles in each bin was calculated by

$$S = - \sum_{k=1}^M p_k \ln p_k \quad (4.10)$$

$$p_k = \frac{\frac{x_k}{P}}{\sum_{i=1}^M \frac{x_i}{P}} \quad (4.11)$$

The higher value of Shannon's entropy indicate better distribution of particles and hence uniform mixing.

4.3.1.3. Micromixing

To characterize micromixing in the microchannel consecutive competitive reactions between diazotized sulphanilic acid and 1-naphthol (Baldyga and Pohorecki, 1995; Krupa et al., 2014) were considered. The concentration of reactants and products was predicted by solving the species balance equation (equation 4.5) along with the basic transport equation. The micromixing performance was further analyzed by quantifying the interactions between the fluid elements. Here buoyant particles were introduced from both the inlets through Lagrangian manner. Discrete phase model (DPM) was used to obtain the trajectories of fluid particles (equation 4.6). The collisions among the fluid elements are predicted through a stochastic collision model. The probability of collision between two particles was computed using algorithm proposed by O'Rourke (ANSYS, 2019; O'Rourke, 1981).

4.3.1.4. Antisolvent Crystallization

To predict the antisolvent crystallization of NaCl in water-ethanol system CFD was coupled with population balance model (PBM). Two phase Euler-Granular approach was used to predict the continuous phase flow field and crystal dynamics in the microchannel. The solution was treated as continuous phase and crystals as dispersed granular phase. The two phase flow in the microchannel is governed by (Ashraf Ali and Falleiro, 2022; ANSYS, 2019).

Continuity equation:

$$\frac{\partial}{\partial t}(\alpha_j \rho_j) + \nabla \cdot (\alpha_j \rho_j \mathbf{u}_j) = \sum_{k=1}^n \dot{m}_{jk} \quad (4.12)$$

Momentum equation:

$$\frac{\partial}{\partial t}(\alpha_j \rho_j \mathbf{u}_j) + \nabla \cdot (\alpha_j \rho_j \mathbf{u}_j \mathbf{u}_j) = -\Delta p_s \alpha_j + \sum (R_{jk} + \dot{m}_{jk} \mathbf{u}_j) + \alpha_j \rho_j F_{d,j} \quad (4.13)$$

where, α_j is the volume fraction of j^{th} phase, ρ_j is the density of j^{th} phase, \mathbf{u}_j is the velocity of j^{th} phase, p_s is solid pressure, \dot{m}_{jk} is the interphase mass exchange, R_{jk} is interphase force exchange and $F_{d,j}$ is the drag force on j^{th} phase. The sum of volume fractions of the phases is considered equal to one. The interphase force exchange was calculated using

$$R_{jk} = k_{ls}(\mathbf{u}_l - \mathbf{u}_s) \quad (4.14)$$

where, k_{ls} is the interphase momentum exchange coefficient, \mathbf{u}_l is the velocity of liquid and \mathbf{u}_s is the velocity of crystals. Here, the volume fraction of crystals is less than 0.2 (dilute system). Hence, Wen-Yu drag model is used (Wen and Yu, 1966). The interface momentum exchange coefficient given by Wen-Yu is

$$k_{ls} = \frac{3}{4} C_D \frac{\alpha_s \alpha_l \rho_l |\vec{u}_s - \vec{u}_l|}{d_s} \alpha_l^{-2.65} \quad (4.15)$$

$$C_D = \frac{24}{\alpha_l Re_s} [1 + 0.15(\alpha_l Re_s)^{0.687}] \quad (4.16)$$

$$Re_s = \frac{\rho_l d_s |\vec{u}_s - \vec{u}_l|}{\mu_l} \quad (4.17)$$

where, C_D is the drag coefficient, Re_s is the relative Reynolds number, α_s is the volume fraction of granular phase (crystals), α_l is the volume fraction of continuous phase, ρ_l is the density of continuous phase, d_s is the diameter of crystals and μ_l is the viscosity of continuous phase.

PBM was defined using the number density function as shown in equation 4.18 (ANSYS, 2019).

$$\frac{\partial}{\partial t} [n(V, t)] + \nabla \cdot [\mathbf{u}n(V, t)] + \nabla_V \cdot [G_V n(V, t)] = \frac{1}{2} \int_0^V a(V - V', V') n(V - V', t) n(V', t) dV' - \int_0^\infty a(V, V') n(V, t) n(V', t) dV' \quad (4.18)$$

The volume of single crystal (V) and volumetric growth rate (G_V) are defined as

$$V = k_v L^3 \quad (4.19)$$

$$G_V = 3k_v L^2 G \quad (4.20)$$

The initial conditions were given as

$$n(V, t = 0) = n_v; G_V n(V = 0, t) = B \quad (4.21)$$

where, $n(V, t)$ is the number density of crystals with volume V at time t , G_V is the growth rate based on volume of the crystal, B is the nucleation rate, n_v is the initial number density of crystals, k_v is the volumetric shape factor, L is the size of the crystal and G is the growth rate.

Since the crystals are in micron size, the breakage among the crystals was ignored. The crystallization kinetics of NaCl were obtained from Wu et al., (2020)

Nucleation Rate:

$$B = 1.328 \times 10^9 \times SS^{3.603} / (1 + m) \quad (4.22)$$

Growth Rate:

$$G = 1.885 \times 10^{-7} \times SS^{1.079} \quad (4.23)$$

Supersaturation:

$$SS = (C - C^*) \cdot (1 + m) \quad (4.24)$$

$$C^* = 356.4 e^{-1.156m} \quad (4.25)$$

where, SS is the relative super saturation, C^* is the solubility of NaCl in water-ethanol mixture, C is the concentration of NaCl and m is the mass fraction of ethanol in solvent mixture. Equations 4.22-4.25 are applicable when the solution is supersaturated (i.e. $S > 1$). The algorithms used to simulate all the above discussed phenomena are provided in Appendix - I.

4.3.2. Simulation Setup

The numerical simulations in T-shaped microchannel were performed using commercial CFD software (ANSYS Fluent 2022R2). The geometry of the microchannel was modelled through Ansys-Workbench (Version 2022R2). The computational domain was discretized using 12.5 μm , 13 μm and 14 μm grid sizes with 11, 9 and 7.5 lakh elements respectively to determine the independence of the results on the grid chosen. The Reynolds number of the system was in the range of 1 - 400. Hence, the laminar flow model was used. The momentum equations were discretized using the QUICK scheme. The SIMPLE algorithm was used to couple the pressure and

velocity field. The least-squares cell gradient approximation was used to evaluate the flow properties at the face value. CFD calculations were performed with optimized time step size (Δt) of 0.5 ms with 100 iterations per Δt . The convergence criteria for the residuals of transport properties was taken as 10^{-5} . The velocity inlet boundary condition (BC) was used at the inlet while pressure outlet at the exit. No-slip BC was specified at the walls of microchannel. Water ($\rho = 998.4 \text{ kg/m}^3$ and $\mu = 0.001003 \text{ Pa}\cdot\text{s}$) was used to investigate the flow field in the micro-channel.

The species transport model was used to perform reactions numerically through the volumetric reaction mechanism. The dilute solution of NaOH (0.1 M) was introduced through inlet 1 while dilute solution of HCl (0.1 M) at inlet 2 with a velocity of 0.05 mm/s to study the progress of the reaction.

To obtain trajectories of tracer particles in DPM simulations, reflect BC was specified on the channel walls and escape BC at the channel outlet. The tracer particles were injected from both the inlets continuously for a flow time of 2 sec. The time step to solve the trajectories of discrete phase particles was considered as 5×10^{-5} s. The particles were considered inert and spherical with a diameter of 1 μm . The particle density was 998.4 kg/m^3 . The one-way coupling was used in which continuous phase flow field was not affected by the discrete particle motion.

To characterize the extent of micromixing, liquid phase reactants A (1-naphthol) and B (diazotized sulphanilic acid) were introduced at the inlets of the microchannel. The consecutive – competitive reaction scheme considered is shown below (Krupa et al., 2014)



where, A was 1-naphthol, B was diazotized sulphanilic acid, R was mono-azo dye, S was bis-azo dye, k_1 was the rate constant for reaction-1 ($15.3 \times 10^3 \text{ m}^3 \text{mol}^{-1} \text{s}^{-1}$) and k_2 was the rate constant for reaction-2 ($3.04 \text{ m}^3 \text{mol}^{-1} \text{s}^{-1}$). R was the desired product, while S was the undesired product. The initial concentration of both the reactants (A and B) was maintained as 0.01M. The reactants were injected separately into the microchannel

from each of the inlets. The reactions 4.23 and 4.24 were considered as volumetric reactions. The reactions progress as the reactants pass through the microchannel. In the above mentioned reactions R is the desired product and S is the undesired product. The yield and selectivity of the desired product (R) were calculated using (Levenspiel, 1999)

$$\text{Yield, } Y = \frac{C_R}{C_{A0}} \quad (4.25)$$

$$\text{Selectivity, } Se = \frac{C_R}{C_S} \quad (4.26)$$

The extent of micromixing was further quantified by analyzing the interactions between the fluid elements through the Lagrangian approach using DPM. The particles were injected uniformly into the microchannel and the extent of mixing was estimated by quantifying the number of probable collisions per unit time in the microchannel at different flow regimes. Here four-way coupling was used in which the effect of continuous phase flow on discrete particles, the effect of discrete particle motion on continuous phase, discrete particle interactions and discrete particle interactions with wall were considered. The single-phase and DPM simulations were carried out on a HP Desktop Computer consisting of Quad core Intel i7 processor (8 core, 3.7 GHz) and 32 GB RAM (1600 MHz, DDR3). All the simulations were run for a physical time of 2 sec.

The Eulerian multiphase model coupled with PBM was used to predict antisolvent crystallization. In addition to the continuity, momentum and species transport equations, Discrete method of PBM was used to predict the nucleation, growth and aggregation of crystals in microchannel. In discrete method, a range of crystal size (1 to 5 μm) was considered and they were divided into 20 bins. The size of the smallest crystal was taken as 1 μm (Wu et al., 2020). The nucleation kinetics, growth rate and solubility of NaCl crystals were specified using a user defined function (UDF) in Ansys Fluent. The antisolvent crystallization simulations were carried out on a Dell workstation consisting of dual Intel Xeon Gold processors (64 core, 2.4 GHz) and 160 GB RAM (3200 MHz, DDR5). An adaptable time step size based on Courant number was used with 20 iterations per time step. The simulations were run for a physical time of 2 sec.

5. RESULTS AND DISCUSSION

5.1. Grid & Time Independence Studies

To determine the grid independence of the numerical solution four different grid sizes (12 μm , 12.5 μm , 13 μm and 14 μm) are considered. 3D transient CFD simulations were performed for an inlet velocity of 0.1 m/s. The velocity profile near the outlet of the microchannel was compared for all grid sizes as shown in Figure 5.1.

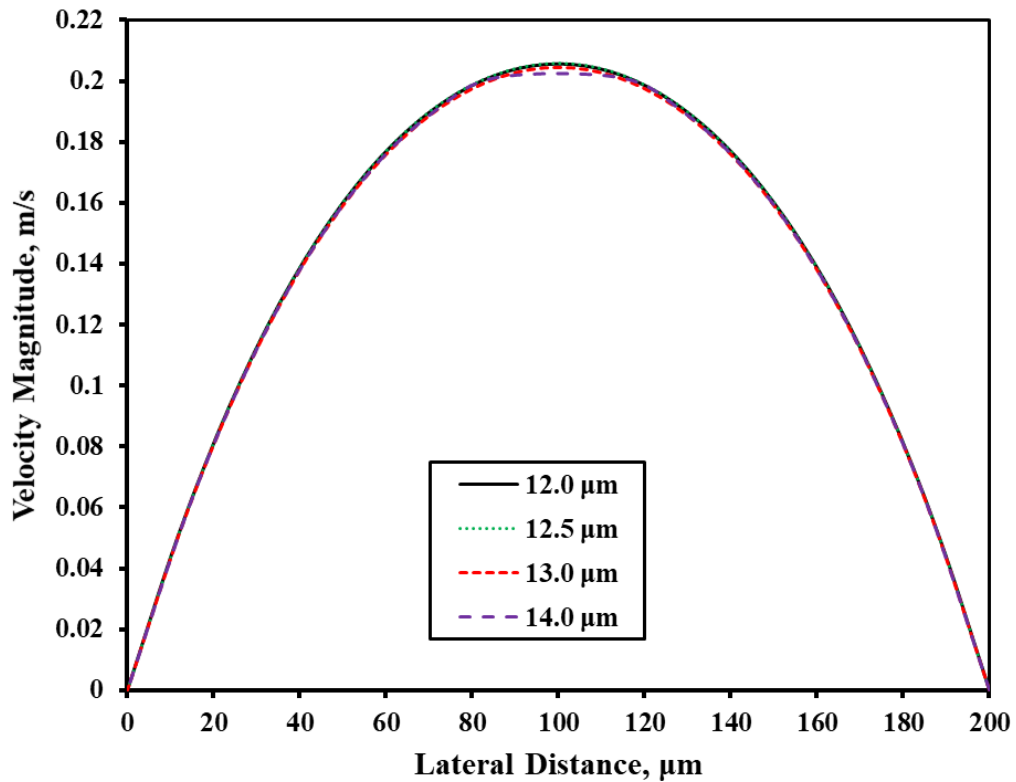


Figure 5.1. Velocity profile near the outlet for various grid sizes

It was observed that the velocity profile is similar for the grid sizes of 12 μm and 12.5 μm . The maximum velocity achieved at different grid sized is compared in Table 5.1. The deviation in velocity was found to be insignificant for 13 μm grid whereas it was significant for 14 μm grid. Thus, 13 μm grid was considered as optimum in terms of accuracy and computational time.

To determine the optimum time step size (Δt) for 3D transient simulations, four different Δt (0.2 ms, 0.5 ms, 1 ms and 5 ms) were considered. The temporal variation of velocity magnitude at a point ($x = 0 \mu\text{m}$, $y = 100 \mu\text{m}$, $z = 0 \mu\text{m}$) for different Δt is

shown in Figure 5.2. Large deviation was observed for the time step size of 5 ms and little deviation was observed for 1 ms and 0.5 ms compared to 0.2 ms. Thus 0.5 ms was considered as optimum time step size.

Table 5.1 Maximum velocity achieved for different grid sizes

Grid Size (μm)	No of Elements (in Million)	Maximum Velocity (m/s)	% Deviation
12.0	1.35	0.205	-
12.5	1.10	0.205	0.0 %
13.0	0.95	0.204	0.5 %
14.0	0.75	0.201	2.0 %

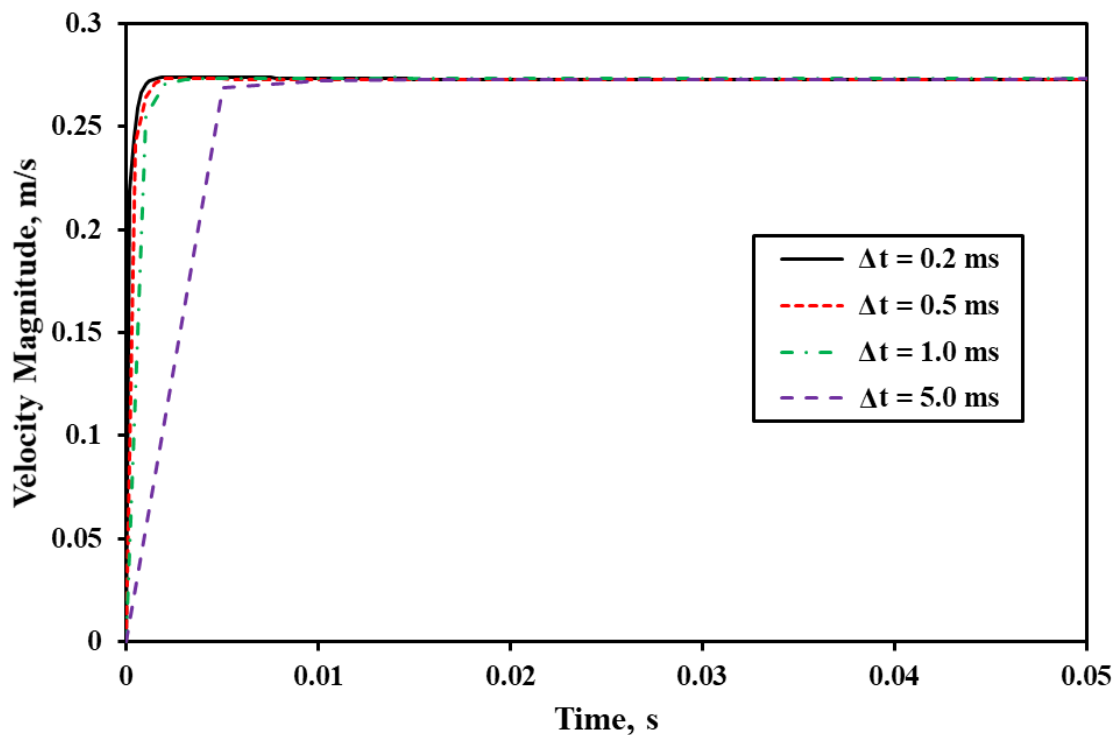


Figure 5.2 Temporal variation of velocity magnitude at a point ($x = 0 \mu\text{m}$, $y = 100 \mu\text{m}$, $z = 0 \mu\text{m}$) for different Δt

5.2. Hydrodynamics & Mixing

5.2.1. Hydrodynamics

The hydrodynamics in a T – shaped microchannel was analyzed numerically using transient 3D simulations. To investigate the flow field, a horizontal plane ($y = 0.1$ mm) has been chosen and the predicted contours of velocity magnitude were analyzed at various time instants for the inlet velocity of 0.05 m/s. This is shown in Figure 5.3 and the corresponding streamlines are depicted in Figure 5.4.

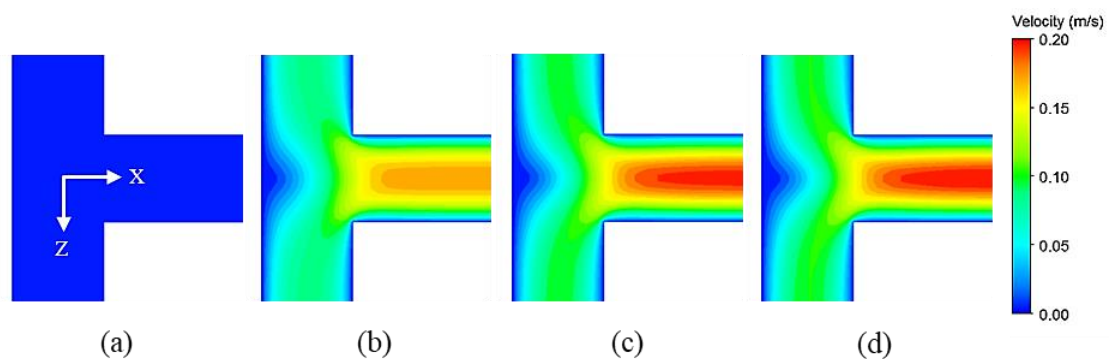


Figure 5.3 Contours of velocity magnitude for $Re = 20$. (a) $t = 0$ s, (b) $t = 0.001$ s, (c) $t = 0.15$ s and (d) $t = 1$ s

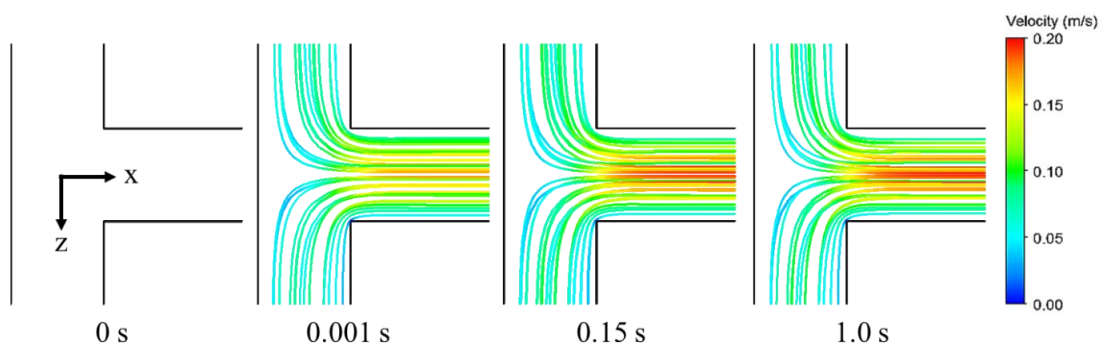


Figure 5.4 Streamlines of velocity magnitude $Re = 20$. (a) $t = 0$ s, (b) $t = 0.001$ s, (c) $t = 0.15$ s and (d) $t = 1$ s

The magnitude of velocity was zero at time $t = 0$ s. As the time progresses, the velocity magnitude span across the channel cross-section with the maximum velocity at the centre and minimum close to the wall. The steady flow field was observed in less than 1 s. To validate the numerical predictions, the velocity profile in the microchannel was experimentally determined through Ghost Particle Velocimetry technique. This

technique was explained in section 4.2.3.1. The spatial variation of velocity magnitude along a horizontal line ($x = 30 \text{ mm}$, $y = 0.1 \text{ mm}$) at $\text{Re} = 1$ was analysed. This is shown in Figure 5.5. It was observed that numerical predictions were comparable with experimental observations with a maximum error of $\pm 10\%$. Due to the roughness induced by the milling on the walls of microchannel, a non-symmetric parabolic profile was observed experimentally. To quantify the flow field, liquid circulation rate was calculated near the entrance and exit of the mixing channel. Liquid circulation rate is defined as the line integral of velocity around a closed curve (Fox et al. 2009). Liquid circulation rate quantifies the circulatory movement of fluid. This is given as

$$\Gamma = \oint \mathbf{u} \cdot d\mathbf{l} \quad (5.1)$$

Two closed regions (abcd and a'b'c'd') were considered to calculate liquid circulation rate as shown in Figure 4.1. The effect of Reynolds number on liquid circulation rate is reported in Figure 5.6. It was observed that the liquid circulation was zero near the exit indicating fully developed and unidirectional flow. The liquid circulation rate was found to increase with Reynolds number at the entrance of the channel.

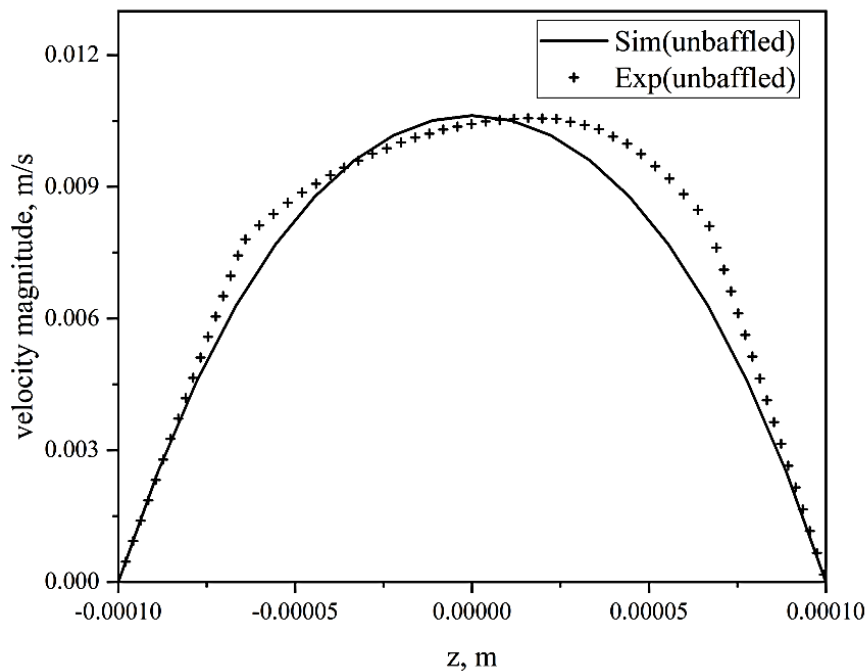


Figure 5.5 Spatial variation of velocity magnitude along a horizontal line ($x = 30 \text{ mm}$, $y = 0.1 \text{ mm}$ and $\text{Re} = 1$)

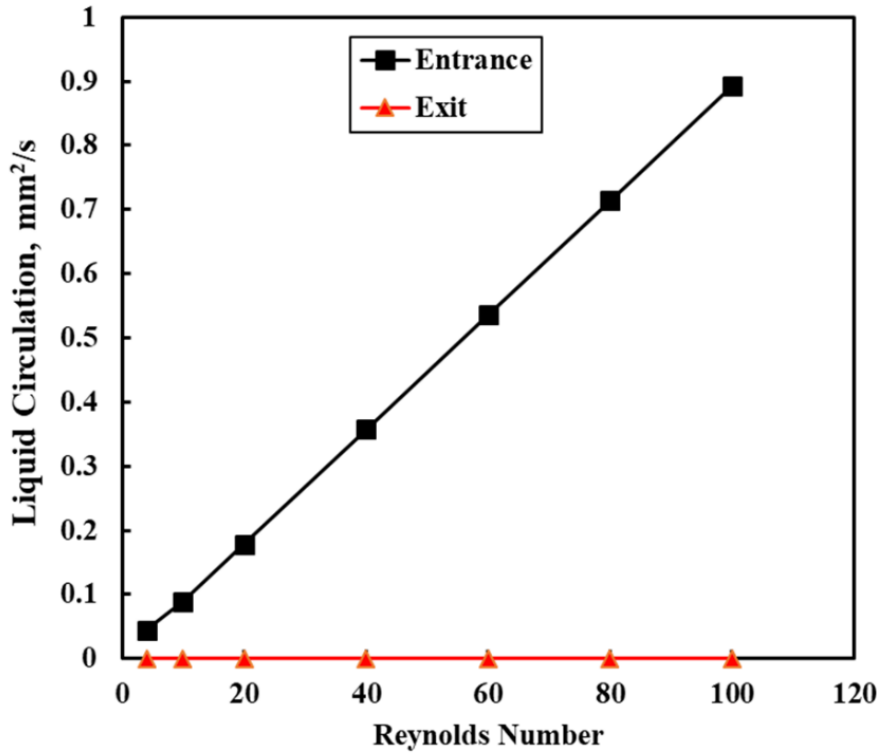


Figure 5.6 Effect of Reynolds number on liquid circulation rate

5.2.2. *Mixing*

To analyze mixing in our system, water was sent through one inlet of microchannel and tracer solution (0.38 mM Rhodamine B) through the other inlet. A small region near the outlet was chosen and two hundred images were captured using the high speed microscope camera for every Reynolds number. The intensity of each pixel in the images was measured to calculate the mixing index. The effect of Re on mixing index is shown in Figure 5.7. It was observed that there was a considerable difference between numerical predictions and experimentally measured values. This was because the camera was able to capture only the top surface of the microchannel and unable to provide complete information of lateral concentration in vertical direction. The mixing was found to be maximum at Re of 5. At this Reynolds number, the residence time of the fluid was high and mixing was diffusion dominant. As the Reynolds number was increased, the mixing index dropped to a minimum at 60. Beyond 60 and increasing trend in the mixing was observed. However, the intensity of mixing was very low over the range of Reynolds numbers (5 – 100) studied. We would require long channels and very low flow rates to achieve uniform mixing.

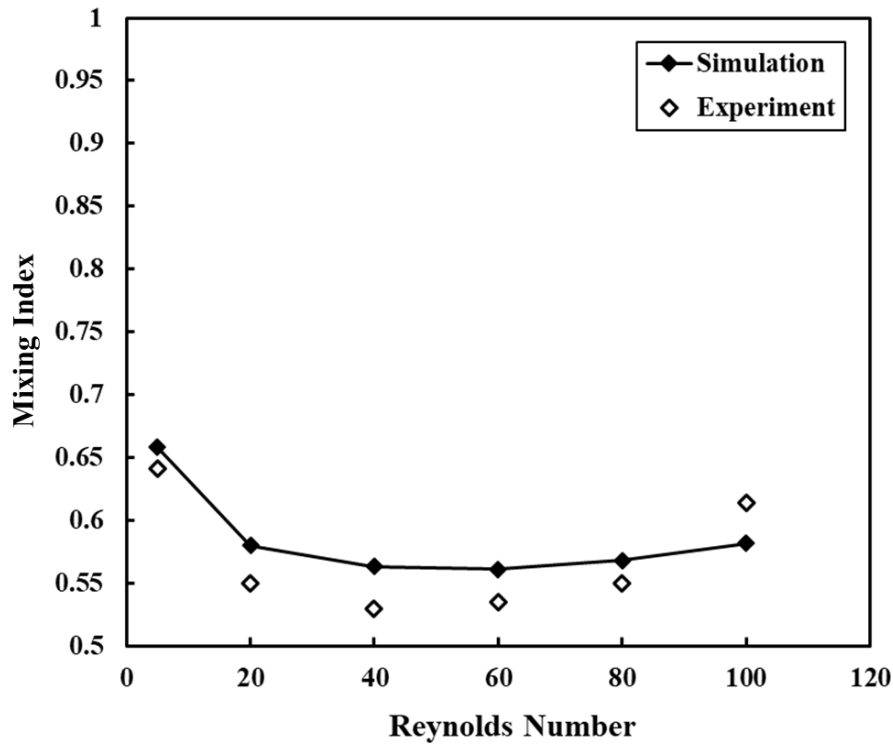


Figure 5.7 Effect of Re on mixing index

Thus, to improve the flow field and mixing in the microchannel, two types of baffle configurations were considered. Here, (i) rectangular baffles were placed along the sides of the microchannel consecutively (B1) and (ii) trapezoidal baffles were placed sideways in a staggered arrangement (B2) throughout the microchannel length at an equal distance of 2.5 mm. The schematics of the modified geometries are shown in Figure 5.8.

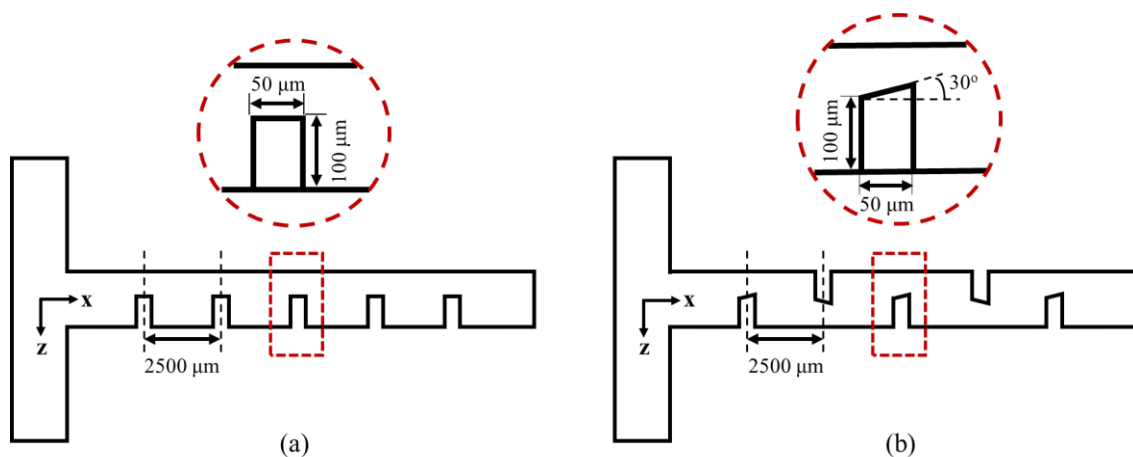


Figure 5.8 Schematic of proposed geometric modifications with (a) consecutive side baffles, B1 (b) alternate trapezoidal baffles, B2

The flow field in the microchannel with baffle configurations was investigated using 3D simulations. The contours of velocity for a Reynolds number of 20 is depicted in Figure 5.9. For baffle configuration B1, sudden contraction and expansion happens near the baffles and for B2 configuration gradual contraction and sudden expansion happens near the baffle. These baffles help in changing the flow direction as well as improve lateral mixing during the contraction and expansion of fluid. The effect of these baffle configurations on pressure drop and liquid circulation is shown in Figure 5.10 and 5.11, respectively.

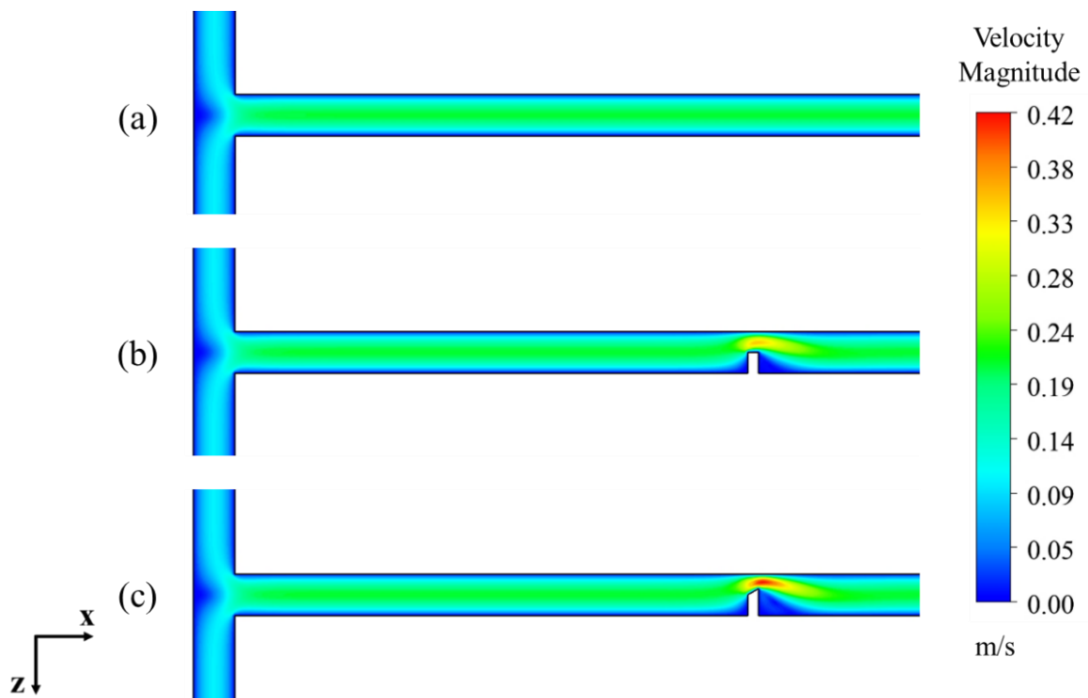


Figure 5.9 Contours of Velocity Magnitude for different baffle configurations

It was observed that the liquid circulation improved significantly when baffles were introduced. The pressure drop was also found to increase significantly with baffles. Maximum pressure drop was observed for B2 configuration. To compare the performance of the microchannel with modified geometries, residence time distribution (RTD) studies were carried out experimentally and computationally. Here, a pulse of tracer (3.04 mM Rhodamine B) was injected into one of the inlets of the un baffled microchannel. The concentration of tracer near the outlet ($x = 40$ mm) was monitored by capturing images at a rate of 200 fps until all the tracer was recovered. This was modelled numerically through CFD for all three configurations. The CFD predictions were validated for the un baffled system. The measured residence time distribution for

pulse inputs is shown in Figure 5.12.

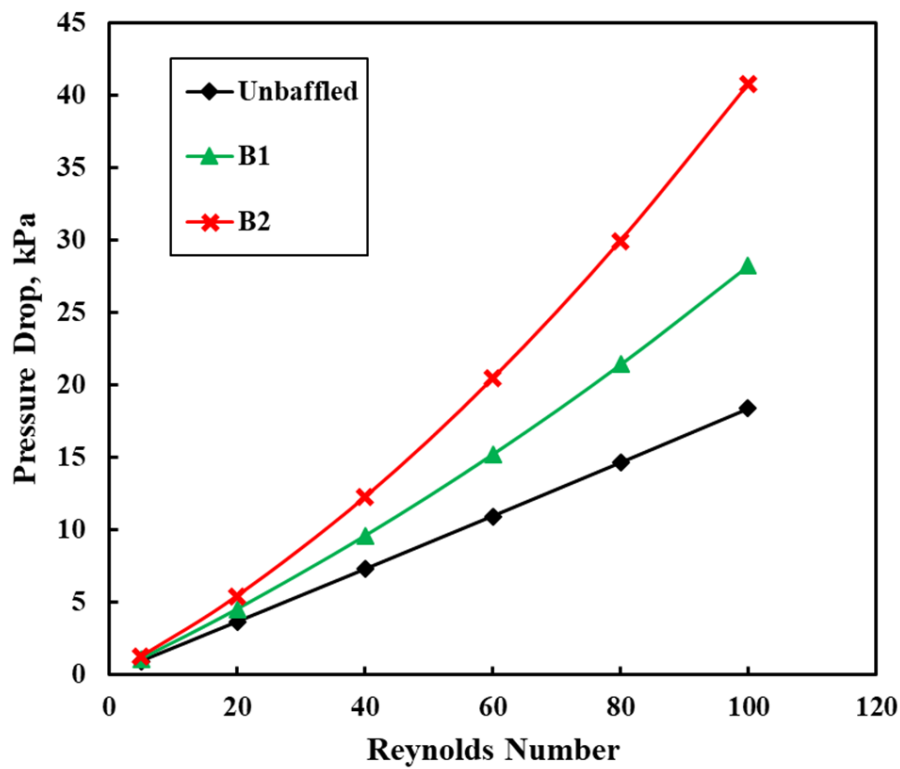


Figure 5.10 Effect of baffle configurations on Pressure drop

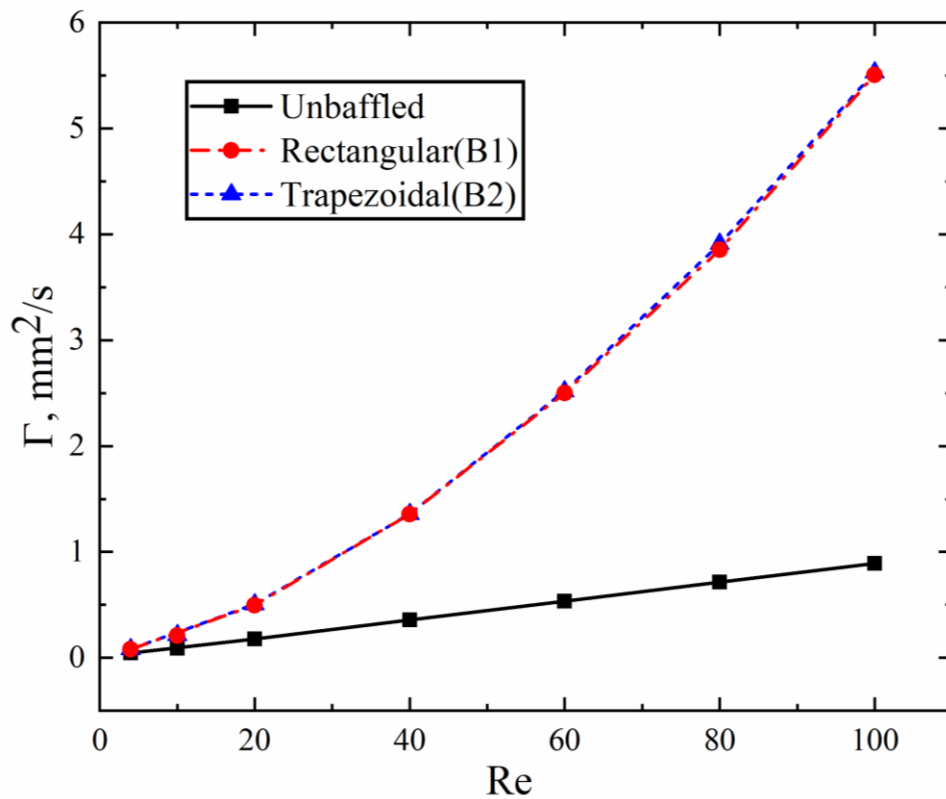


Figure 5.11 Effect of baffle configurations on Liquid Circulation

The axial dispersion model was used to characterize non-ideal mixing in the microchannel. The correlation between the RTD curve and the Peclet number is given by (Levenspiel, 1999; Fogler, 2013)

$$\sigma_{\theta}^2 = \frac{\sigma^2}{\tau^2} = \frac{2}{Pe} + \frac{8}{Pe^2} \quad (5.1)$$

This correlation utilizes the mean residence time (τ), variance of the distribution (σ^2) and Peclet number (Pe). These were calculated and reported in Table 5.2 for various configuration of baffles. It was observed that the mean residence time reduces when baffles were introduced in the microchannel and its value was found to be lower for rectangular baffle configuration. However, the variance and Peclet number were found to be better for trapezoidal baffle configuration. This was attributed to the lower axial dispersion and better mixing than unbaffled microchannel.

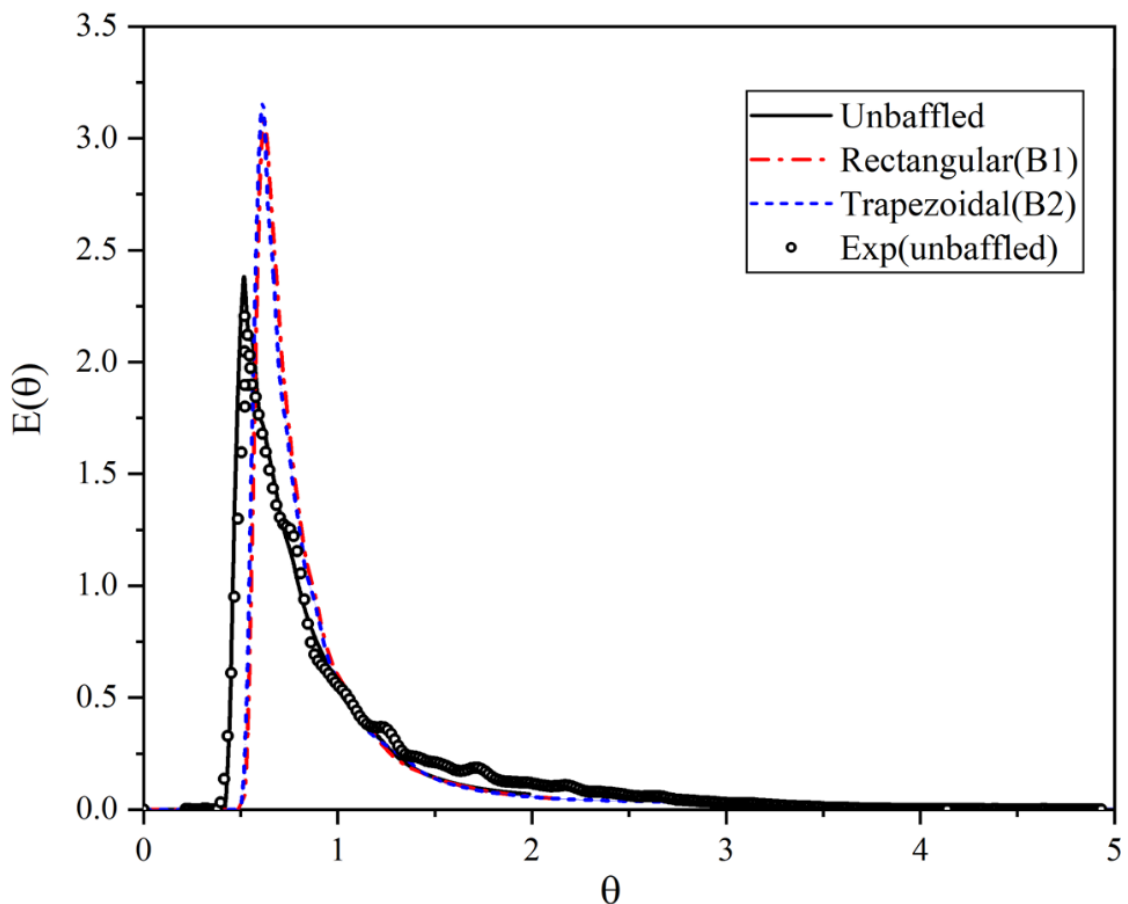


Figure 5.12 Effect of various baffle configurations on normalized RTD function

Further, the performance of the baffled configurations was analyzed by predicting the lateral mixing (mixing index). A vertical plane was chosen at the outlet and the concentration of tracer across the plane was used to calculate the mixing index. This was analyzed for various Reynolds numbers and geometric configurations (unbaffled, rectangular and trapezoidal). In unbaffled microchannel, at low Re, the mixing of fluids occurred primarily due to molecular diffusion. Hence, the mixing index value decreased with Re since the residence time decreased and the time available for diffusion was low. In baffled microchannel, mixing was influenced by both convection (attributed to lateral mixing) and diffusion. Thus, reverse trend was observed for baffled configuration. It was observed that the mixing index was maximum for trapezoidal baffle configuration at lower Reynolds numbers ($Re < 60$). At higher Reynolds numbers, the predicted mixing index value for trapezoidal and rectangular baffles was found to be same. The contours of mass fraction of tracer along the length of the microchannel are depicted in Figure 5.14.

Table 5.2 Effect of baffle configurations on mean residence time, variance and Pe

Configuration	Mean Residence Time, τ (s)	Variance, σ^2	Peclet Number, Pe
Unbaffled (Experiment)	3.38	0.48	6.67
Unbaffled (Simulation)	3.56	0.52	6.25
Rectangular baffles (B1) (Simulation)	3.14	0.46	6.94
Trapezoidal baffles (B2) (Simulation)	3.29	0.43	7.41

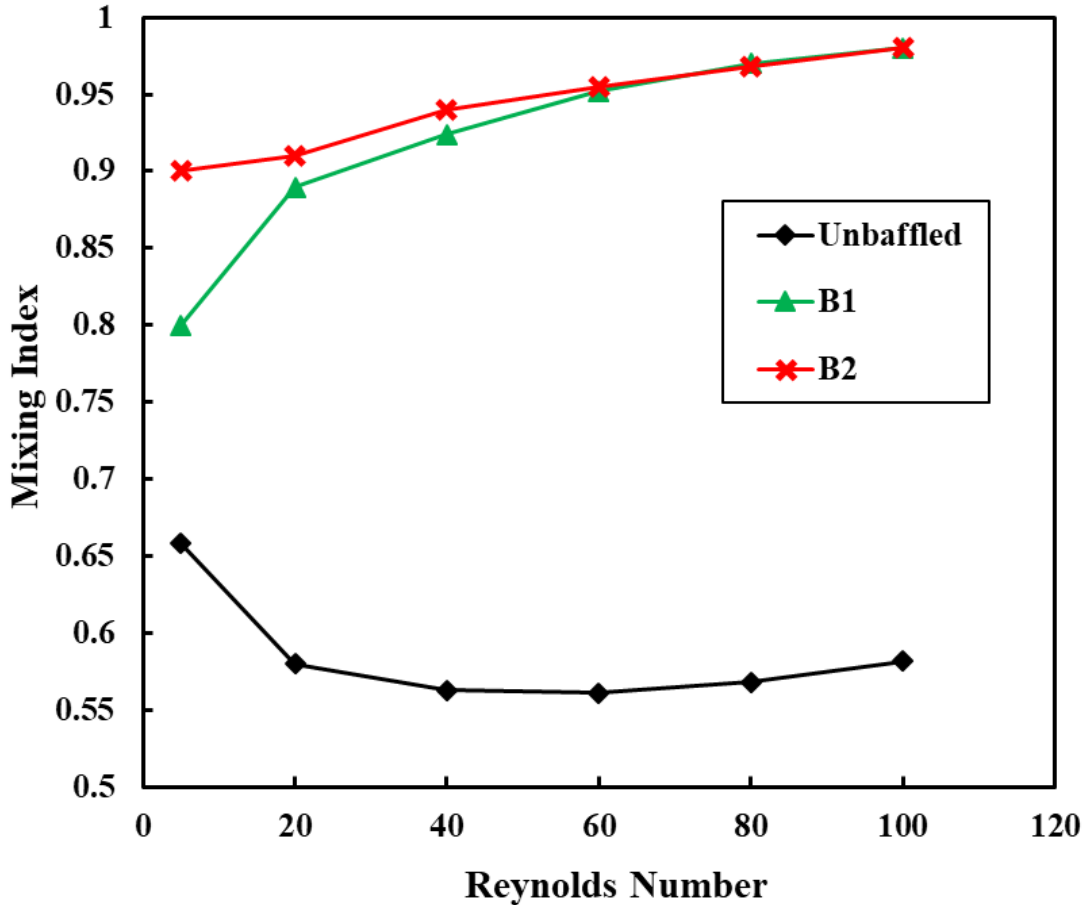


Figure 5.13 Effect of Reynolds number on mixing index for various geometric configurations

In Figure 5.14, red indicates tracer and blue indicates water. The mixing was very low in unbaffled microchannel. In the baffled microchannels, due to the presence of baffles the mixing among the fluid streams improved as they cross the baffles. The mixing was found to be better in trapezoidal baffle configuration at low Re and similar for both baffle configuration at $Re > 60$. In trapezoidal baffle configuration, the placement of alternative converging sections led to the improvement of mixing among the fluid streams. These converging sections led to circulatory patterns in the fluid and improved the mixing. Thus, the trapezoidal baffles support in improving the performance of microchannel (71%).

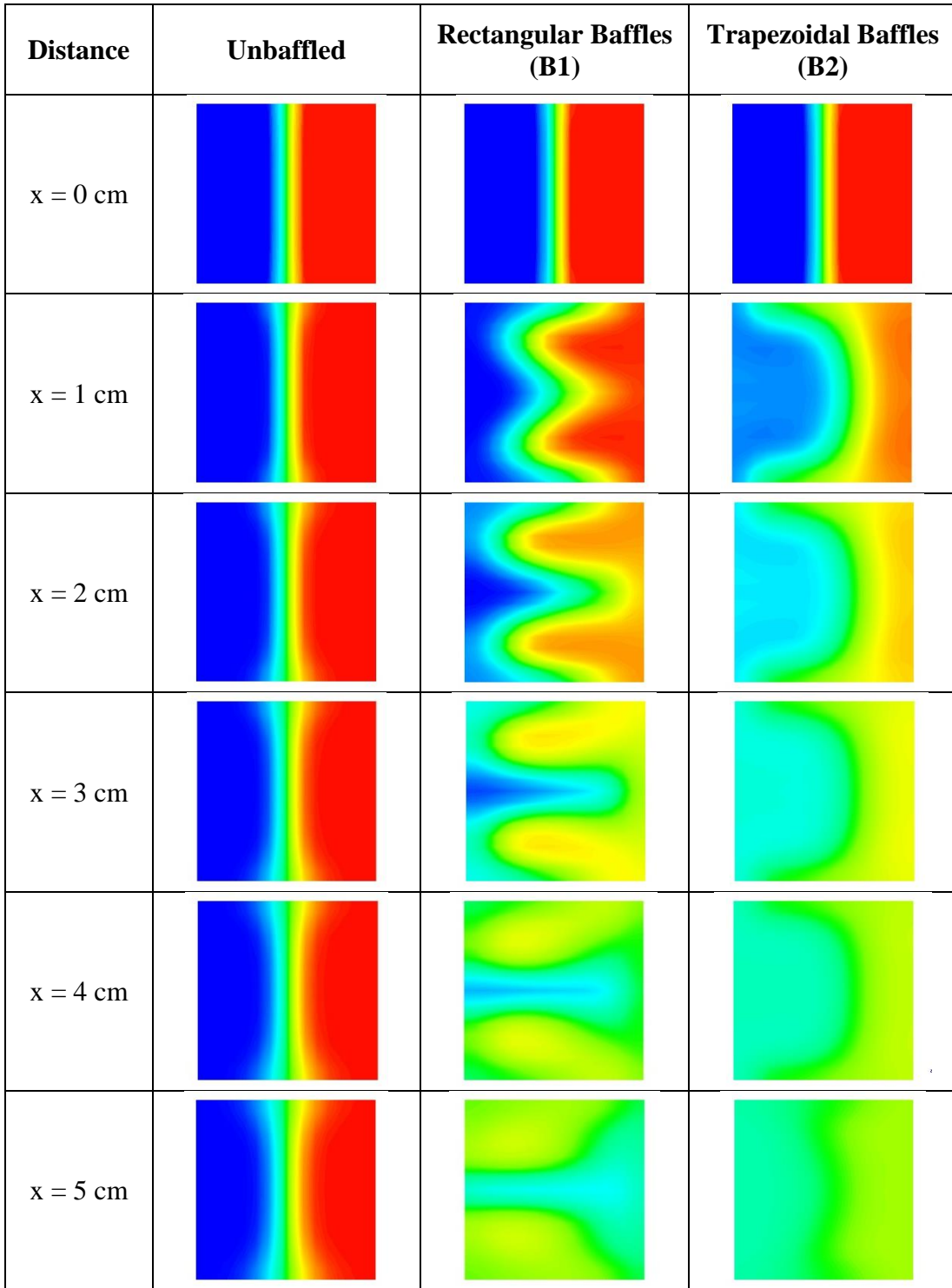


Figure 5.14 Contours of mass fraction of tracer along the length of the microchannel for $Re = 20$

5.2.3. Reaction

To study the effect of the proposed baffle configurations on chemical reactions, a fast neutralization reaction between sodium hydroxide and hydrochloric acid was considered in the microchannel. The performance of the microchannel was numerically investigated using CFD. An equimolar solution (0.1 M) of NaOH and HCl at a velocity of 50 mm/s were introduced through inlet 1 and inlet 2 respectively. The transient CFD simulations were performed with a time step of 0.0005 s to predict the conversion of reactants. The conversion was monitored at the outlet for three geometric configurations as shown in Figure 5.15.

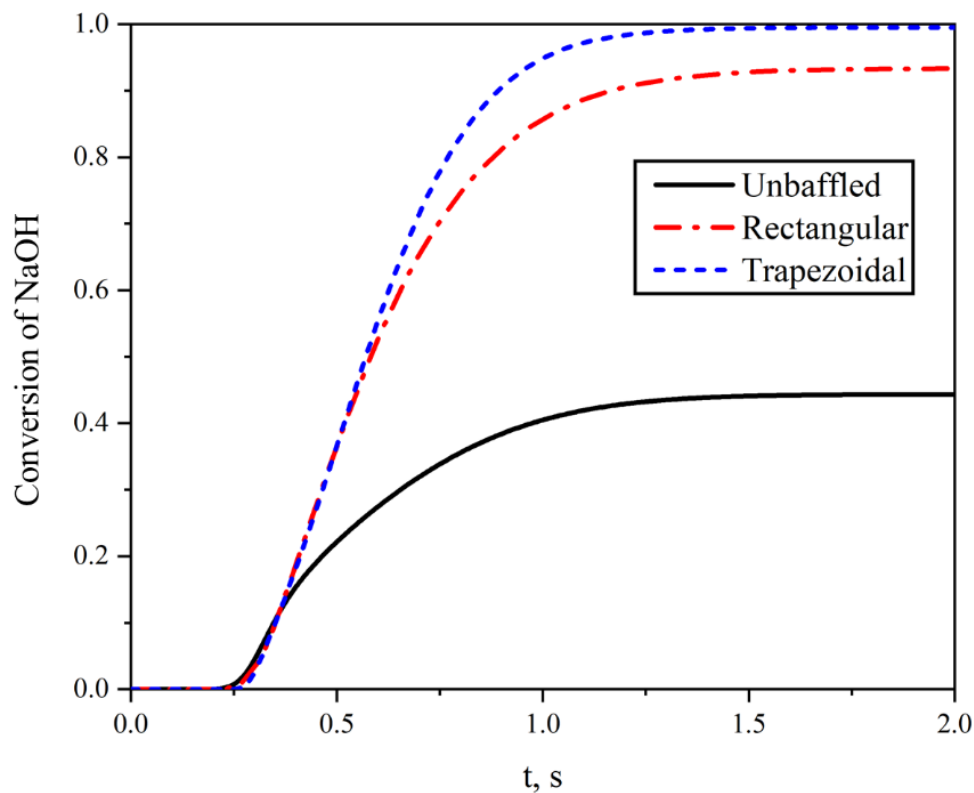


Figure 5.15 Temporal variation of NaOH conversion for various baffle configurations

The predicted conversion for trapezoidal baffle configuration (B2) was found to be larger compared to unbaffled and rectangular baffles (B1). The calculated conversion of NaOH at different Reynolds numbers is shown in Figure 5.16.

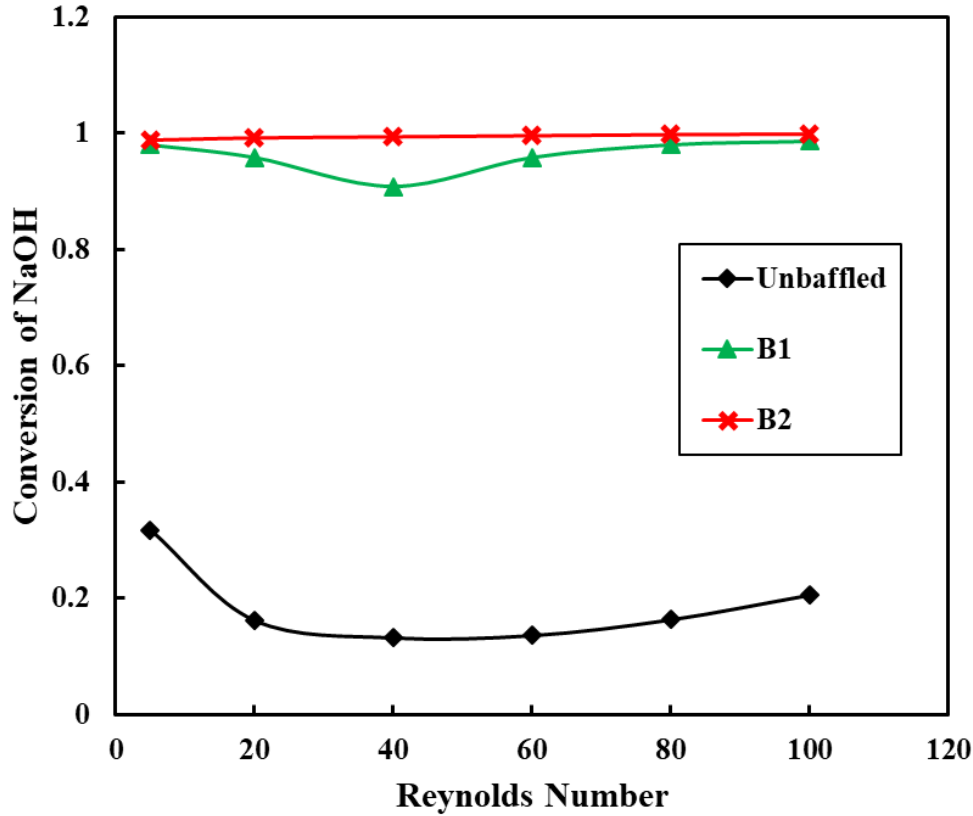


Figure 5.16 Effect of baffle configuration on conversion of NaOH

The conversion was very low (< 0.4) for unbaffled microchannel and high for microchannel with baffles. For B1 configuration, the conversion reduced in the Re range of 5 to 40 and then increased to reach a maximum conversion of 0.98 ($Re = 100$). The B2 configuration showed the maximum conversion close to 1 at all Reynolds numbers. This was attributed to the configuration of baffles in the microchannel. Hence, trapezoidal baffles in the microchannel improve the flow-field, mixing and chemical reactions. However, incorporating such baffle configurations in the microchannel increases pressure drop, which was undesirable. Though these baffle configurations improve mixing performance, they induce high pressure drop and are not suitable for multiphase applications (solid – liquid, gas – liquid) as they obstruct the flow. Thus, in order to improve mixing with low-pressure drop, single-phase flow regimes prevailing in the T-shaped microchannel were exploited.

5.3. Single Phase Flow Regimes

5.3.1. Flow Regimes

To analyze the flow regimes in the T-shaped microchannel, transient 3D simulations were performed for various Reynolds numbers from 5 to 400. The flow regimes were identified and the corresponding Re range is reported in Table 5.3. The predicted contours of velocity magnitude for different flow regimes ($y = 0.1$ mm) are shown in Figure 5.17. The $Re_{critical}$ at which engulfment flow occurs in our system was found to be 300 (inlet velocity = 750 mm/s).

Table 5.3 Flow regimes present in the T-shaped microchannel

Flow Regime	Range
Stratified Flow	$Re < 60$
Vortex Flow	$60 \leq Re < 300$
Engulfment Flow	$Re \geq 300$

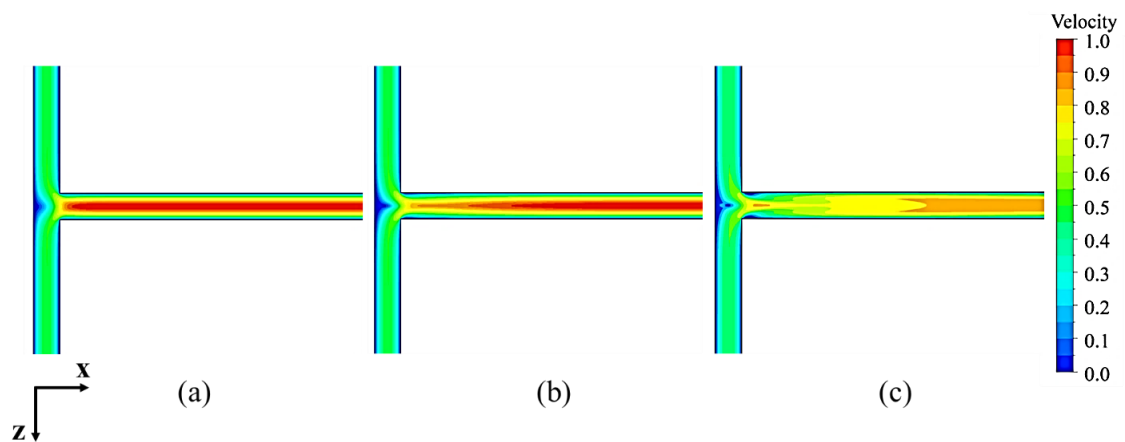


Figure 5.17. Contours of normalized velocity magnitude for (a) stratified flow regime ($Re = 20$), (b) vortex flow regime ($Re = 100$) and (c) engulfment flow regime ($Re = 300$)

The associated streamlines and vectors for various flow regimes are shown in Figure 5.18. The streamlines with blue colour represent the flow of the liquid from inlet-1, and red colour was the flow of liquid from inlet-2.

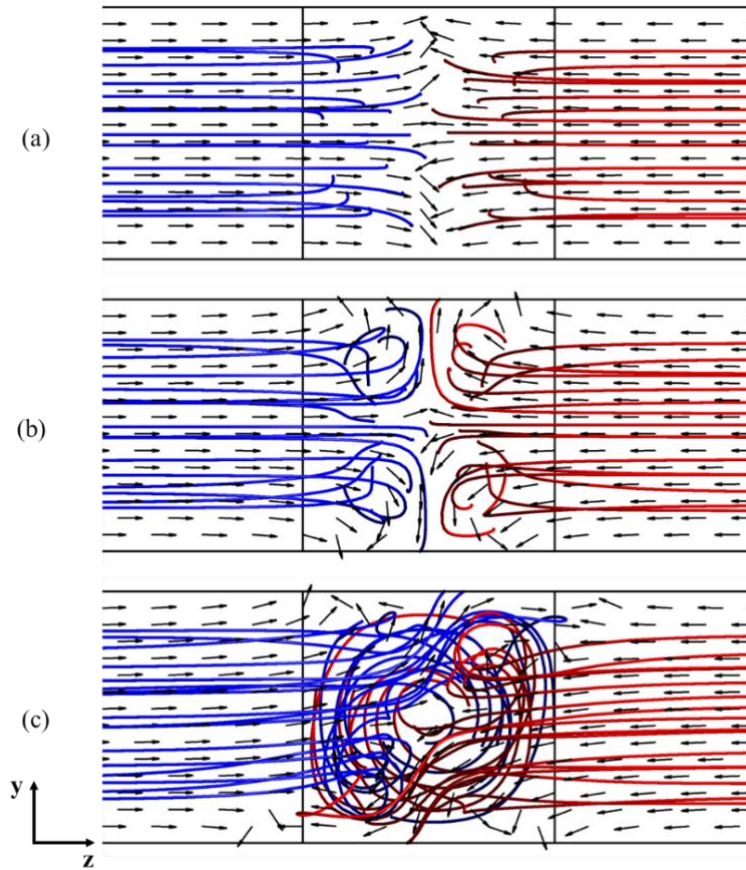


Figure 5.18. Streamlines and vectors corresponding to (a) stratified flow regime, (b) vortex flow regime and (c) engulfment flow regime

These streamlines were observed to be parallel and segregated in Figure 5.18 (a) indicating the presence of a stratified flow regime and occurs at $Re = 20$. In stratified flow, diffusion plays a dominant role. Further increase in velocity of inlet fluid stream, four counter-rotating vortices were observed at $Re = 100$ with weak interaction between them indicating vortex flow regime [Figure 5.18 (b)]. In vortex flow, diffusion is dominant at the vortex interface and advection is dominant inside the vortices. Further increase in the fluid velocity, strong interaction between two counter-rotating vortices was observed at $Re > 300$ [Figure 5.18 (c)]. The strong interaction of vortices indicates engulfment flow regime and this regime promotes mixing of fluid streams significantly. The engulfment flow regime occurs at high Re and is advection dominant. These flow regimes were validated by comparing the contours of tracer concentration at T-junction with flow visualization experiments (Figure 5.19). The numerical predictions were found to be comparable with the experimental observations.

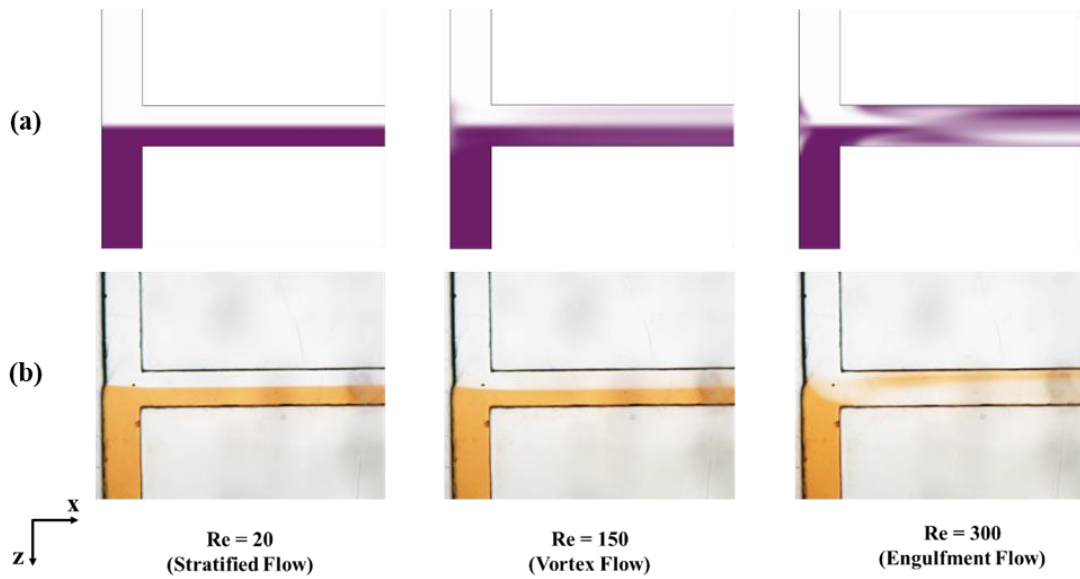


Figure 5.19 Spatial variation of tracer at T-junction for different flow regimes (a) Simulation and (b) Experiment

The mixing performance at different flow regimes was predicted and shown in Figure 5.20. The mixing was low in stratified flow and decreased with increase in Re. As the fluid enters vortex flow regimes, mixing gradually improved. As 300 Re was attained, mixing improved significantly due to engulfment flow regime.

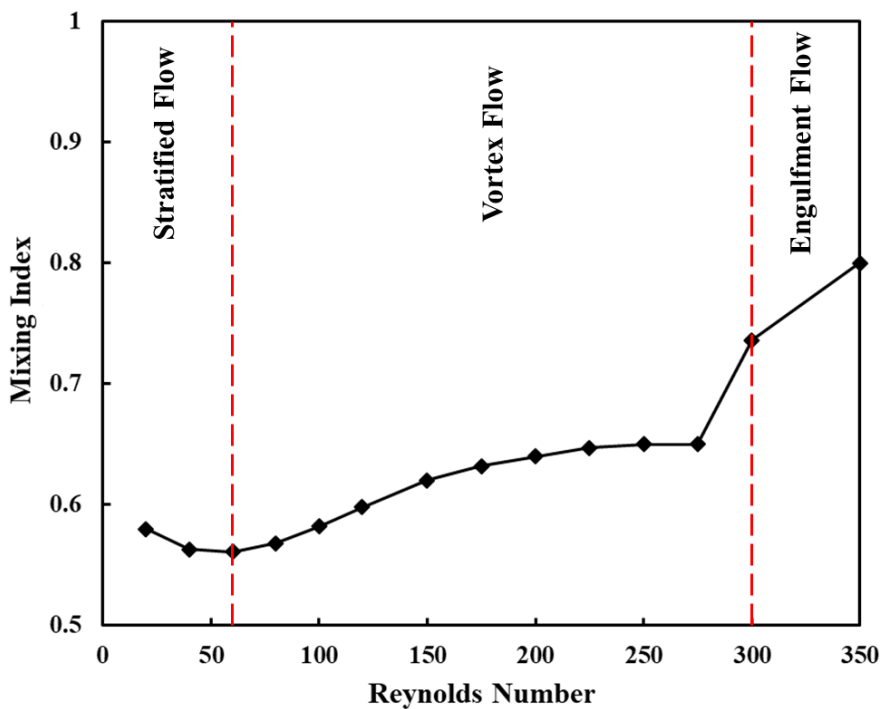


Figure 5.20 Effect of flow regimes on mixing index

The contours of tracer mass fraction in different flow regimes is shown in Figure 5.21. In stratified flow, the mixing was very low. In vortex flow regime, due to the four counter rotating vortices weak interaction of fluids can be observed. It was clearly visible at $Re = 250$. In engulfment flow regime, chaotic interaction of fluids happen and mixing improved significantly.

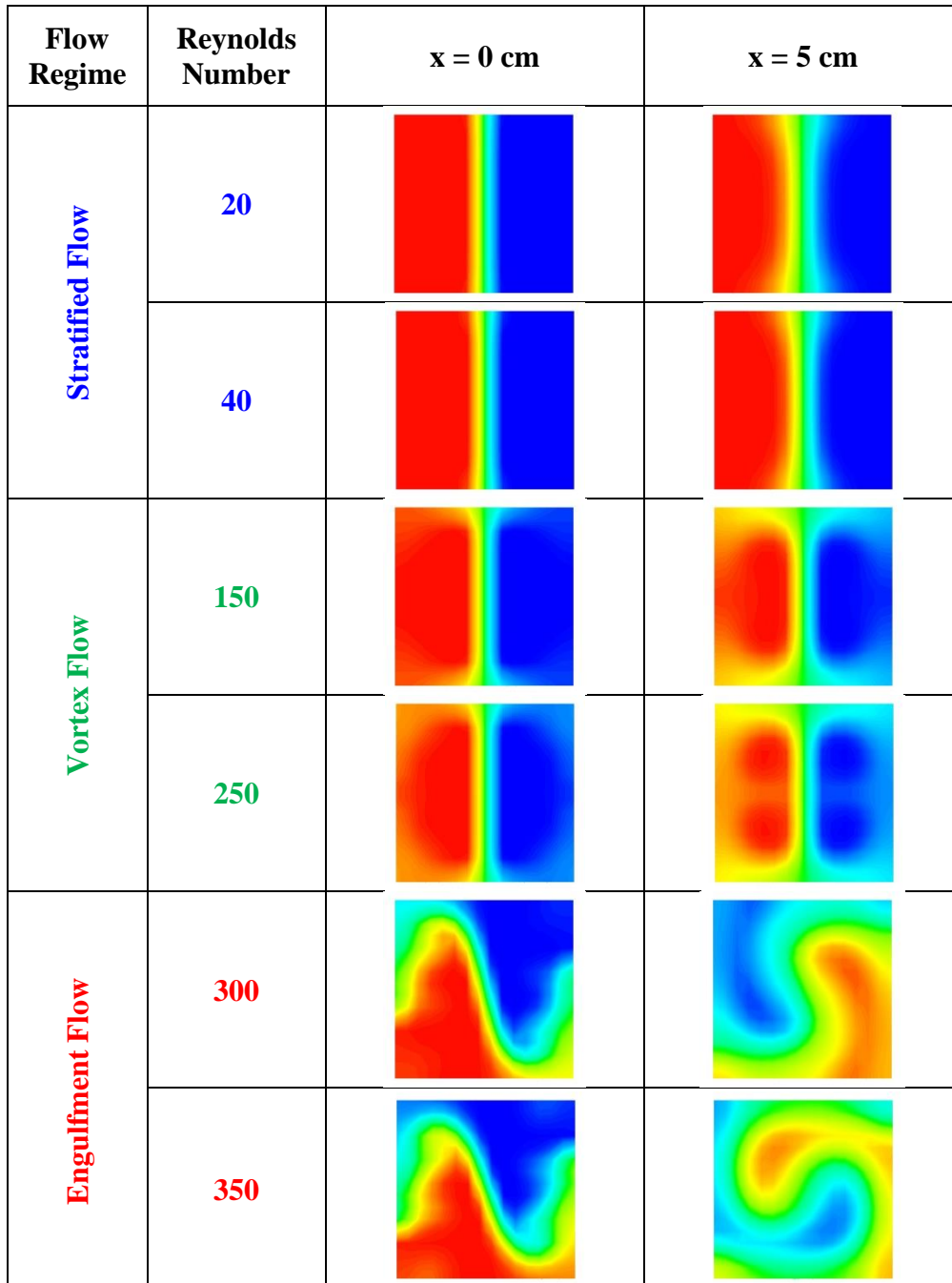


Figure 5.21 Contours of tracer mass fraction at different flow regimes near the entrance and exit of the microchannel

5.3.2. Inlet Modifications

At engulfment flow regime, the calculated pressure drop was found to be very high ($\Delta p = 57.7$ kPa) and the residence time of the fluid elements was very less to achieve complete mixing. Thus, it was not feasible to operate at high Re in practical applications. Hence, in order to achieve engulfment flow regime at low Re, convergent-divergent configurations were proposed at microchannel inlets in the current work as shown in Figure 5.22.

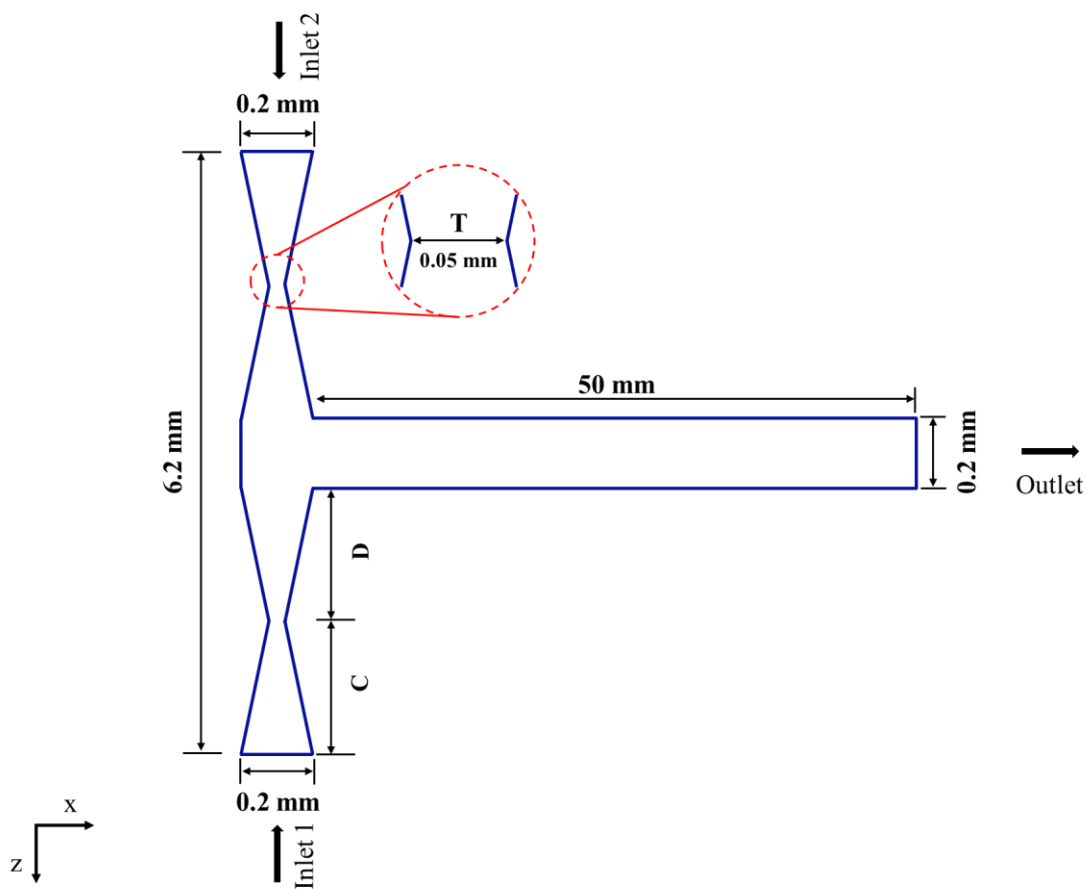


Figure 5.22 Schematic of proposed geometric modifications at the microchannel inlet. (C – convergent section length, D – divergent section length and T – throat width)

The length of the proposed convergent-divergent inlet was 3 mm with 0.2 mm depth and throat was 0.05 mm wide. The length of the convergent and divergent sections was denoted by C and D, respectively. As the ratio of C to D increases, the throat section moves closer to the T-junction. Here five different convergent-divergent inlet configurations (Table 5.4) were considered to obtain engulfment flow regime at

low Re . The $Re_{critical}$ at which flow transition takes place for these modifications was found by analyzing the flow field for various Re . The magnitude of velocity was found to be higher in the throat section. It was observed that the onset of engulfment takes place earlier for microchannel with modified inlets. Since the C:D ratio was varied systematically, throat section moves accordingly close to the T-junction. Hence, fluid elements were found to interact strongly near the junction and the engulfment flow regime was observed early for the proposed modifications.

Table 5.4. Effect of geometric modifications on $Re_{critical}$ and pressure drop

Modification (C:D)	$Re_{critical}$	Pressure Drop (ΔP, kPa)
No Modifications	300	57.7
1:1	158	33.5
3:1	115	24.2
5:1	90	18.9
7:1	80	16.7
9:1	75	15.2

To quantify the engulfment flow regime further, the effect of the C:D ratio on $Re_{critical}$ and corresponding pressure drops were calculated. The $Re_{critical}$ values are reported in Table 5.4. As the C:D ratio increases, the Re at which engulfment flow regime occurs decreases and the pressure drop value lowers (Table 5.4). The magnitude of pressure drop was found to be minimum for the C:D ratio of 9:1 at which $Re_{critical}$ was 75. Further, the onset of engulfment flow regimes for various C:D ratios at fixed Reynolds number ($Re = 75$) was also analyzed. The streamlines and vectors for various C:D ratios are shown in Figure 5.23. The engulfment flow regime was observed for the modified inlets with C:D ratio of 9:1, whereas the vortex flow regime was observed in other modifications. The flow regimes in the modified microchannel (C:D = 9:1) were validated with flow visualization experiments as depicted in Figure 5.24. The numerical predictions were found to be comparable with flow visualization results.

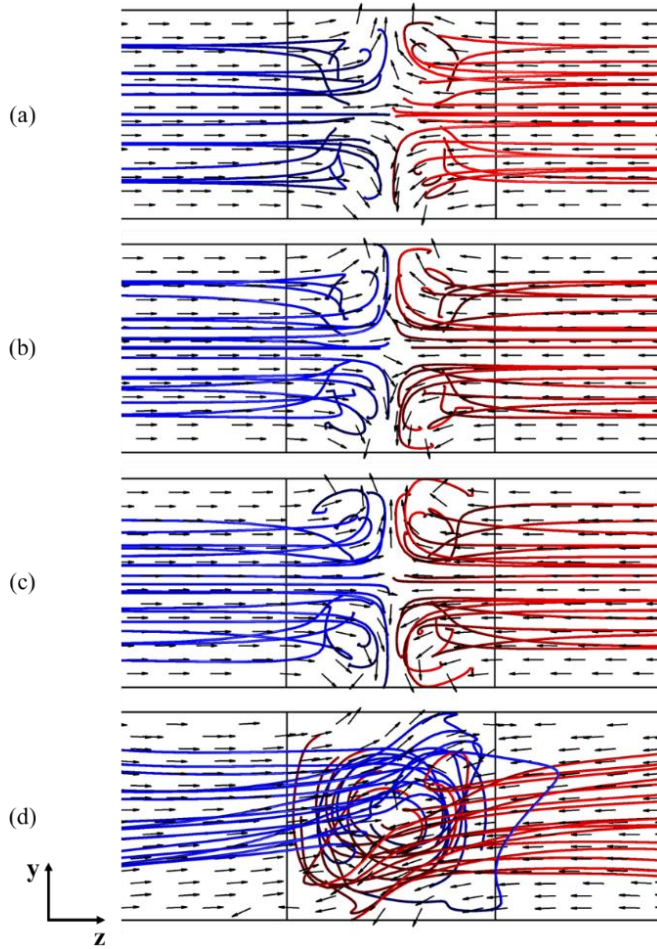


Figure 5.23 Streamlines and vectors corresponding to (a) without modification, (b) $C/D = 1:1$, (c) $C/D = 3:1$ and (d) $C/D = 9:1$ at $Re = 75$

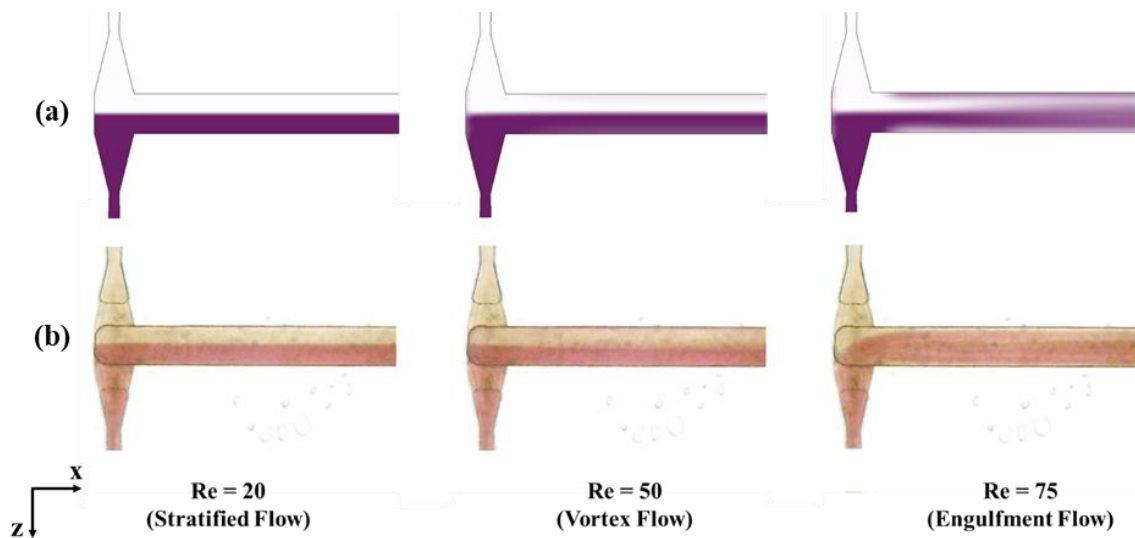


Figure 5.24 Spatial variation of tracer at different flow regimes for modified inlet configuration ($C:D = 9:1$). (a) Simulation and (b) Experiment

5.3.2. Poincaré and Shannon's Entropy

To quantify mixing in engulfment flow regime, mixing index was calculated at $Re = 75$ for various geometric modifications (C:D ratios) and reported in Table 5.5. The effect of these geometric modifications on mixing index is compared as shown in Figure 5.25. The calculated mixing index increased as the C:D ratio was increased. As the throat moves closer to the T-junction, the interaction between both the inlet streams increased and hence the magnitude of mixing index increased. The mixing index was found to be maximum (0.7) when C:D ratio was 9:1. Hence, the ratio of 9:1 was considered to be optimum and predicted hydrodynamics confirms the performance of this configuration.

Table 5.5. Effect of geometric modifications on pressure drop and Shannon's entropy

Modification (C:D)	Pressure Drop (ΔP, kPa)	Mixing Index (MI)	Shannon's Entropy (S)
No Modification	13.7	0.56	3.7
1:1	15.6	0.57	4.2
3:1	15.6	0.58	4.5
5:1	15.6	0.60	4.6
7:1	15.6	0.62	4.7
9:1	15.6	0.65	5.1

To validate the optimum C:D ratio (9:1) further, passive tracer particles were introduced into the system and CFD simulations were performed using Euler - Lagrangian approach. Here injected passive, inert spherical particles ($d_p = 0.001$ mm, $\rho = 998.4$ kg/m³) were tracked by solving Newton's second law of motion through two-way coupling with the continuous phase (Ashraf Ali and Pushpavanam 2011). These particles were injected through both the microchannel inlets once the steady-state flow was obtained. The trajectories of the particles in the microchannel were characterized through the Poincaré map. A section of microchannel was considered near the entrance of the T-junction and location of all the tracer particles was plotted across the cross

section of the microchannel. These plots are called Poincaré maps. Poincaré maps help us in understanding the mixing of fluid streams. The obtained Poincaré maps across the microchannel for various C:D ratios for fixed $Re = 75$ are shown in Figure 5.26.

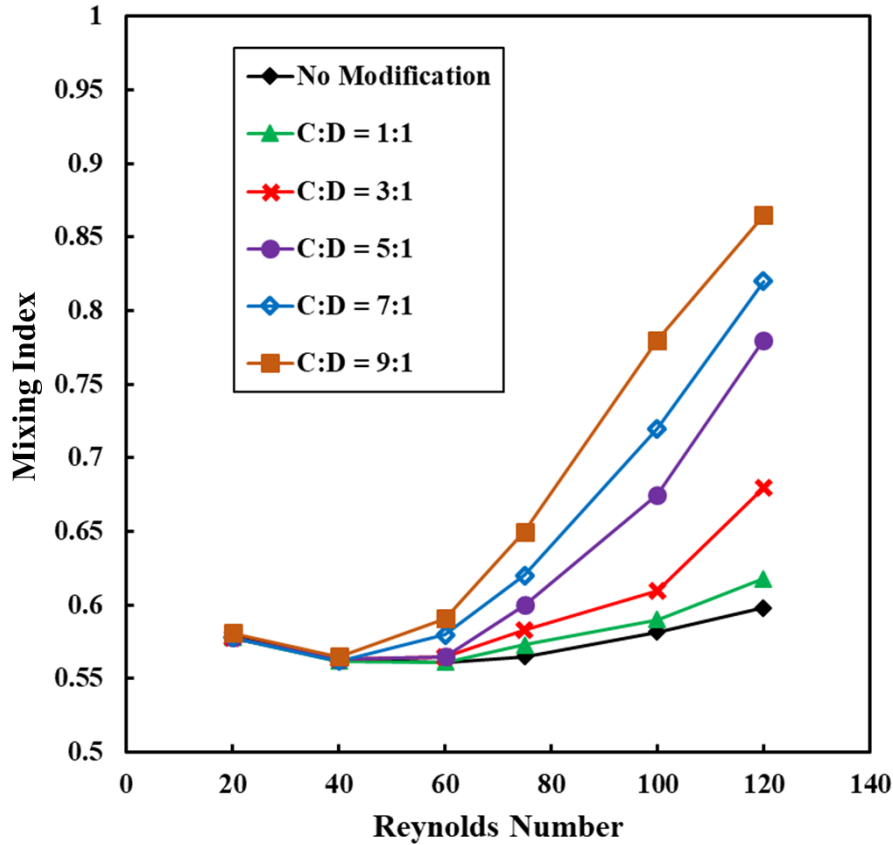


Figure 5.25 The effect of convergent – divergent inlets on mixing index

The particle distribution in the Poincaré map [Figure 5.25 (a)] was characterized by symmetric regions when no modifications were imposed in the microchannel. The presence of these regions implies that mixing was not significant in these domains. When the geometric modifications were incorporated in the microchannel inlets, particles position in Poincaré map disintegrates and the uniform chaotic region diverges. These regions are depicted in Figure 5.25 (b) and it happens when the C:D ratio was 1:1. The calculated particle trajectories when C:D ratio was 3:1 were similar to the trajectories of 1:1 since vortex flow regime prevails in both the cases [Figure 5.25 (c)]. The particle trajectories in the Poincaré map in Figure 5.25 (d) were characterized by highly chaotic and uniform distribution when C:D ratio was 9:1. The non-uniform distribution was attributed to the presence of engulfment flow regime at $Re = 75$ and these chaotic regions enhance mixing quality in such regimes. Hence, the convergent

to divergent ratio of 9:1 was found to be more advantageous in achieving chaotic mixing. Since the Poincaré map predictions provide qualitative insights of chaotic mixing in the microchannel, Shannon's entropy was used to quantify mixing in engulfment flow regime.

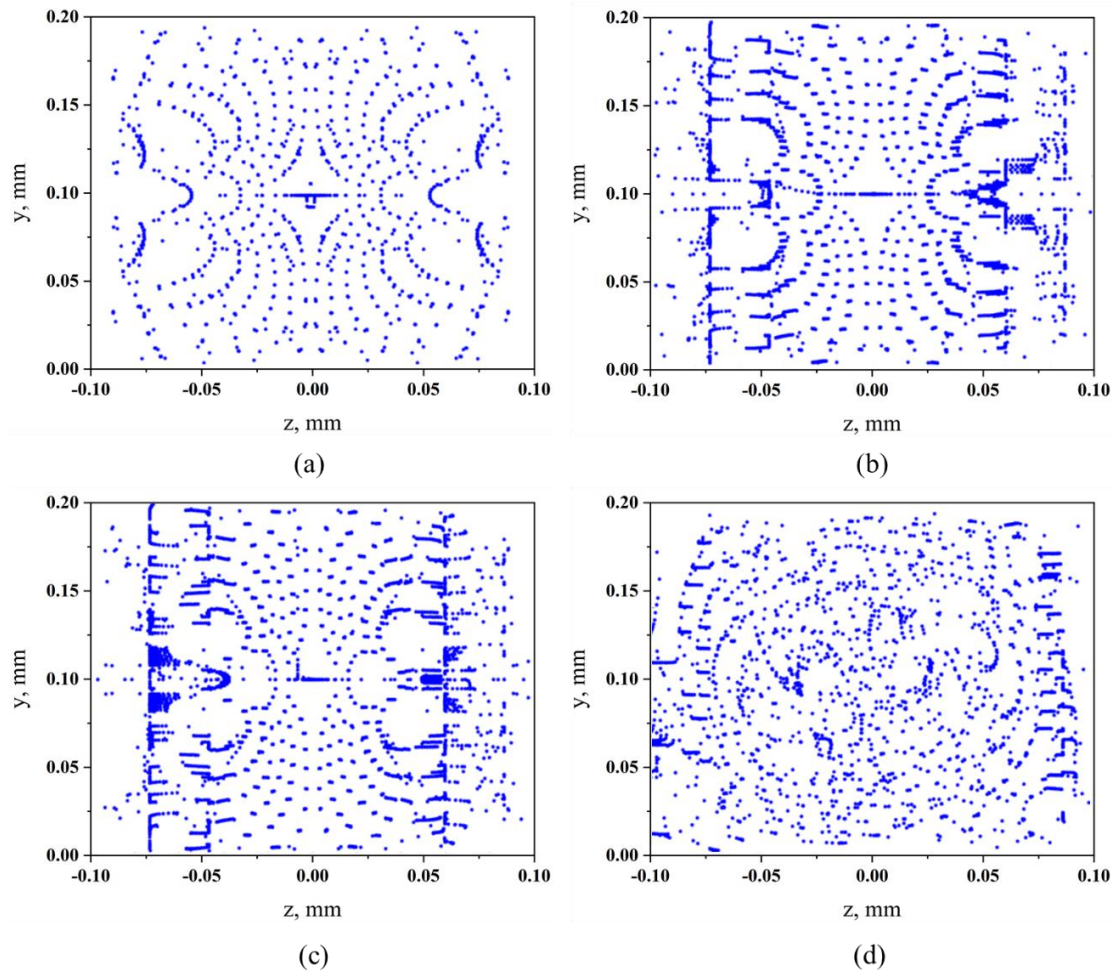


Figure 5.26 Poincaré map in the engulfment region for (a) no modification, (b) $C/D = 1:1$, (c) $C/D = 3:1$ and (d) $C/D = 9:1$

The Shannon's entropy was calculated using the particle positions from Poincaré maps. The cross-section of the microchannel was subdivided into 400 equally sized bins. The probability of finding particles in each bin was calculated using equation 4.11 to find spatial homogeneity across the microchannel. Then the Shannon's entropy was calculated using equation 4.10. The Shannon's entropy was calculated for various C:D ratios of the microchannel inlets at $Re = 75$ and reported in Table 5.5. The value of Shannon's entropy was found to be maximum (relatively good mixing) for the C:D ratio of 9:1 and minimum (poor mixing) for the microchannel without convergent-divergent

inlets. The high Shannon's entropy value signifies the extent of uniform distribution of particles across the cross-section of the microchannel for the proposed modification when the C/D ratio was 9:1. This happens at a relatively low Reynolds number ($Re = 75$) at which the engulfment flow regime was observed. Thus, the convergent-divergent inlets in the microchannel help to achieve engulfment flow at a lower Reynolds number and hence significant extent of mixing.

5.4. Micromixing in T-shaped Microchannels

5.4.1. Effect of Reynolds number on Micromixing

To characterize micromixing in the microchannel at different flow regimes, the spatial variation of vorticity magnitude was analyzed at a horizontal ($y = 100 \mu\text{m}$) and vertical plane ($x = 100 \mu\text{m}$). This is shown in Figure 5.27.

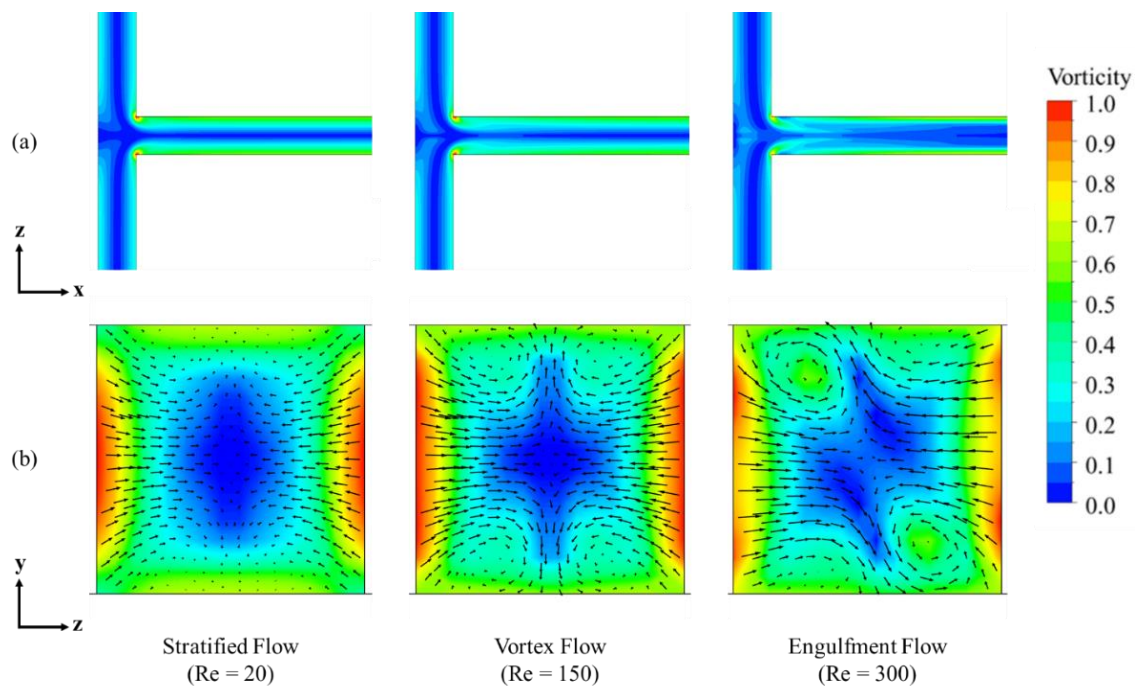


Figure 5.27 (a) Contours of normalized vorticity at a horizontal plane ($y = 100 \mu\text{m}$) and (b) contours of normalized vorticity along with velocity vectors at a vertical plane ($x = 100 \mu\text{m}$) near the entrance of the microchannel for different flow regimes

In the stratified flow regime (Figure 5.27b), no vortices were observed, whereas four weak counter-rotating vortices were found in the vortex flow regime. In the engulfment flow regime, strong vortices were observed near the entrance of the T-junction and these vortices enhance mixing in the engulfment flow regime.

The effect of flow regimes on micromixing was characterized by considering consecutive competitive reactions between reactants A and B. These reactants with 0.01M concentration were introduced through microchannel inlets (1 and 2). The yield and selectivity of desired product (R) were calculated at the outlet for different flow regimes using equations 4.24 and 4.25. This is shown in Figure 5.28. The desired

product conversion was observed to increase gradually until 300 Re. A sharp increment in conversion was found at 300 Re. This was attributed to the onset of engulfment flow which enhances mixing among the reactants. The desired product selectivity increased and decreased with the Reynolds number as the stratified flow transformed into vortex flow. The selectivity was found to remain constant in the vortex flow regime. In the stratified flow, the amount of R that reacts with B was low due to insignificant mixing among the fluid elements. Thus, the formation of undesired product (S) was low resulting in higher selectivity. As flow velocity increases and vortex flow regime was attained, four counter-rotating vortices were observed. These vortices significantly increase the concentration of S due to higher interaction between R and B. Hence, the selectivity obtained in this regime was found to be low. The selectivity of R was found to be high in the engulfment flow regime ($Re > 300$) attributed to significant mixing among liquid phase reactants at the T-junction.

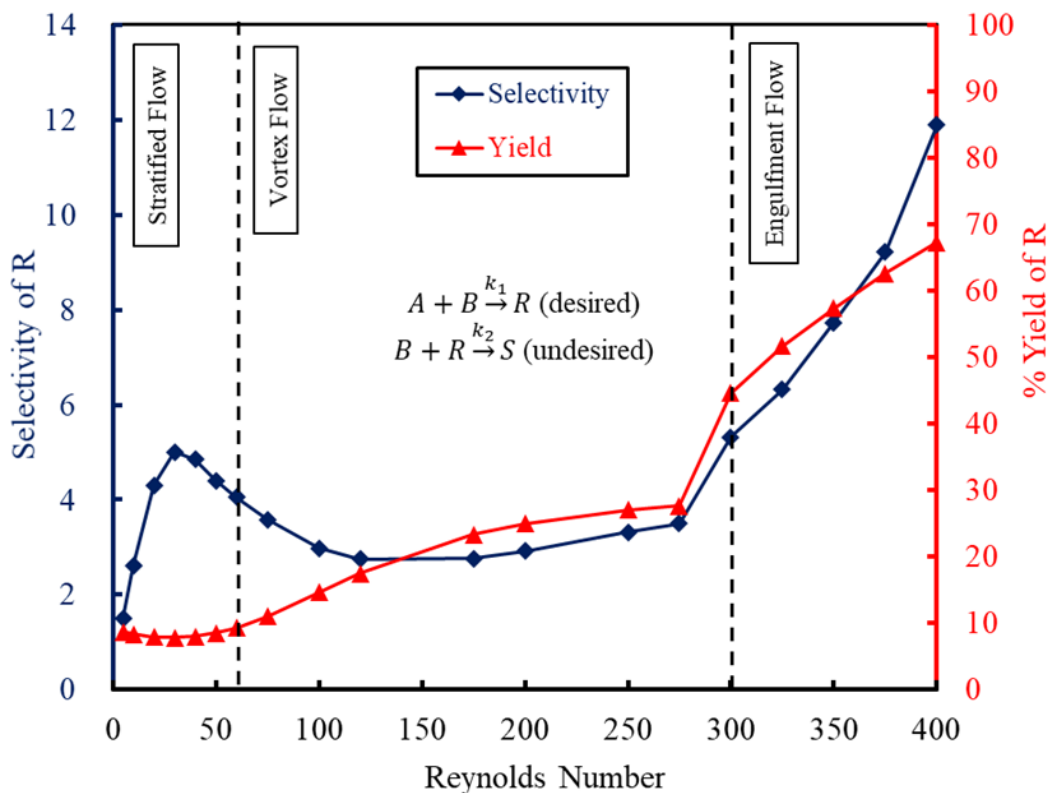


Figure 5.28 Effect of flow regimes on selectivity and percentage yield of R

5.4.2. Effect of Inlet Modifications on Micromixing

To improve micromixing characteristics, convergent-divergent type inlets were introduced. The optimum convergent to divergent ratio (C:D = 9:1) obtained from earlier studies was considered to enhance the micromixing performance. The flow regimes present in the modified microchannel were identified and reported in Table 5.6.

Table 5.6 Flow regimes in the modified microchannel configuration (C:D = 9:1)

Flow Regime	Range
Stratified Flow	$Re < 30$
Vortex Flow	$30 < Re < 75$
Engulfment Flow	$Re \geq 75$

The predicted contours of vorticity magnitude for various flow regimes in modified microchannel were compared with the microchannel without modifications (Figure 5.29). The corresponding vorticity and velocity vectors at a vertical plane ($x = 100 \mu\text{m}$) near the entrance of the microchannel are shown in Figure 5.30.

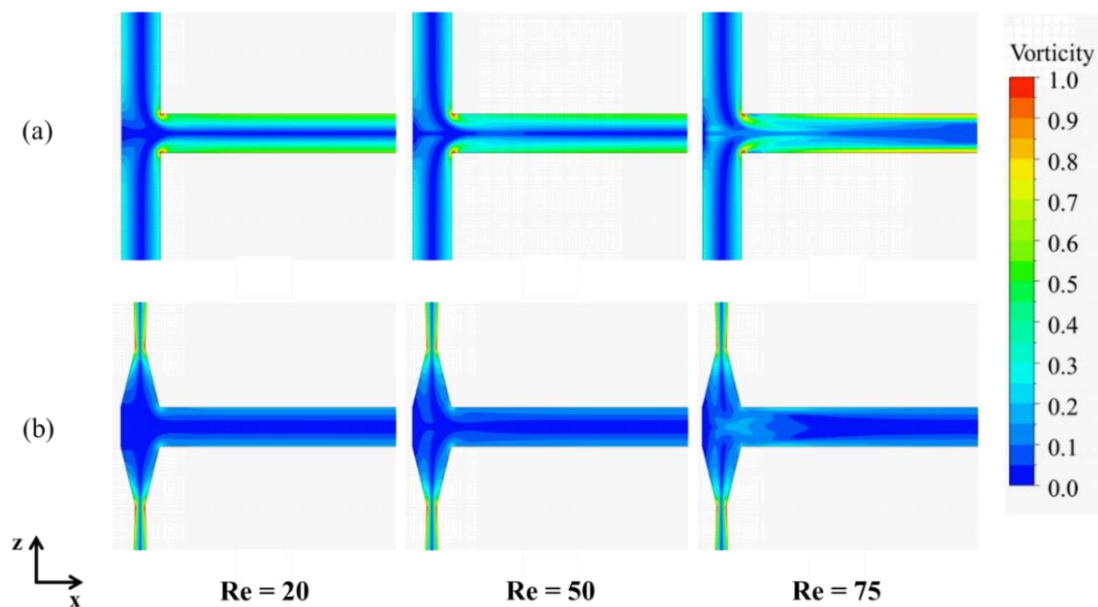


Figure 5.29 Contours of normalized vorticity at a horizontal plane ($y = 100 \mu\text{m}$) for (a) microchannel without modification and (b) microchannel with 9:1 convergent divergent inlets

At $Re = 75$, weak vortices were observed with vortex flow regime in the microchannel without modifications [Figure 5.30(a)] and strong vortices with engulfment flow regime were observed in modified microchannel [Figure 5.30(b)]. The calculated pressure drop for various Re is shown in Figure 5.31(a). The pressure drop was found to be 18% higher for microchannel with convergent-divergent inlet configuration. Once again, liquid circulation rate at the flow channel entrance was calculated for various Reynolds numbers, as depicted in Figure 5.31(b). This was analyzed for both microchannel configurations. The calculated liquid circulation rate was observed to be significantly high in the microchannel with convergent-divergent inlets.

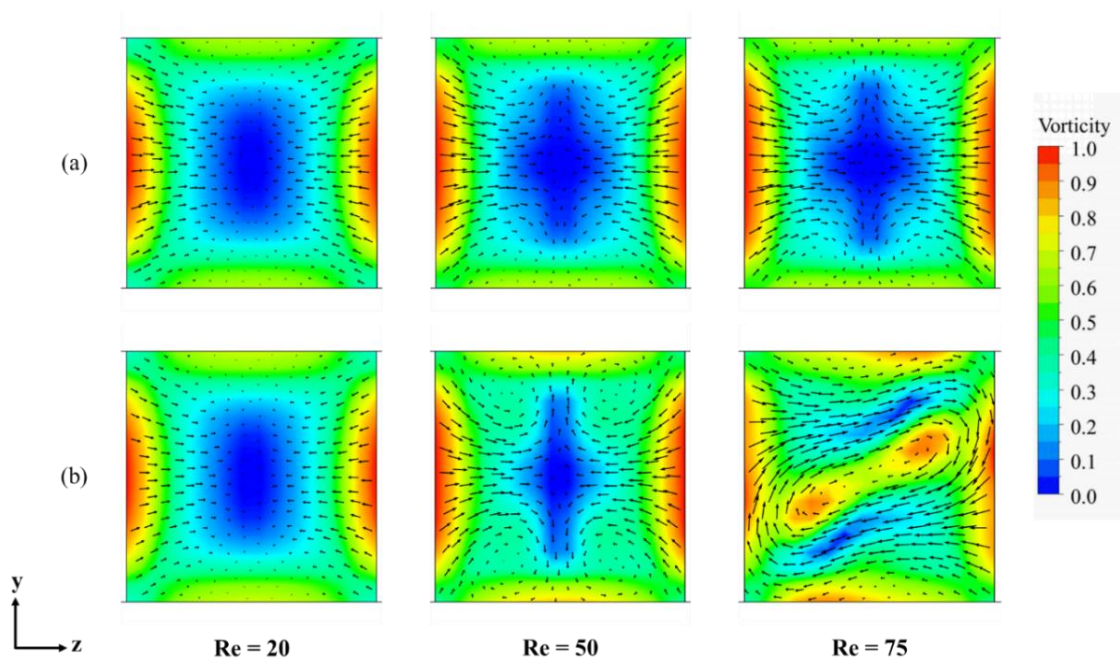
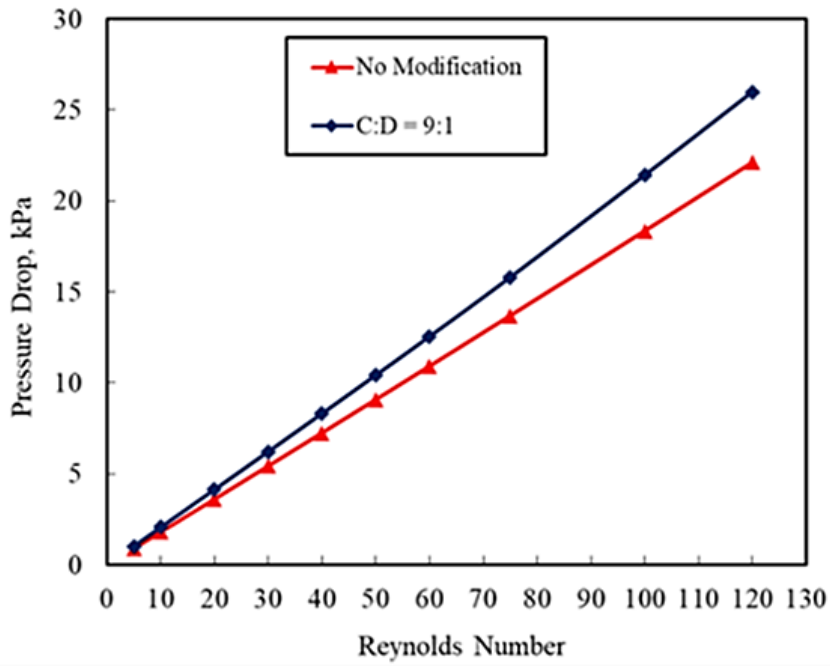
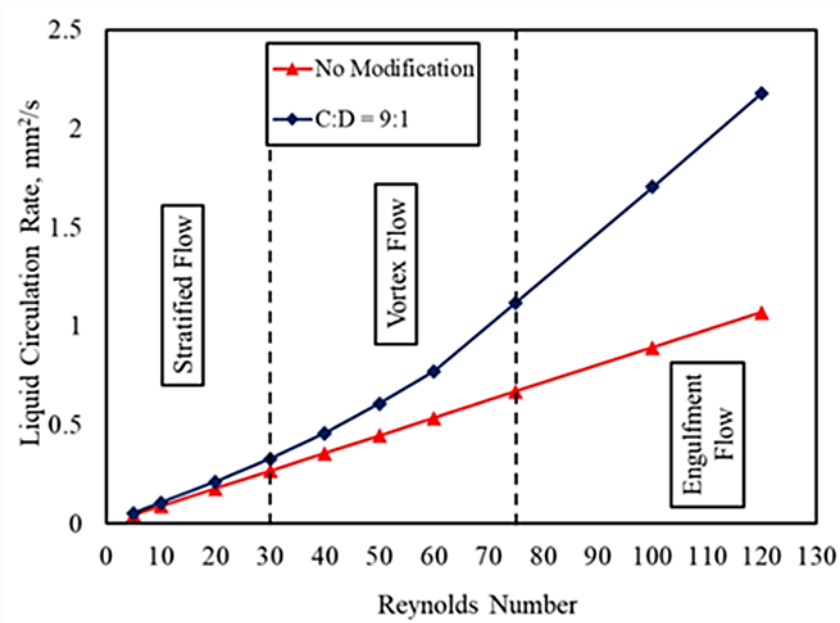


Figure 5.30 Contours of normalized vorticity along with velocity vectors at a vertical plane ($x = 100 \mu\text{m}$) near the entrance of the microchannel for (a) microchannel without modification and (b) microchannel with 9:1 convergent divergent inlets



(a)



(b)

Figure 5.31 Comparison of pressure drop (a) and liquid circulation rate (b) at the entrance for microchannel without modification and with 9:1 convergent - divergent inlets

These predictions were further validated by comparing selectivity and yield of desired product R through consecutive competitive reaction. This is shown in Figure 5.32. The conversion and selectivity were observed to be low in modified microchannel when $Re < 75$ due to vortex flow regime. Their magnitude increases sharply when $Re > 75$. The conversion and selectivity of desired product was found to be significantly higher in modified microchannel. Thus the convergent – divergent inlet configuration (C:D = 9:1) support in enhancing the micromixing performance in the microchannel.

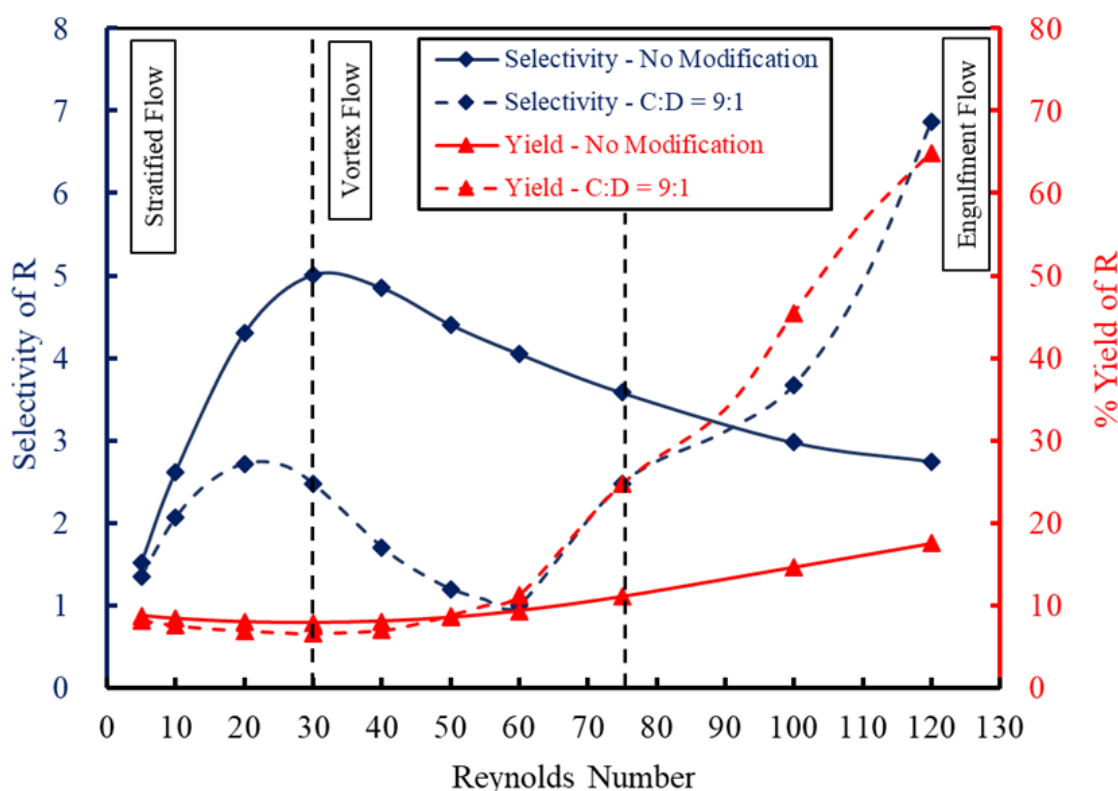
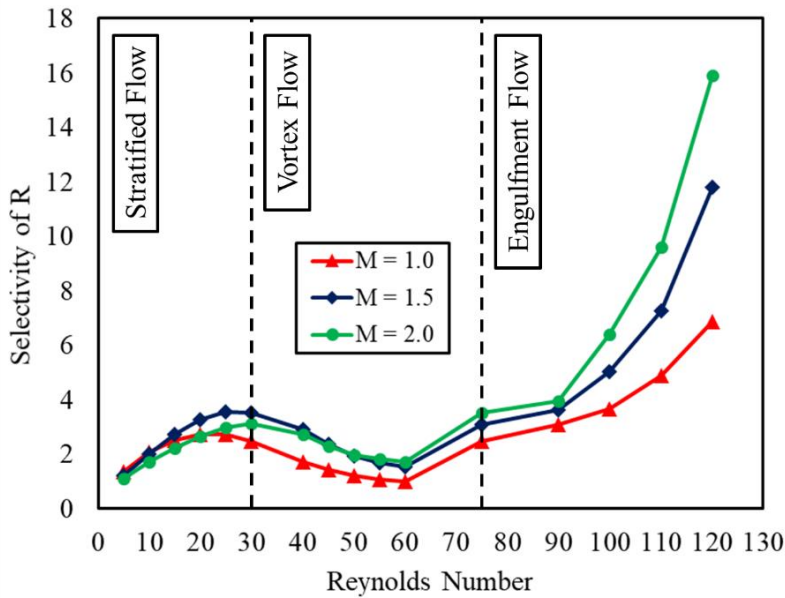


Figure 5.32 Comparison of selectivity and yield of R for microchannel without modification and with 9:1 Convergent - Divergent inlets

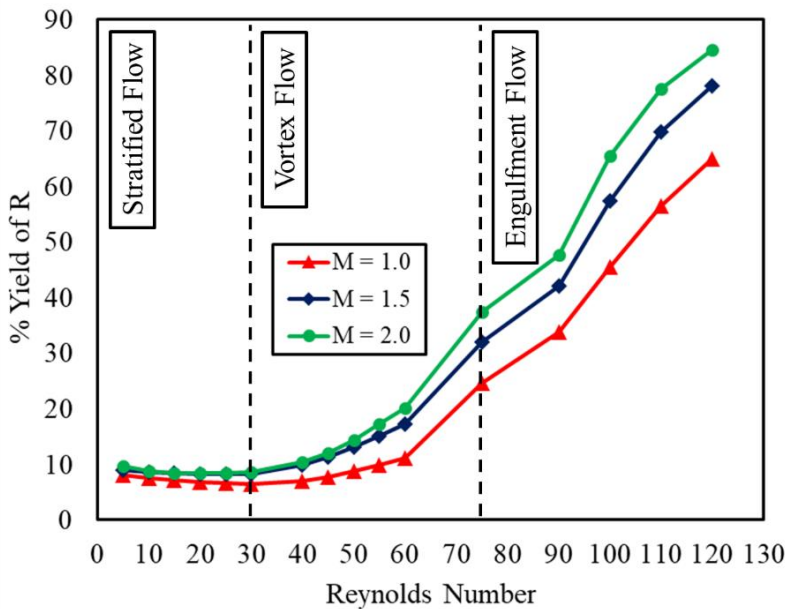
The dependence of selectivity and yield of R on reactant molar ratio (M) was analyzed. Here B was the limiting reactant and the concentration of A was varied (Table 5.7). The effect of M on selectivity and conversion of R is shown in Figure 5.33. The selectivity and conversion of R was found to increase with M. They were found to be high when $M = 2$, which was attributed to the excess concentration of A and insufficient amount of B for the formation of undesired product S. Thus, a higher molar ratio (M) favours micromixing in the microchannel.

Table 5.7 Effect of reactant molar ratio on Selectivity and Conversion of R

Molar Ratio (M)	Selectivity of R		Yield of R	
	Re = 120	% Change	Re = 120	% Change
1.0	6.86	-	0.65	-
1.5	11.8	72%	0.78	20%
2.0	15.9	131%	0.85	30%



(a)



(b)

Figure 5.33 Effect of reactant molar ratio on (a) selectivity and (b) yield of R

5.4.3. Fluid Particle Interactions

The extent of micromixing was further quantified for various flow regimes by introducing buoyant fluid particles at both the inlets. The motion of the particles was tracked through the Lagrangian approach and the interactions between the particles were predicted as they move along the length of the microchannel. Accordingly, mixing behaviour was characterized by predicting the collision rate of particles per unit time for different flow regimes (Figure 5.34).

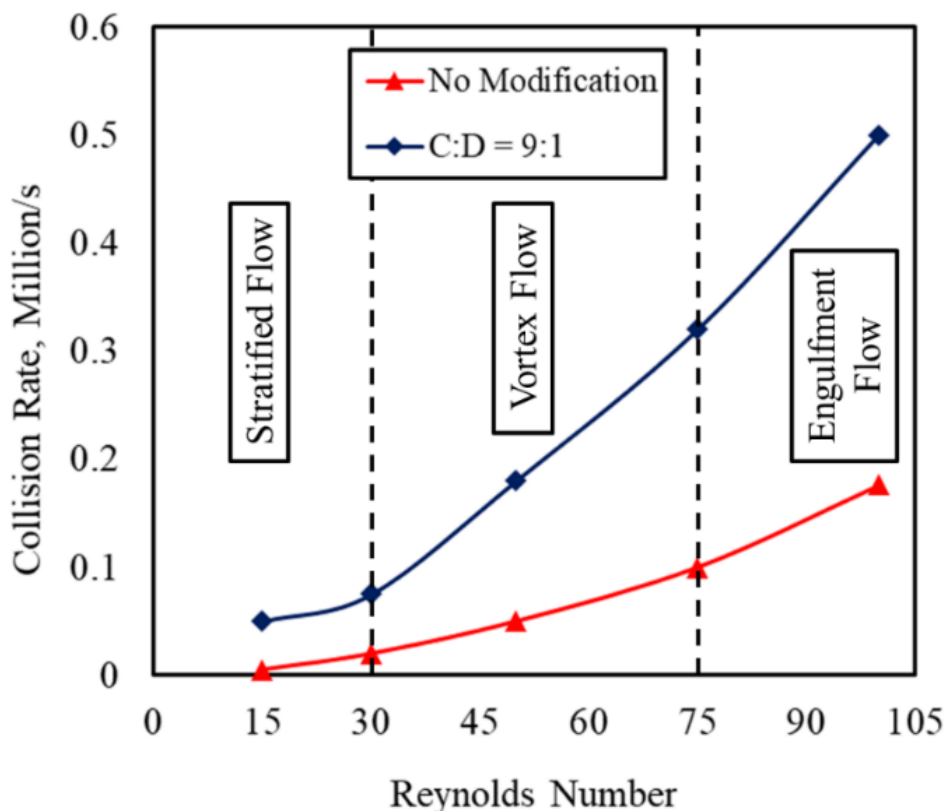


Figure 5.34 Effect of flow regimes on collision rate of buoyant fluid particles in the microchannel

The predicted collision rate among the fluid elements was found to be low in stratified flow regime and high in engulfment flow regime. In stratified flow, the collisions take place at the centre of the microchannel as fluid flow takes place side by side and hence low mixing (low conversion of R). Further, in vortex flow regime, the collisions were confined to four separate regions (leads to excess formation of S and lower selectivity of R) due to the presence of weak counter-rotating vortices. The

collision rate was relatively higher compared to stratified flow regime. In the engulfment flow regime, collisions were found to increase as the mixing among the fluid elements was high (higher selectivity and conversion of R). These findings were consistent with the predictions of micromixing studies (section 5.4.2). Thus, the engulfment flow regime supports the performance of microreactor and it can be further enhanced by using convergent-divergent type inlet configuration. The microchannel with optimum C-D inlets (C:D = 9:1) was used for further investigations.

5.5. Antisolvent Crystallization

5.5.1. Grid Independence

To determine the optimum grid size for the multiphase problem of antisolvent crystallization, grid independence study by considering three different grid sizes (12 μm , 10 μm & 8 μm). The simulations were performed by injecting saturated solution of NaCl in water from inlet-1 and pure ethanol from inlet-2 for Re of 75 and channel length of 1 mm. The predicted crystal size distribution (CSD) for different grid sizes is shown in Figure 5.35. The crystal yield and mean crystal size is depicted in Table 5.8.

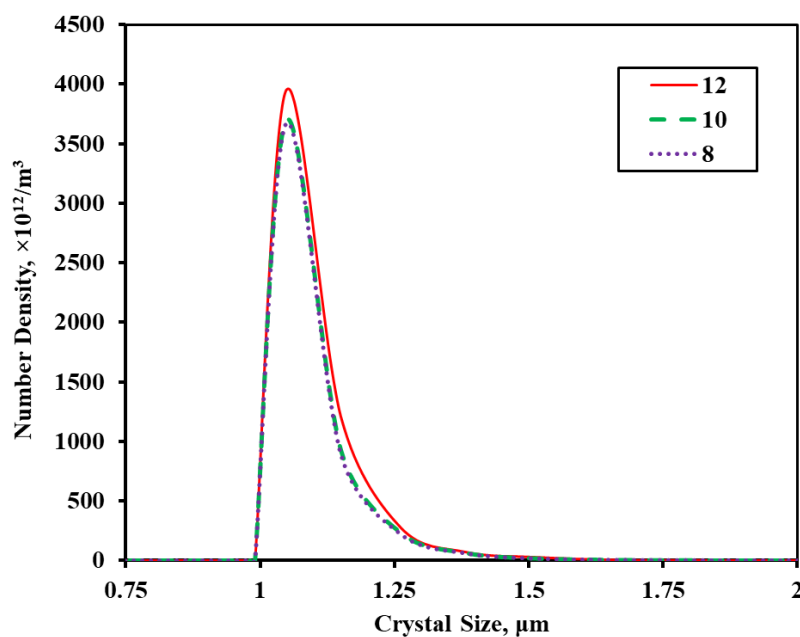


Figure 5.35 Crystal size distribution for various grid sizes (in μm).

Table 5.8 Crystal yield and mean crystal size for various grid sizes.

Grid Size (μm)	No of Elements (Million)	Crystal Yield	Mean Crystal Size (μm)
12	0.5	0.0643	1.160
10	1.1	0.0618	1.084
8	2.2	0.0619	1.083

It was observed that there was significant deviation in the results obtained from 12 μm grid compared to 10 μm & 8 μm grids. The CSD, crystal yield and mean crystal size are found to be similar with very less error. Thus to reduce computational time, 10 μm grid size is used for all further simulations.

5.5.2. Effect of C-D inlets & Reynolds Number

The optimized microchannel (C:D = 9:1) was used for the application study of antisolvent crystallization of NaCl in the water-ethanol system. The time scale for antisolvent crystallization is very small compared to other crystallization methods. Since the residence time in a microchannel is also very small, antisolvent crystallization was considered for this study. The solubility of NaCl in water-ethanol system was obtained from Galleguillos et al., (2003) as shown in Figure 5.36.

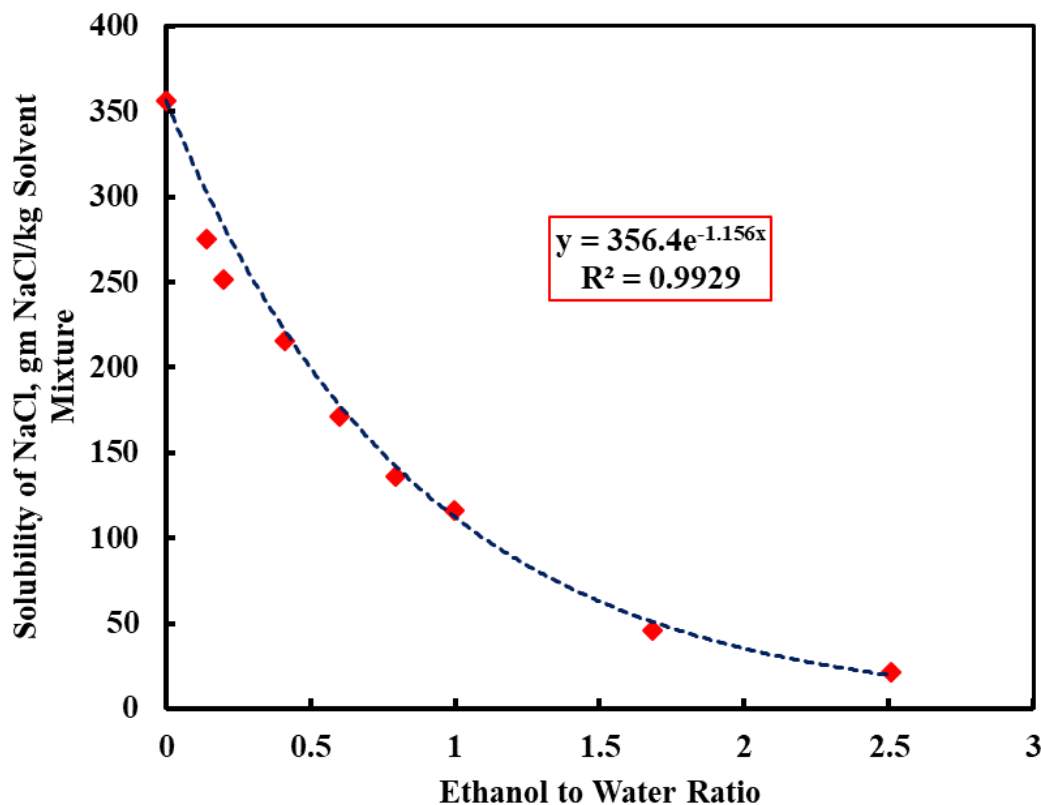


Figure 5.36 Solubility of NaCl in Water-Ethanol Mixture

The simulations were performed by injecting saturated solution of NaCl in water from inlet-1 and pure ethanol from inlet-2. The predicted contours of mass fraction of NaCl in the solvent mixture at different Re is depicted in Figure 5.37. It was observed that as the Reynolds number increases the flow regime changes and mixing of both the fluid streams increases. Stratified flow (Re = 20), Vortex flow (Re = 50) and Engulfment flow (Re = 75) were observed. The crystal size distribution was predicted for different Re using PBM.

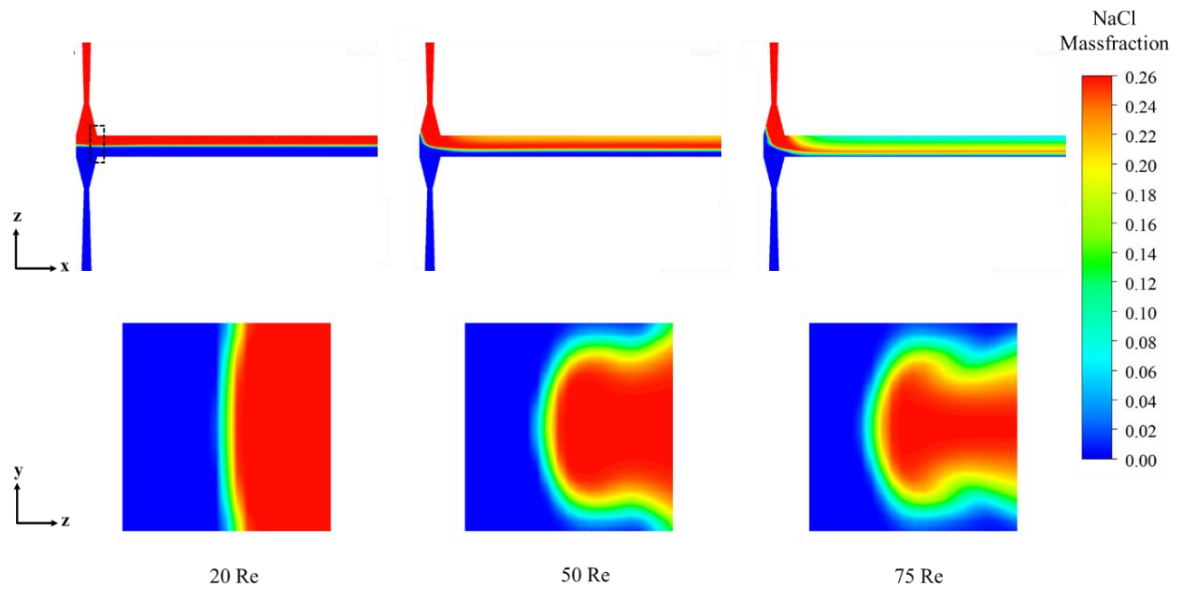


Figure 5.37 Contours of NaCl mass fraction at different Reynolds numbers at $y = 100 \mu\text{m}$ (top) and $x = 100 \mu\text{m}$ (bottom)

At first, the effect of C-D inlets on crystallization was analyzed by comparing the crystal size distribution predicted for the microchannel with and without C-D inlets. This is shown in Figure 5.38. The predicted mean crystal size and yield were reported in Table 5.9.

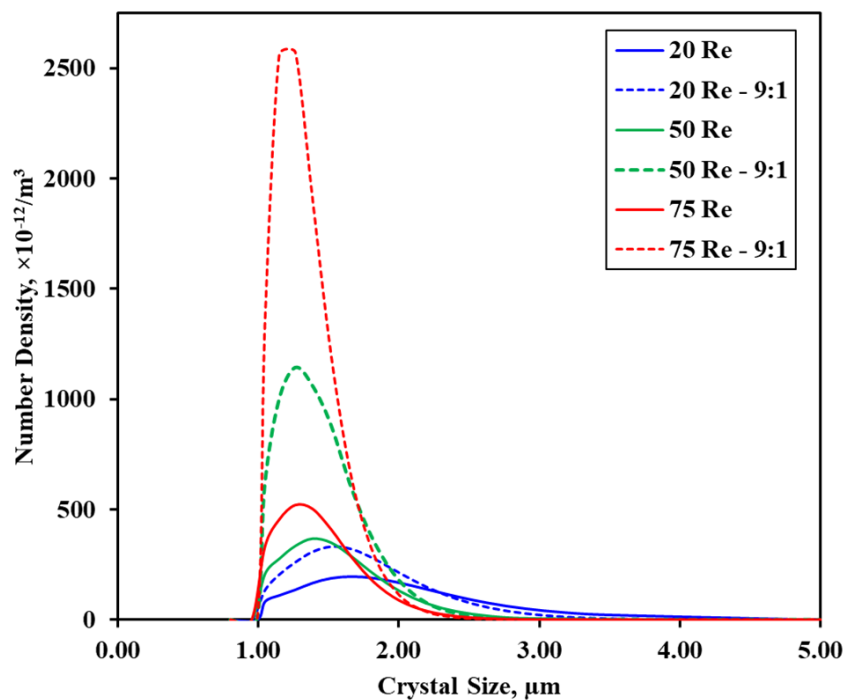


Figure 5.38 Effect of C-D inlets on crystal size distribution

Table 5.9 Effect of C-D inlets on mean crystal size and yield

Re	Mean Crystal Size (μm)		Crystal Yield	
	No Mod	C-D (9:1)	No Mod	C-D (9:1)
20	1.80	1.65	0.17	0.18
50	1.50	1.40	0.14	0.21
75	1.40	1.31	0.11	0.30

It was observed that the crystal size distribution was broader in the case of microchannel without inlet modifications. With the introduction of C-D inlets, narrow distribution was obtained. At $Re = 20$, the crystal yield was found to be similar in both the cases. As Re was increased, the crystal yield in the microchannel with C-D inlets increased significantly. Also smaller size crystals were obtained in the case of modified microchannel due to narrow distribution. Thus, further studies were continued with the microchannel with C-D inlets.

To study the effect of Re , the crystal size distribution (CSD) at the outlet of the microchannel with C-D inlets was predicted and shown in Figure 5.39. It was observed that least number of crystals with a broader CSD were formed for $Re = 20$. At this Reynolds number, stratified flow was observed and the mixing between the inlet streams was minimum (Figure 5.37). As the Reynolds number was increased to 50, mixing has improved due to the formation of vortex flow and crystallization has improved (Figure 5.37). As the Reynolds number was further increased, sharp increase in the crystal yield was observed at $Re = 75$ (Figure 5.41). At this Reynolds number, the onset of engulfment flow takes place and improves the mixing significantly (Figure 5.37). Thus, a narrow distribution was obtained for $Re > 75$. As the Re was increased to 100, the CSD became narrower but not much improvement in crystal yield was observed (Figure 5.41).

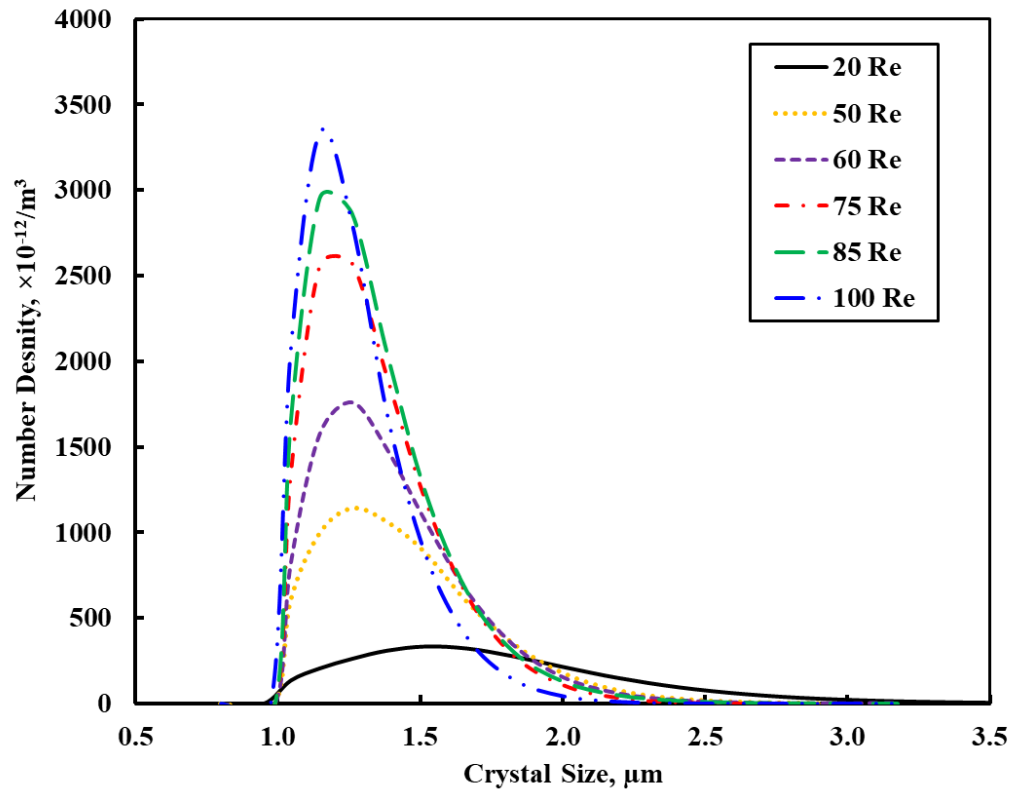


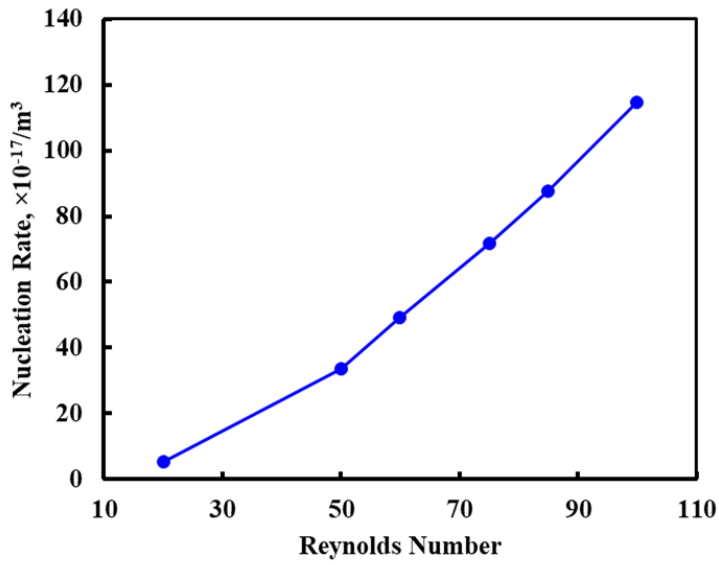
Figure 5.39 Effect of Re on crystal size distribution

The effect of Re on mean crystal size, crystal yield and variance of crystal distribution is shown in Table 5.10. It was observed that the mean crystal size decreased with Reynolds number. This was due to the decrease in the residence time of the crystals.

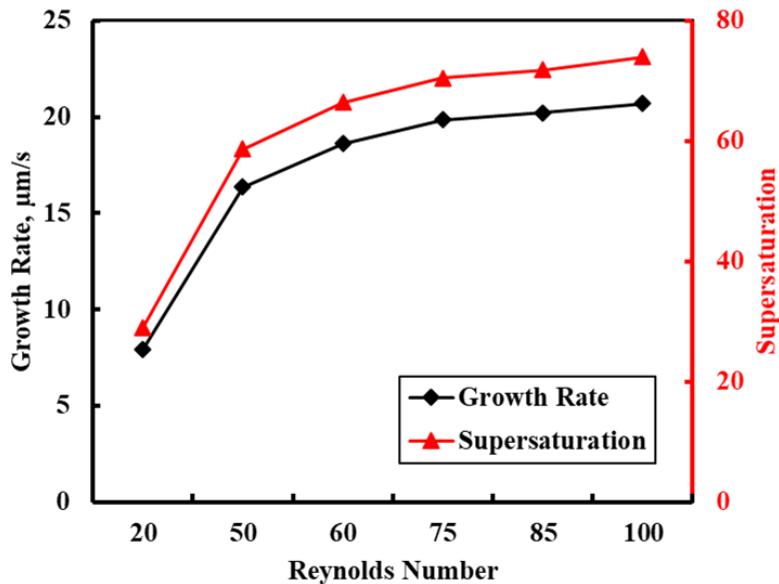
Table 5.10 Effect of Reynolds number on crystal size distribution

Reynolds Number	Mean Crystal Size (μm)	Crystal Yield	Variance
20	1.65	0.18	0.04
50	1.40	0.21	0.08
60	1.36	0.26	0.08
75	1.31	0.30	0.10
85	1.28	0.32	0.11
100	1.25	0.33	0.12

The effect of Re on growth rate, nucleation rate and supersaturation were predicted near the junction of the microchannel and shown in Figure 5.40. The nucleation rate was found to increase linearly with Re due to improved mixing. The growth rate and supersaturation found to increase sharply until Re = 50. For 50 < Re < 75 the change in growth rate reduced. For Re > 75, the change in growth rate was found to be very low.



(a)



(b)

Figure 5.40 The effect of Re on (a) nucleation rate and (b) growth rate

The crystal yield and pressure drop were compared at different Re in Figure 5.41. The slope of crystal yield was calculated to find out the rate at which it increasing with Re.

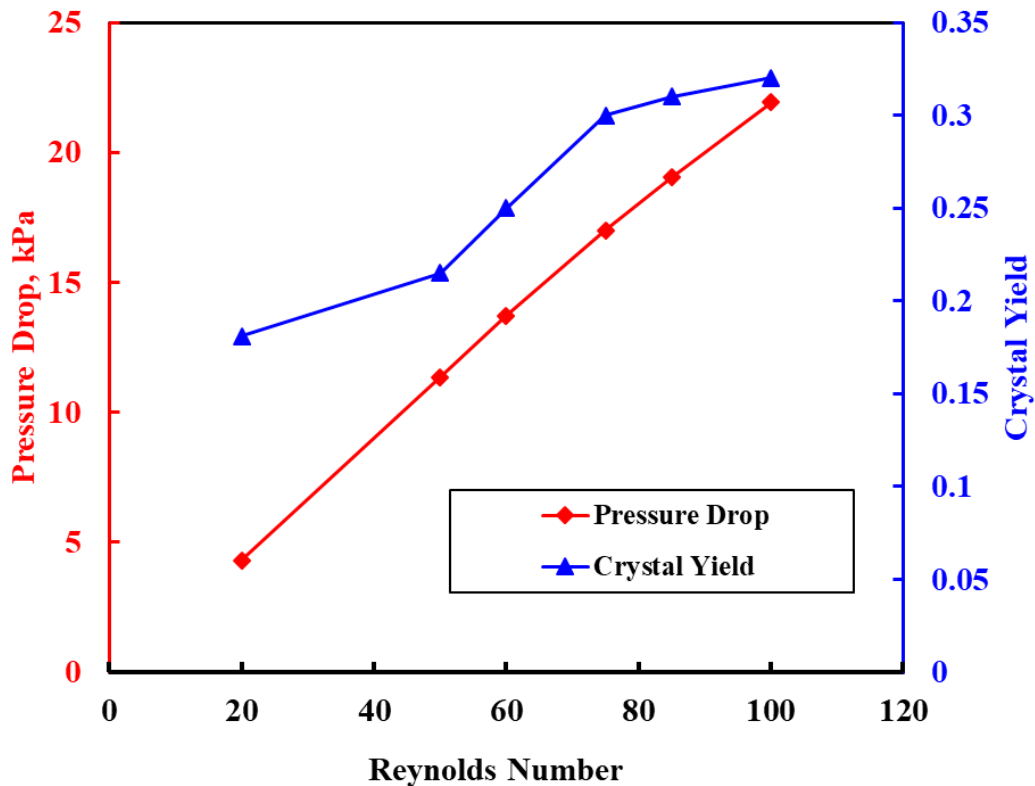


Figure 5.41 Effect of Re on pressure drop and crystal yield

For $Re < 50$, the slope was found to be 0.001 indicating low mixing. For $50 < Re < 75$, the slope was found to be 0.0036 indicating high rate of increase in crystal yield due to the transition of flow regime from vortex to engulfment flow. For $Re > 75$, the slope was found to be low again (0.0012). Thus, to achieve better crystal growth with narrow distribution $Re = 75$ is advantageous and was considered for further investigations.

Further, the effect of ethanol inlet mass fraction on CSD was predicted. The contours of spatial variation of supersaturation at different ethanol mass fractions are shown in Figure 5.42. The predicted crystal size distribution is depicted in Figure 5.43. It was observed that as the mass fraction of ethanol decreases the amount of crystals formed reduced significantly due to a decrease in the supersaturation. The CSD was also found to be broader as the ethanol mass fraction reduced. It was found that for ethanol mass fraction less than 0.8, no crystals were formed due to zero supersaturation

(Figure 5.42). It was also observed that the mean crystal size increased as the ethanol mass fraction was reduced. This was due to high growth rate and low nucleation rate.

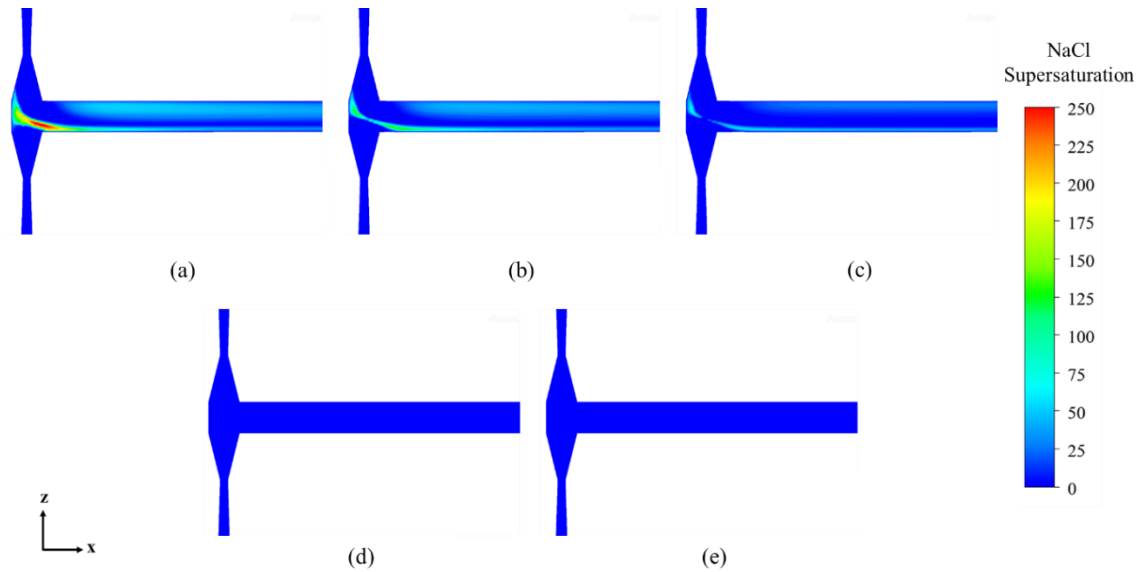


Figure 5.42 Contours of NaCl supersaturation for various ethanol mass fractions at $y = 100 \mu\text{m}$. (a) 1, (b) 0.9, (c) 0.8, (d) 0.7 and (e) 0.6.

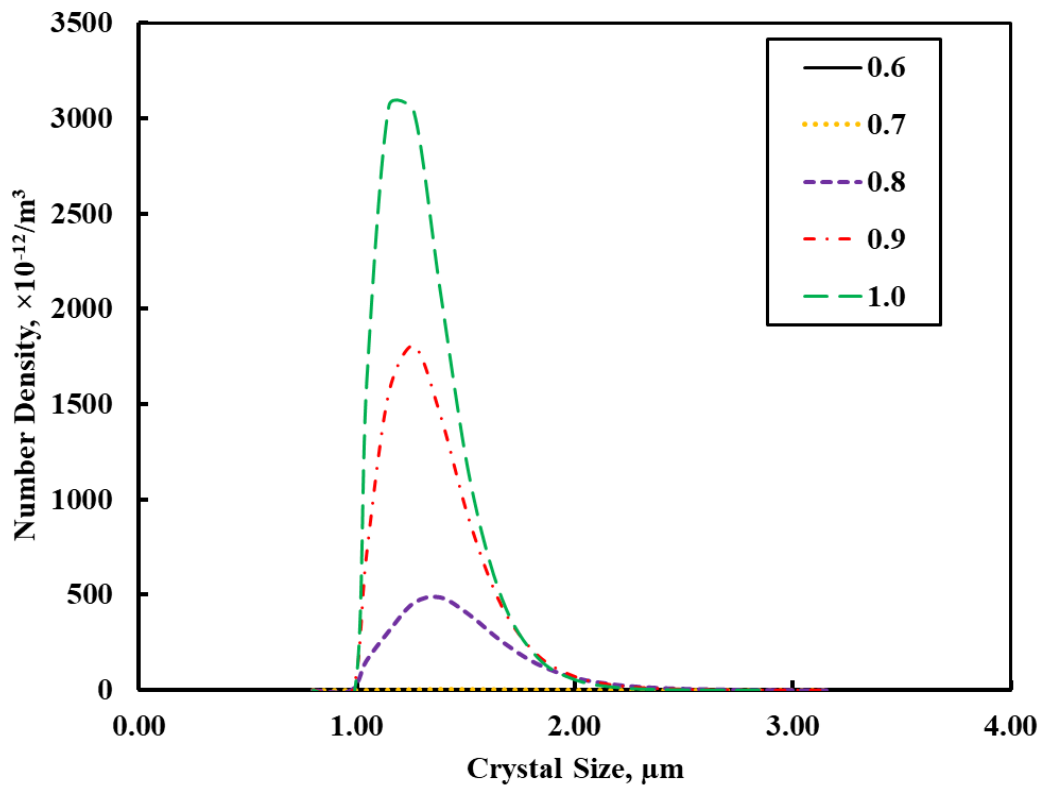


Figure 5.43 Effect of antisolvent mass fraction on crystal size distribution

The effect of ethanol inlet mass fraction on nucleation rate, growth rate and supersaturation is shown in Figure 5.44. It was observed that both nucleation rate and growth rate decreases sharply with a decrease in ethanol inlet mass fraction. This was due to a sharp reduction in the supersaturation inside the microchannel.

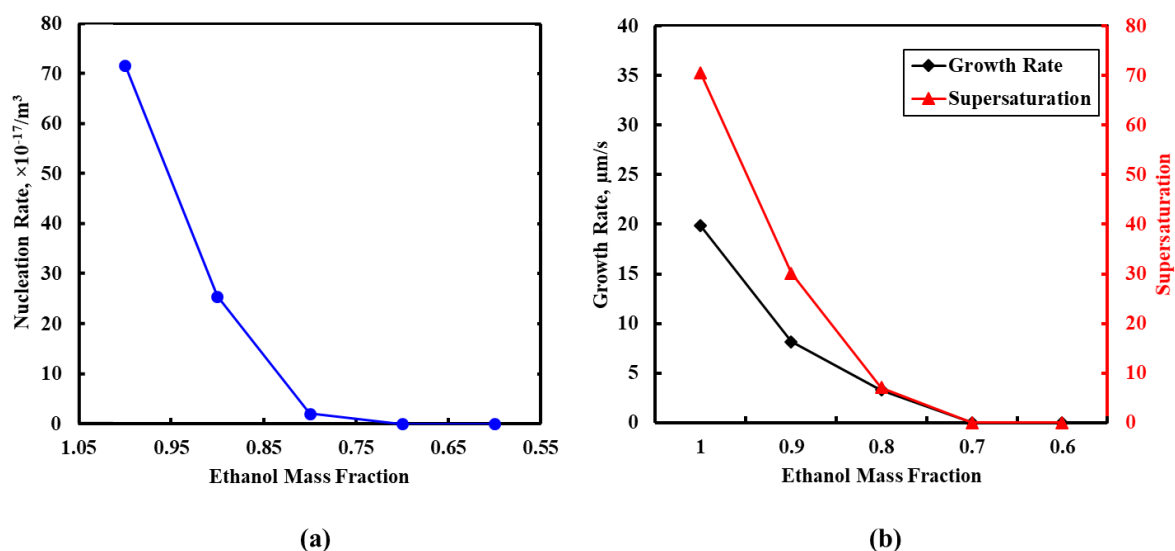


Figure 5.44 Effect of ethanol mass fraction on (a) nucleation rate and (b) growth rate

Further, the effect of ethanol mass fraction on mean crystal size, crystallized mass fraction and variance of crystal distribution is reported in Table 5.11. It was observed that no crystals were formed for mass fraction less than 0.8 and ethanol mass fraction of 1 supports higher crystallization rate and narrow CSD.

Table 5.11 Effect of antisolvent mass fraction on crystal size distribution

Ethanol Mass Fraction	Mean Crystal Size (µm)	Crystal Yield	Variance
1	1.31	0.30	0.10
0.9	1.35	0.19	0.08
0.8	1.42	0.06	0.07
0.7	0	0	0
0.6	0	0	0

5.5.3. Antisolvent Dosing

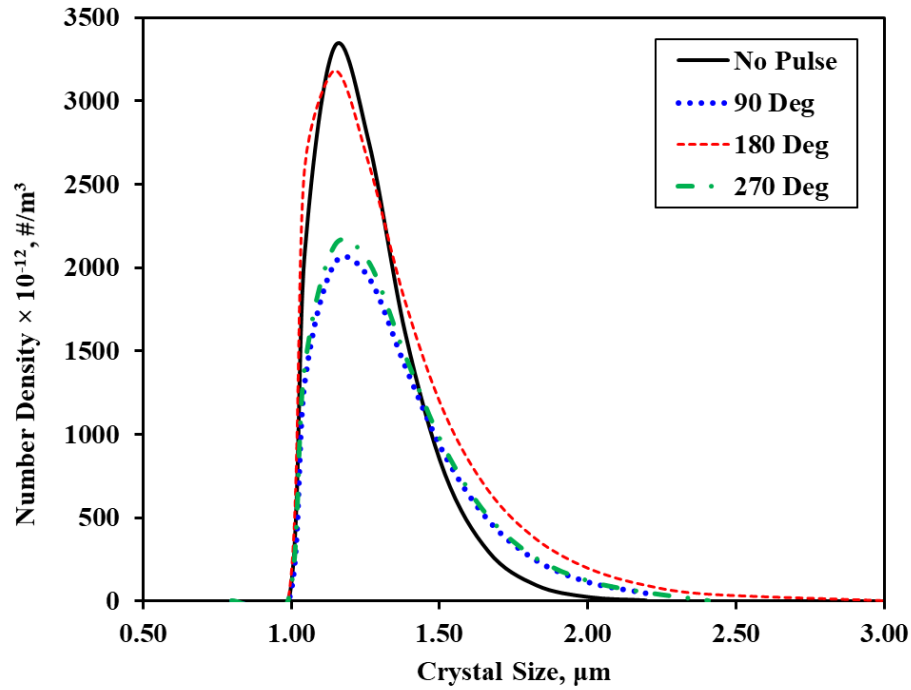
To improve crystal yield and CSD, pulse flow is introduced. The antisolvent and solution were dosed in pulse flow mode through the inlets. The effect of pulse flow parameters like phase lag between inlets, frequency of pulse flow and amplitude of pulse flow on CSD was investigated. To reduce the computational time, simulations were performed for a microchannel length of 2 cm instead of 5 cm. The effect of phase lag and frequency of sinusoidal pulse on crystal yield and CSD for microchannel length of 2 cm is depicted in Figure 5.45. The effect phase lag and frequency of pulse flow on crystal yield is shown in Table 5.12 and 5.13, respectively. It was observed that maximum crystal yield was obtained for the phase lag of 180° and frequency of 20 Hz.

Table 5.12 Effect of phase lag between inlet pulses on mean crystal size and yield

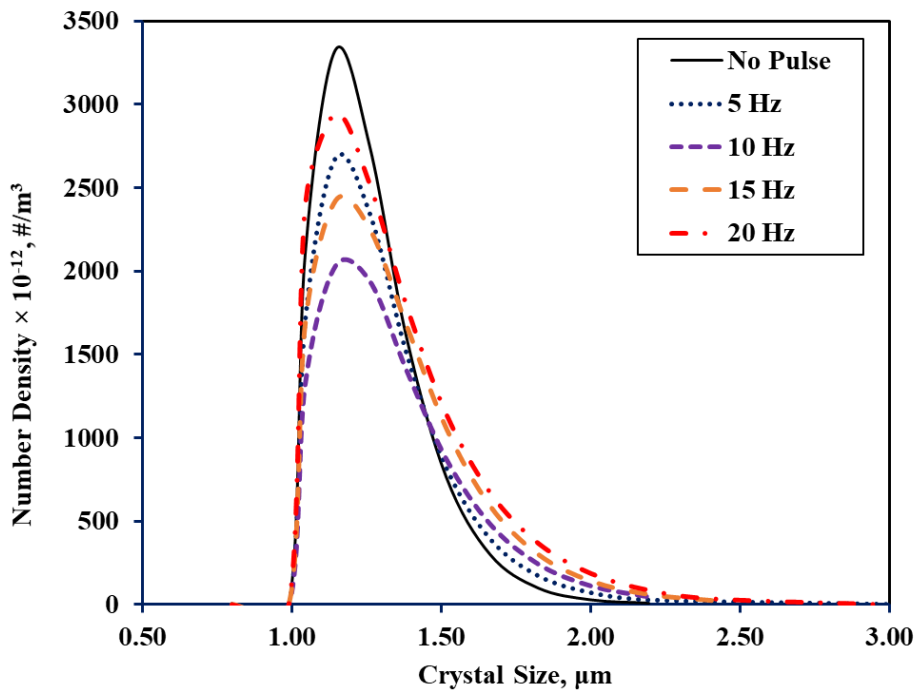
Phase lag	Mean Crystal Size (μm)	Crystal Yield
No Pulse	1.24	0.24
90°	1.30	0.26
180°	1.29	0.35
270°	1.30	0.27

Table 5.13 Effect of frequency of inlet pulses on mean crystal size and yield

Frequency (Hz)	Mean Crystal Size (μm)	Crystal Yield
No Pulse	1.24	0.24
5	1.27	0.25
10	1.30	0.26
15	1.29	0.28
20	1.29	0.35



(a)



(b)

Figure 5.45 The effect of (a) phase lag and (b) frequency of pulse on CSD

As the phase lag increases from 90° to 180° mixing among the fluid streams improved significantly leading to higher crystal yield. The crystal yield reduced as the phase lag was further increased to 270° due to low extent of mixing. The crystal yield

was found to increase with the frequency due to improved interaction among the inlet streams leading to higher supersaturation. The effect of amplitude on CSD is shown in Figure 5.46. Its effect on mean crystal size and yield is reported in Table 5.14. It was found that the crystal yield and mean crystal size did not change much with the amplitude. Thus, an amplitude of 0.05 m/s was considered to be optimum.

Table 5.14 Effect of amplitude of pulse flow on mean crystal size and yield

Amplitude (m/s)	Mean Crystal Size (μm)	Crystal Yield
No Pulse	1.24	0.24
0.02	1.25	0.25
0.05	1.26	0.26
0.07	1.29	0.28

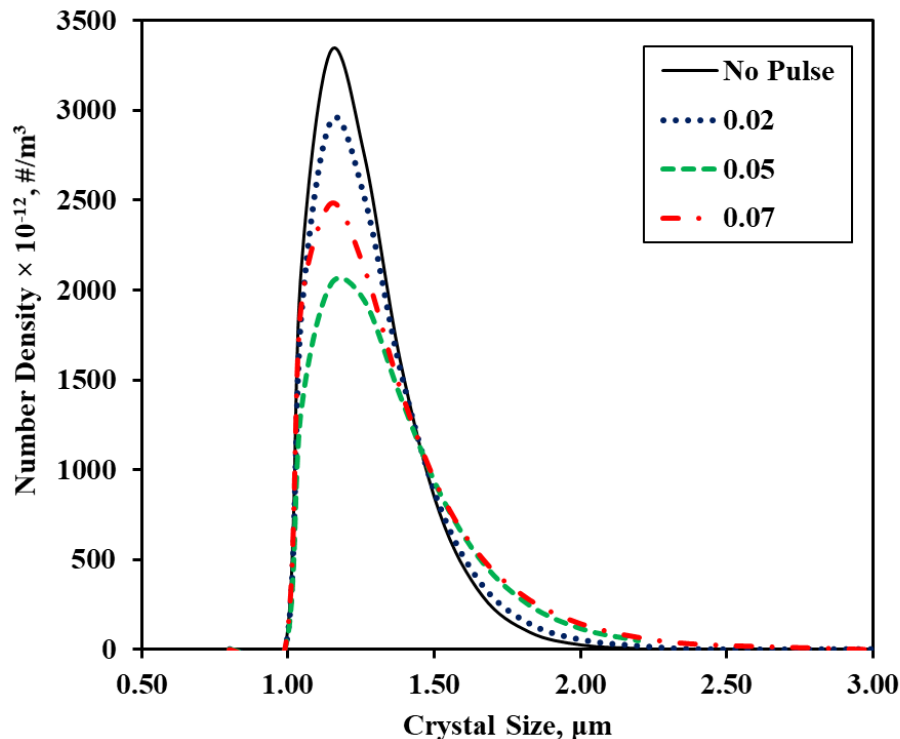
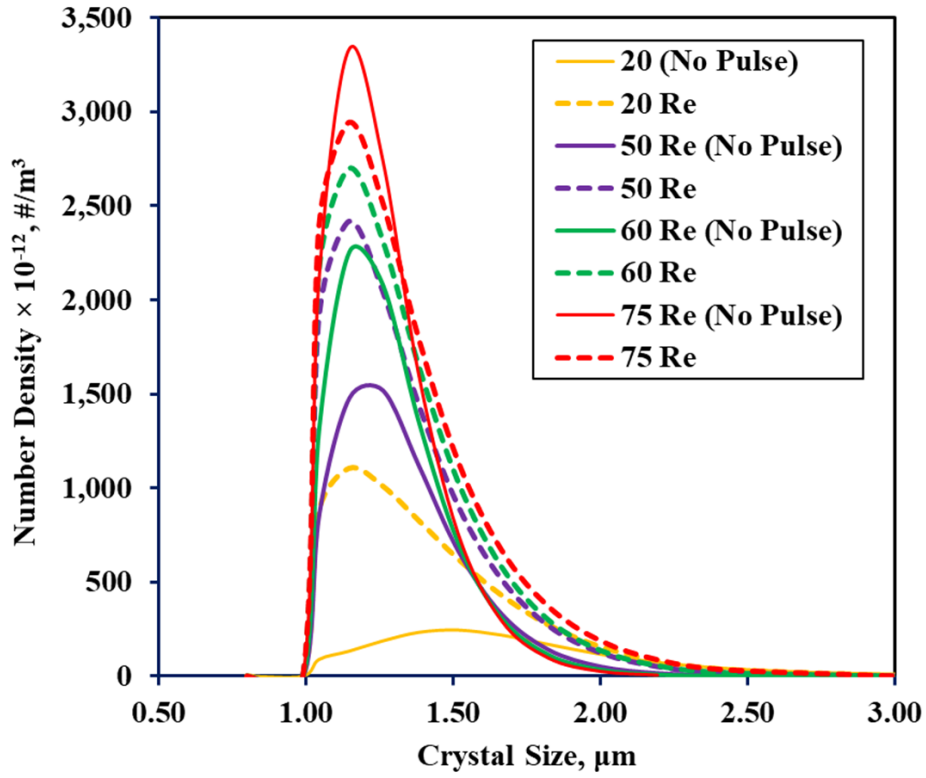
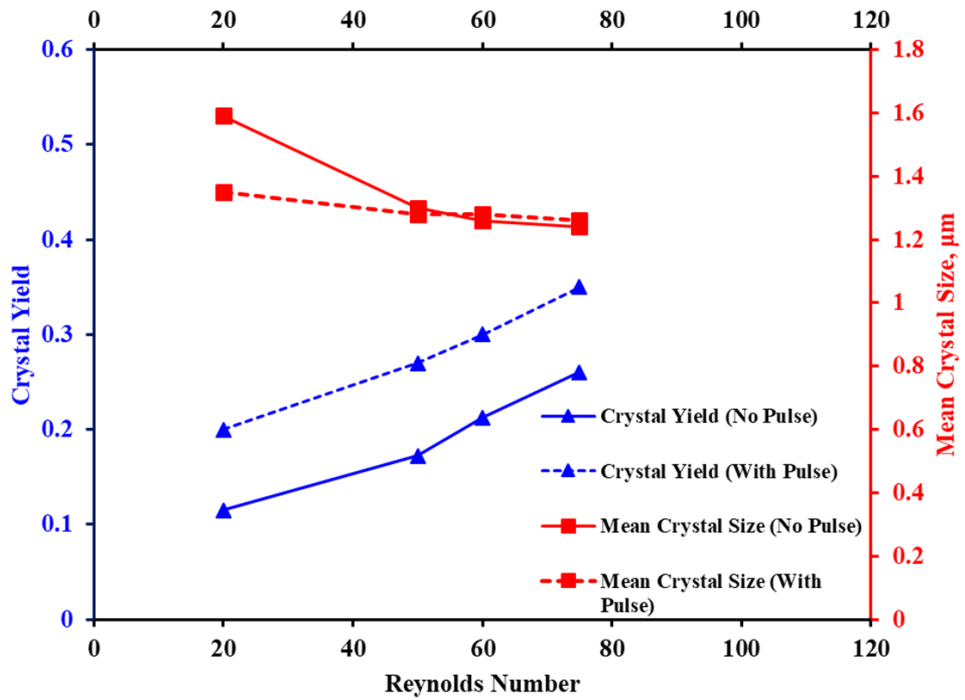


Figure 5.46 The effect of amplitude (m/s) of pulse on CSD

Further, the effect of the optimized pulse flow conditions on CSD at low Reynolds numbers was predicted and shown in Figure 5.47.



(a)



(b)

Figure 5.47 The effect of Re on (a) CSD; (b) crystal yield and mean crystal size at optimum pulse flow conditions

It was observed that the crystal yield has increased significantly and not much change in mean crystal size was observed at different Re [Figure 5.47 (b)]. The CSD was also found to be narrower at low Re under pulse flow conditions [Figure 5.47 (a)]. Thus, pulse flow has significantly improved crystal yield and CSD. These predictions can be used to design the crystallization process in the microcrystallizer. Based on the desired crystal size and time scale of the crystallization process, the operating conditions can be chosen. The crystals with minimum size can be obtained at high Re in engulfment flow. If the crystallization time scales are high, the crystallizer can be operated at low Re with pulsed flow so that narrow CSD can be obtained. The same operating conditions can be extended to nanoparticle synthesis in microchannels.

6. SUMMARY AND CONCLUSIONS

The hydrodynamics in a T-shaped microchannel was numerically investigated through CFD. The predicted spatial variation of velocity magnitude was analyzed to quantify the flow field and it was validated through flow visualization technique of ghost particle velocimetry (GPV). The numerical predictions were found to be comparable with experimental observations. To improve the flow field and mixing, various baffle configurations were introduced. To quantify the extent of mixing in our system, RTD and reaction studies were performed for various geometric modifications. Here model predictions were favourable with experimental observations. It was found that trapezoidal baffle configuration shows better mixing performance at lower Reynolds number ($Re < 60$) compared to other baffle configurations. The trapezoidal baffles also showed maximum reactant conversion. Since such baffle configurations will result in high pressure drop, inlet geometry modifications were proposed to improve mixing with low pressure drop.

The flow regimes prevailing in a T-shaped microchannel were numerically analyzed through CFD. The critical Reynolds number where the transition takes place among various flow regimes was identified by performing CFD simulations for a range of Re (1 - 400). The $Re_{critical}$ at which engulfment flow regime occurs was observed to be 300 and the predicted pressure drop was found to be very high. Hence, to overcome the high pressure drop and achieve engulfment flow at low Re , various convergent-divergent configurations (C/D ratios) were proposed at the inlets of the microchannel. The $Re_{critical}$ at which onset of engulfment flow occurs at low Re was found. This happens when the ratio of convergent to divergent length was 9:1. The mixing index was calculated to characterize the extent of mixing for various C/D ratios and the value was found to be maximum (0.7) when the ratio was 9:1. The observed hydrodynamic predictions were further verified by introducing passive tracer particles into the system and tracked in Lagrangian manner using discrete phase modelling (DPM) for various C/D ratios. The predicted particle trajectories were analyzed qualitatively by Poincaré map at a fixed Re (75) and quantified using Shannon's entropy. The magnitude of Shannon's entropy was found to be the highest when the C/D ratio was 9:1. The hydrodynamic predictions once again confirm the advantage of convergent to divergent length ratio of 9:1.

The consecutive-competitive reactions were considered to characterize micromixing performance for various flow regimes. This was quantified by calculating selectivity and yield of desired product R for various Re. The selectivity of R was found to be minimum in vortex flow regime and maximum in engulfment flow regime ($Re > 300$). The predicted pressure drop at this Re was found to be high. Hence to achieve engulfment flow at low Re, convergent-divergent type inlets were introduced in the microchannel. The engulfment flow was achieved at very low Re for convergent to divergent length ratio of 9:1 ($Re = 75$). The modified inlet configuration was found to significantly improve micromixing characteristics at low Re. Thus, the proposed convergent-divergent inlet configuration (9:1) support in enhancing the macromixing and micromixing performance of the microchannel.

The convergent-divergent inlet configuration (9:1) of T-shaped microchannel was exploited to perform antisolvent crystallization of NaCl in water-ethanol system. The CSD was predicted for different flow regimes and found that the distribution was broader at low Reynolds number due to low degree of mixing. As the Re was increased, crystallization rate increased as well as narrow CSD was obtained. The effect of ethanol inlet mass fraction on CSD was predicted. It was found that as the mass fraction was reduced the crystallization rate decreases as well as the CSD becomes broader. It was observed the mass fraction should be maintained above 0.8 since below that no crystals were formed due to low supersaturation. Further, pulse flow (sinusoidal) was introduced at the inlets to improve crystal yield and CSD. The effect of various pulse conditions on CSD, yield and mean crystal size was analyzed and optimum pulse conditions (phase lag = 180° , frequency = 20 Hz, amplitude = 0.05 m/s) were determined. The optimum pulse conditions helped in achieving higher crystal yield and narrow CSD at low Re as well. Thus, the modified microchannel along with pulse flow conditions have significantly improved microcrystallizer performance. The predicted results can be used to design a microcrystallizer to obtain desired crystal size and CSD. The proposed inlet design can also be extended to other multiphase applications in microchannels.

6.1. Future Scope

- The optimized geometry can be further extended to the synthesis of nano and microparticles in the microchannels.
- The proposed convergent - divergent inlet modifications can be applied to improve performance of other multiphase systems such as CO₂ absorption (gas - liquid), liquid-liquid extraction (liquid - liquid), photocatalysis (solid - liquid), etc.

REFERENCES

- Afzal, A., and Kim, K.-Y. (2012). “Passive split and recombination micromixer with convergent–divergent walls.” *Chemical Engineering Journal*, 203, 182–192.
- Alam, A., Afzal, A., and Kim, K. Y. (2014). “Mixing performance of a planar micromixer with circular obstructions in a curved microchannel.” *Chemical Engineering Research and Design*, 92(3), 423–434.
- Alam, A., and Kim, K. Y. (2012). “Analysis of mixing in a curved microchannel with rectangular grooves.” *Chemical Engineering Journal*, 181–182, 708–716.
- Ali, B. A., and Falleiro, L. H. (2022). “Effect of baffle configuration on performance of batch stirred vessel.” *Korean Journal of Chemical Engineering*, 39(5), 1146–1157.
- ANSYS FLUENT 19 User’s Guide. (2019). “Ansys Fluent Theory Guide.” ANSYS Inc, USA.
- Aoki, N., Fukuda, T., Maeda, N., and Mae, K. (2013). “Design of confluence and bend geometry for rapid mixing in microchannels.” *Chemical Engineering Journal*, 227, 198–202.
- Ashraf Ali, B., and Pushpavanam, S. (2011). “Analysis of unsteady gas–liquid flows in a rectangular tank: Comparison of Euler–Eulerian and Euler–Lagrangian simulations.” *International Journal of Multiphase Flow*, 37(3), 268–277.
- Bałdyga, J., and Pohorecki, R. (1995). “Turbulent micromixing in chemical reactors — a review.” *The Chemical Engineering Journal and the Biochemical Engineering Journal*, 58(2), 183–195.
- Bhagat, A. A. S., Kuntaegowdanahalli, S. S., and Papautsky, I. (2008). “Continuous particle separation in spiral microchannels using dean flows and differential migration.” *Lab on a Chip*, 8(11), 1906–1914.
- Bhagat, A. A. S., Peterson, E. T. K., and Papautsky, I. (2007). “A passive planar micromixer with obstructions for mixing at low Reynolds numbers.” *Journal of Micromechanics and Microengineering*, 17(5), 1017–1024.
- Bhamidi, V., Lee, S. H., He, G., Chow, P. S., Tan, R. B. H., Zukoski, C. F., and Kenis,

P. J. A. (2015). “Antisolvent Crystallization and Polymorph Screening of Glycine in Microfluidic Channels Using Hydrodynamic Focusing.” *Crystal Growth & Design*, 15(7), 3299–3306.

Bird, R. B., Stewart, W. E., and Lightfoot, E. N. (2006). *Transport Phenomena, 2nd Edition*. John Wiley & Sons, Inc, New York: John Wiley & Sons, Inc.

Bökenkamp, D., Desai, A., Yang, X., Tai, Y.-C., Marzluff, E. M., and Mayo, S. L. (1998). “Microfabricated Silicon Mixers for Submillisecond Quench-Flow Analysis.” *Analytical Chemistry*, 70(2), 232–236.

Bothe, D., Stemich, C., and Warnecke, H. J. (2006). “Fluid mixing in a T-shaped micro-mixer.” *Chemical Engineering Science*, 61(9), 2950–2958.

Bourne, J. R. (2003). “Mixing and the Selectivity of Chemical Reactions.” *Organic Process Research & Development*, 7(4), 471–508.

Burns, J. R., and Ramshaw, C. (1999). “Development of a microreactor for chemical production.” *Chemical Engineering Research and Design*, 77(3), 206–211.

Cai, G., Xue, L., Zhang, H., and Lin, J. (2017). “A review on micromixers.” *Micromachines*, 8(9).

Camesasca, M., Kaufman, M., and Manas-Zloczower, I. (2006). “Quantifying fluid mixing with the Shannon entropy.” *Macromolecular Theory and Simulations*, 15(8), 595–607.

Cheng, K., Liu, C., Guo, T., and Wen, L. (2019). “CFD and experimental investigations on the micromixing performance of single countercurrent-flow microchannel reactor.” *Chinese Journal of Chemical Engineering*, 27(5), 1079–1088.

Chu, G. W., Song, Y. H., Yang, H. J., Chen, J. M., Chen, H., and Chen, J. F. (2007). “Micromixing efficiency of a novel rotor–stator reactor.” *Chemical Engineering Journal*, 128(2), 191–196.

Doki, N., and Masaaki, M. (2021). “Pyrene Nanocrystals Crystallized by a Continuous Flow Microreactor.” *Journal of Materials Science and Chemical Engineering*, 09(11), 1–6.

Domingues, A. F., Poole, R. J., and Dennis, D. J. C. (2019). “Inertial instabilities in a

Multiphase Flow Characteristics in T-shaped Microchannels

microfluidic mixing-separating device.” *Physics of Fluids*, 31(7), 74101.

Du, L., Wang, Y. J., Lu, Y. C., and Luo, G. S. (2013). “Process intensification of BaSO₄ nanoparticle preparation with agitation of microbubbles.” *Powder Technology*, 247, 60–68.

Dundi, T. M., Raju, V. R. K., and Chandramohan, V. P. (2019). “Numerical evaluation of swirl effect on liquid mixing in a passive T-mixer.” *Australian Journal of Mechanical Engineering*, 1–15.

Duryodhan, V. S., Chatterjee, R., Govind Singh, S., and Agrawal, A. (2017). “Mixing in planar spiral microchannel.” *Experimental Thermal and Fluid Science*, 89, 119–127.

El-Kadi, J., Fenoaltea Pieche, E., Ko, S. W., and Torrente-Murciano, L. (2024). “Continuous synthesis of ruthenium nanoparticles with tuneable sizes using ruthenium nitrosyl nitrate precursor.” *Reaction Chemistry and Engineering*, 9(5), 1145–1153.

Fani, A., Camarri, S., and Salvetti, M. V. (2013). “Investigation of the steady engulfment regime in a three-dimensional T-mixer.” *Physics of Fluids*, 25(6), 64102.

Fatemi, N., Devos, C., Cordt, G. De, Gerven, T. Van, and Kuhn, S. (2019). “Effect of Sodium Dodecyl Sulfate on the Continuous Crystallization in Microfluidic Devices Using Microbubbles.” *Chemical Engineering & Technology*, 42(10), 2105–2112.

Ferziger, J. H., and Peric, M. (2002). *Computational Methods for Fluid Dynamics*. Springer-Verlag Berlin Heidelberg.

Fletcher, P. D. I., Haswell, S. J., Pombo-Villar, E., Warrington, B. H., Watts, P., Wong, S. Y. F., and Zhang, X. (2002). “Micro reactors: principles and applications in organic synthesis.” *Tetrahedron*, 58(24), 4735–4757.

Floyd, T. M., Losey, M. W., Firebaugh, S. L., Jensen, K. F., and Schmidt, M. A. (2000). “Novel Liquid Phase Microreactors for Safe Production of Hazardous Specialty Chemicals BT - Microreaction Technology: Industrial Prospects.” W. Ehrfeld, ed., Berlin, Heidelberg: Springer Berlin Heidelberg, 171–180.

Fogler, H. S. (2013). *Elements of Chemical Reaction Engineering*. Always Learning, Pearson Higher Education & Professional Group.

Fournier, M. C., Falk, L., and Villermaux, J. (1996). “A new parallel competing

reaction system for assessing micromixing efficiency—Experimental approach.” *Chemical Engineering Science*, 51(22), 5053–5064.

Fox, R. W., Pritchard, P. J., and McDonald, A. T. (2009). *Introduction To Fluid Mechanics, 7Th Ed.* Wiley India Pvt. Limited.

Galleguillos, H. R., Taboada, M. E., Graber, T. A., and Bolado, S. (2003). “Compositions, densities, and refractive indices of potassium chloride + ethanol + water and sodium chloride + ethanol + water solutions at (298.15 and 313.15) K.” *Journal of Chemical and Engineering Data*, 48(2), 405–410.

Galletti, C., Brunazzi, E., and Mauri, R. (2017). “Unsteady mixing of binary liquid mixtures with composition-dependent viscosity.” *Chemical Engineering Science*, 164, 333–343.

Galletti, C., Roudgar, M., Brunazzi, E., and Mauri, R. (2012). “Effect of inlet conditions on the engulfment pattern in a T-shaped micro-mixer.” *Chemical Engineering Journal*, 185–186(0), 300–313.

Gendron, P.-O., Avaltroni, F., and Wilkinson, K. J. (2008). “Diffusion Coefficients of Several Rhodamine Derivatives as Determined by Pulsed Field Gradient–Nuclear Magnetic Resonance and Fluorescence Correlation Spectroscopy.” *Journal of Fluorescence*, 18(6), 1093–1101.

Goulet, A., Glasgow, I., and Aubry, N. (2006). “Effects of microchannel geometry on pulsed flow mixing.” *Mechanics Research Communications*, 33(5), 739–746.

Graaf, S. van der, Nisisako, T., Schroeen, C. G. P. H., Sman, R. G. M. van der, and Boom, R. M. (2006). “Lattice Boltzmann Simulations of Droplet Formation in a T-Shaped Microchannel.” *Langmuir*, 22(9), 4144–4152.

Hafeez, S., Al-Salem, S. M., Bansode, A., Villa, A., Dimitratos, N., Manos, G., and Constantinou, A. (2022). “Computational Investigation of Microreactor Configurations for Hydrogen Production from Formic Acid Decomposition Using a Pd/C Catalyst.” *Industrial and Engineering Chemistry Research*, 61(4), 1655–1665.

Hessel, V., Hardt, S., Löwe, H., and Schönfeld, F. (2004). “Laminar mixing in different interdigital micromixers: I. Experimental characterization.” *AIChE Journal*, 49(3),

566–577.

Hisamoto, H., Saito, T., Tokeshi, M., Hibara, A., and Kitamori, T. (2001). “Fast and high conversion phase-transfer synthesis exploiting the liquid–liquid interface formed in a microchannel chip.” *Chemical Communications*, (24), 2662–2663.

HU, H., JIN, Z., DAWOUD, A., and JANKOWIAK, R. (2008). “Fluid Mixing Control Inside a Y-shaped Microchannel by Using Electrokinetic Instability.” *Journal of Fluid Science and Technology*, 3(2), 260–273.

Jang, J., Coquerel, G., Seo, T. S., Kim, W. S., and Park, B. J. (2024). “Microfluidic antisolvent crystallization for chiral symmetry breaking.” *Lab on a Chip*, 5055–5064.

Javaid, M. U., Cheema, T. A., and Park, C. W. (2018). “Analysis of Passive Mixing in a Serpentine Microchannel with Sinusoidal Side Walls.” *Micromachines*.

Jensen, K. F. (2017). “Flow chemistry—Microreaction technology comes of age.” *AIChE Journal*, 63(3), 858–869.

Kaabipour, S., and Hemmati, S. (2023). “Continuous, green, and room-temperature synthesis of silver nanowires in a helically-coiled millifluidic reactor.” *Colloids and Surfaces A: Physicochemical and Engineering Aspects*, 659(October 2022), 130806.

Kandlikar, S. G., and Grande, W. J. (2003). “Evolution of Microchannel Flow Passages - Thermohydraulic Performance and Fabrication Technology.” *Heat Transfer Engineering*, 24(1), 3–17.

Kashid, M. N., and Kiwi-Minsker, L. (2009). “Microstructured Reactors for Multiphase Reactions: State of the Art.” *Industrial & Engineering Chemistry Research*, 48(14), 6465–6485.

Kobayashi, J., Mori, Y., Okamoto, K., Akiyama, R., Ueno, M., Kitamori, T., and Kobayashi, S. (2004). “A Microfluidic Device for Conducting Gas-Liquid-Solid Hydrogenation Reactions.” *Science*, 304(5675), 1305–1308.

Kockmann, N. (2008). “Convective micromixers — design and industrial applications.” *Proceedings of the Institution of Mechanical Engineers, Part C: Journal of Mechanical Engineering Science*, 222(5), 807–816.

Kravtsova, A., Ianko, P., Meshalkin, Y., and Bilsky, A. (2018). “Influence of external

periodic perturbation on the flow in T-microchannel.” *AIP Conference Proceedings*, 2027(1), 40084.

Krishnaveni, T., Renganathan, T., Picardo, J. R., and Pushpavanam, S. (2017). “Numerical study of enhanced mixing in pressure-driven flows in microchannels using a spatially periodic electric field.” *Physical Review E*, 96(3), 1–15.

Krupa, K., Nunes, M. I., Santos, R. J., and Bourne, J. R. (2014). “Characterization of micromixing in T-jet mixers.” *Chemical Engineering Science*, 111, 48–55.

Lee, C.-Y., Chang, C.-L., Wang, Y.-N., and Fu, L.-M. (2011a). “Microfluidic Mixing: A Review.” *International Journal of Molecular Sciences*, 12(5), 3263–3287.

Lee, C. Y., Chang, C. L., Wang, Y. N., and Fu, L. M. (2011b). “Microfluidic mixing: A review.” *International Journal of Molecular Sciences*, 12(5), 3263–3287.

Lee, C. Y., Wang, W. T., Liu, C. C., and Fu, L. M. (2016). “Passive mixers in microfluidic systems: A review.” *Chemical Engineering Journal*, 288, 146–160.

Levenspiel, O. (1999). *Chemical Reaction Engineering*. John Wiley & Sons, New York: John Wiley & Sons, Ltd.

Li, S., Xu, J., Wang, Y., and Luo, G. (2008). “Controllable Preparation of Nanoparticles by Drops and Plugs Flow in a Microchannel Device.” *Langmuir*, 24(8), 4194–4199.

Lin, Y. C., Chung, Y. C., and Wu, C. Y. (2007). “Mixing enhancement of the passive microfluidic mixer with J-shaped baffles in the tee channel.” *Biomedical Microdevices*, 9(2), 215–221.

Liu, Y. Z., Kim, B. J., and Sung, H. J. (2004). “Two-fluid mixing in a microchannel.” *International Journal of Heat and Fluid Flow*, 25(6), 986–995.

Lobasov, A., and Minakov, A. (2017). “Density effect on the mixing efficiency and flow modes in T-shaped micromixers.” *MATEC Web Conf*, 115, 07002.

Lobasov, A. S., and Minakov, A. V. (2018). “Analyzing mixing quality in a T-shaped micromixer for different fluids properties through numerical simulation.” *Chemical Engineering and Processing - Process Intensification*, 124, 11–23.

Lobasov, A. S., Minakov, A. V., and Rudyak, V. Y. (2016). “Viscosity effect on the

flow patterns in T-type micromixers.” *Fluid Dynamics*, 51(3), 381–388.

Lobasov, A. S., Minakov, A. V, and Rudyak, V. Y. (2018). “Flow Modes of Non-Newtonian Fluids with Power-Law Rheology in a T-Shaped Micromixer.” *Theoretical Foundations of Chemical Engineering*, 52(3), 393–403.

Lobasov, A. S., and Shebeleva, A. A. (2017). “Initial temperatures effect on the mixing efficiency and flow modes in T-shaped micromixer.” *Journal of Physics: Conference Series*, 899, 22010.

M. Javaid Afzal, Tayyaba, S., M. Waseem Ashraf, M. I. Khan, Javaid, F., M. K. Basher, and M. Khalid Hossain. (2022). “A Review on Microchannel Fabrication Methods and Applications in Large-Scale and Prospective Industries.” *Evergreen*, 9(3), 764–808.

Maeki, M. (2019). “Chapter 4 - Microfluidics for pharmaceutical applications.” *Micro and Nano Technologies*, H. A. Santos, D. Liu, and H. B. T.-M. for P. A. Zhang, eds., William Andrew Publishing, 101–119.

Mansur, E. A., YE, M., WANG, Y., and DAI, Y. (2008). “A State-of-the-Art Review of Mixing in Microfluidic Mixers.” *Chinese Journal of Chemical Engineering*, 16(4), 503–516.

Mariotti, A., Galletti, C., Mauri, R., Salvetti, M. V., and Brunazzi, E. (2018). “Steady and unsteady regimes in a T-shaped micro-mixer: Synergic experimental and numerical investigation.” *Chemical Engineering Journal*, 341, 414–431.

Mariotti, A., Galletti, C., Mauri, R., Salvetti, M. V, and Brunazzi, E. (2021). “Effect of stratification on the mixing and reaction yield in a T-shaped micro-mixer.” *Physical Review Fluids*, 6(2), 24202.

Mawatari, K., Kazoe, Y., Aota, A., Tsukahara, T., Sato, K., and Kitamori, T. (2012). “Microflow Systems for Chemical Synthesis and Analysis: Approaches to Full Integration of Chemical Process.” *Journal of Flow Chemistry JFC*, 1(1), 3–12.

Medeiros de Souza, L., Temmel, E., Janiga, G., Seidel-Morgenstern, A., and Thévenin, D. (2021). “Simulation of a batch crystallizer using a multi-scale approach in time and space.” *Chemical Engineering Science*, 232, 116344.

Mehendale, S. S., Jacobi, A. M., and Shah, R. K. (2000). “Fluid Flow and Heat Transfer

at Micro- and Meso-Scales With Application to Heat Exchanger Design.” *Applied Mechanics Reviews*, 53(7), 175–193.

Melzig, S., Finke, J. H., Schilde, C., Vierheller, A., Dietzel, A., and Kwade, A. (2019). “Fluid mechanics and process design of high-pressure antisolvent precipitation of fenofibrate nanoparticles using a customized microsystem.” *Chemical Engineering Journal*, 371(April), 554–564.

Meng, L., Wu, D., He, X., and Zhuang, J. (2014). “Effect of surface tension on filling flow of carboxymethyl cellulose solution in microchannel.” *Materials Research Innovations*, 18(sup2), S2-1034-S2-1039.

Mersmann, A. (2001). *Crystallization Technology Handbook*. CRC Press.

Morshedaski, N., Raji, F., and Rahbar-Kelishami, A. (2023). “Optimization of Y and T-shaped microchannels for liquid–liquid extraction.” *Scientific Reports*, 13(1), 19708.

Nishat, S., Jafry, A. T., Martinez, A. W., and Awan, F. R. (2021). “Paper-based microfluidics: Simplified fabrication and assay methods.” *Sensors and Actuators B: Chemical*, 336, 129681.

Nishigaki, A., Maruyama, M., Numata, M., Kanzaki, C., Tanaka, S.-I., Yoshikawa, H. Y., Imanishi, M., Yoshimura, M., Mori, Y., and Takano, K. (2020). “Microflow system promotes acetaminophen crystal nucleation.” *Engineering in life sciences*, 20(9–10), 395–401.

Nisisako, T., and Torii, T. (2008). “Microfluidic large-scale integration on a chip for mass production of monodisperse droplets and particles.” *Lab on a Chip*, 8(2), 287–293.

O’Rourke P.J. (1981). “Collective Drop Effects on Vaporizing Liquid Sprays.” Princeton University.

Patil, G. A., Bari, M. L., Bhanvase, B. A., Ganvir, V., Mishra, S., and Sonawane, S. H. (2012). “Continuous synthesis of functional silver nanoparticles using microreactor: Effect of surfactant and process parameters.” *Chemical Engineering and Processing: Process Intensification*, 62, 69–77.

Rahman, M. T., and Rebrov, E. V. (2014). “Microreactors for Gold Nanoparticles

Synthesis: From Faraday to Flow.” *Processes*.

Raji, F., Kahani, A., Sahabi, M., Rahbar-kalishami, A., and Padrela, L. (2023). “Investigating the effectiveness of the main channel in microfluidic liquid-liquid extraction process.” *International Communications in Heat and Mass Transfer*, 147, 106986.

Ran, J., Wang, X., Liu, Y., Yin, S., Li, S., and Zhang, L. (2023). “Microreactor-based micro/nanomaterials: fabrication, advances, and outlook.” *Materials Horizons*, 10(7), 2343–2372.

Ravi Kumar, D. V, Prasad, B. L. V, and Kulkarni, A. A. (2012). “Segmented flow synthesis of Ag nanoparticles in spiral microreactor: Role of continuous and dispersed phase.” *Chemical Engineering Journal*, 192, 357–368.

Reddy Cherlo, S. K., and Pushpavanam, S. (2010). “Effect of depth on onset of engulfment in rectangular micro-channels.” *Chemical Engineering Science*, 65(24), 6486–6490.

Roberge, D. M., Ducry, L., Bieler, N., Cretton, P., and Zimmermann, B. (2005). “Microreactor Technology: A Revolution for the Fine Chemical and Pharmaceutical Industries?” *Chemical Engineering & Technology*, 28(3), 318–323.

Robertson, K., Seeberger, P. H., and Gilmore, K. (2022). “Rapid optimisation of API crystallisation in a segmented flow reactor with a continuous, variable temperature gradient.” *Reaction Chemistry and Engineering*, 8(1), 77–83.

Saffman, P. G. (1965). “The lift on a small sphere in a slow shear flow.” *Journal of Fluid Mechanics*, 22(2), 385–400.

Sahu, P. K., Golia, A., and Sen, A. K. (2012). “Analytical, numerical and experimental investigations of mixing fluids in microchannel.” *Microsystem Technologies*, 18(6), 823–832.

Sahu, P. K., Golia, A., and Sen, A. K. (2013). “Investigations into mixing of fluids in microchannels with lateral obstructions.” *Microsystem Technologies*, 19(4), 493–501.

Schejn, A., Frégnaux, M., Commenge, J.-M., Balan, L., Falk, L., and Schneider, R. (2014). “Size-controlled synthesis of ZnO quantum dots in microreactors.”

Nanotechnology, 25(14), 145606.

Shayesteh, H., Raji, F., and Kelishami, A. R. (2021). “Influence of the alkyl chain length of surfactant on adsorption process: A case study.” *Surfaces and Interfaces*, 22, 100806.

Shestakov, M. V. (2019). “Investigation of unsteady flow regime in a T-shaped channel by means of Time-Resolved PLIF and PIV techniques.” *Journal of Physics: Conference Series*, 1382, 12040.

Siconolfi, L., Camarri, S., and Salvetti, M. V. (2018). “T-mixer operating with water at different temperatures: Simulation and stability analysis.” *Physical Review Fluids*, 3(3), 33902.

Simmons, M. D., Jones, N., Evans, D. J., Wiles, C., Watts, P., Salamon, S., Escobar Castillo, M., Wende, H., Lupascu, D. C., and Francesconi, M. G. (2015). “Doping of inorganic materials in microreactors – preparation of Zn doped Fe₃O₄ nanoparticles.” *Lab on a Chip*, 15(15), 3154–3162.

Singh, K. K., Renjith, A. U., and Shenoy, K. T. (2015). “Liquid–liquid extraction in microchannels and conventional stage-wise extractors: A comparative study.” *Chemical Engineering and Processing: Process Intensification*, 98, 95–105.

Soleymani, A., Yousefi, H., Ratchananusorn, W., and Turunen, I. (2009). “Pressure drop in micro T-mixers.” *Journal of Micromechanics and Microengineering*, 20(1), 15029.

Soleymani, A., Yousefi, H., and Turunen, I. (2008). “Dimensionless number for identification of flow patterns inside a T-micromixer.” *Chemical Engineering Science*, 63(21), 5291–5297.

Srivastava, V. (2023). “Continuous-flow Synthesis of Ruthenium Nanoparticles using a Microreactor for the Selective Hydrogenation Reaction.” *Letters in Organic Chemistry*.

Suryawanshi, P. L., Gumfekar, S. P., Bhanvase, B. A., Sonawane, S. H., and Pimplapure, M. S. (2018). “A review on microreactors: Reactor fabrication, design, and cutting-edge applications.” *Chemical Engineering Science*, 189, 431–448.

Suryawanshi, P. L., Gumfekar, S. P., Kumar, P. R., Kale, B. B., and Sonawane, S. H. (2016). "Synthesis of ultra-small platinum nanoparticles in a continuous flow microreactor." *Colloid and Interface Science Communications*, 13, 6–9.

Valeh-e-Sheyda, P., Rahimi, M., Parsamoghadam, A., and Adibi, H. (2015). "Effect of microchannel confluence angles on size reduction of curcumin nano-suspension via liquid anti-solvent precipitation process." *Journal of the Taiwan Institute of Chemical Engineers*, 46, 65–73.

Voloshin, Y., Halder, R., and Lawal, A. (2007). "Kinetics of hydrogen peroxide synthesis by direct combination of H₂ and O₂ in a microreactor." *Catalysis Today*, 125(1), 40–47.

Wang, N., Jin, Y., Huang, T., Zhou, J., Zhang, Y., and Li, N. (2022). "Continuous production of 3,5,5-trimethylhexanoyl chloride and CFD simulations of single-phase flow in an advanced-flow reactor." *Journal of the Taiwan Institute of Chemical Engineers*, 138(2), 104465.

Wen, C.-Y., and Yu, Y. H. (1966). "Mechanics of fluidization." *Chemical Engineering Progress Symposium Series*, 62, 100–111.

Wu, B., Li, J., Li, C., He, J., and Luo, P. (2020). "Antisolvent crystallization intensified by a jet crystallizer and a method for investigating crystallization kinetics." *Chemical Engineering Science*, 211, 115259.

Wu, G., Zhou, H., and Zhu, S. (2007). "Precipitation of barium sulfate nanoparticles via impinging streams." *Materials Letters*, 61(1), 168–170.

Xu, L., Peng, J., Srinivasakannan, C., Chen, G., and Shen, A. Q. (2015). "Synthesis of copper nanocolloids using a continuous flow based microreactor." *Applied Surface Science*, 355, 1–6.

Yan, J., Lu, J., Qiu, J., Guo, Y., Zhao, S., and Bao, B. (2023). "Anti-solvent crystallization behavior of triphenylmethanol in a droplet-based microfluidic device." *Chemical Engineering Science*, 280(June), 118971.

Yang, M., Yang, L., Zheng, J., Hondow, N., Bourne, R. A., Bailey, T., Irons, G., Sutherland, E., Lavric, D., and Wu, K. J. (2021). "Mixing performance and continuous

production of nanomaterials in an advanced-flow reactor.” *Chemical Engineering Journal*, 412(January), 128565.

Yao, X., Zhang, Y., Du, L., Liu, J., and Yao, J. (2015). “Review of the applications of microreactors.” *Renewable and Sustainable Energy Reviews*, 47, 519–539.

Zanati, E. El, Abdallah, H., and Elnahas, G. (2017). “Micro-reactor for Non-catalyzed Esterification Reaction: Performance and Modeling.” *International Journal of Chemical Reactor Engineering*, 15(2).

Zhang, J., Liu, S., Cheng, C., Li, W., Xu, X., Liu, H., and Wang, F. (2019). “Investigation of three-dimensional flow regime and mixing characteristic in T-jet reactor.” *Chemical Engineering Journal*, 358, 1561–1573.

Zhang, J. S., Wang, K., Lu, Y. C., and Luo, G. S. (2010). “Characterization and modeling of micromixing performance in micropore dispersion reactors.” *Chemical Engineering and Processing: Process Intensification*, 49(7), 740–747.

Zhang, J., Wang, K., Teixeira, A. R., Jensen, K. F., and Luo, G. (2017). “Design and Scaling Up of Microchemical Systems: A Review.” *Annual Review of Chemical and Biomolecular Engineering*, 8(1), 285–305.

APPENDIX – I
ALGORITHMS

1. Hydrodynamics, Flow Regimes, Mixing & Reactions

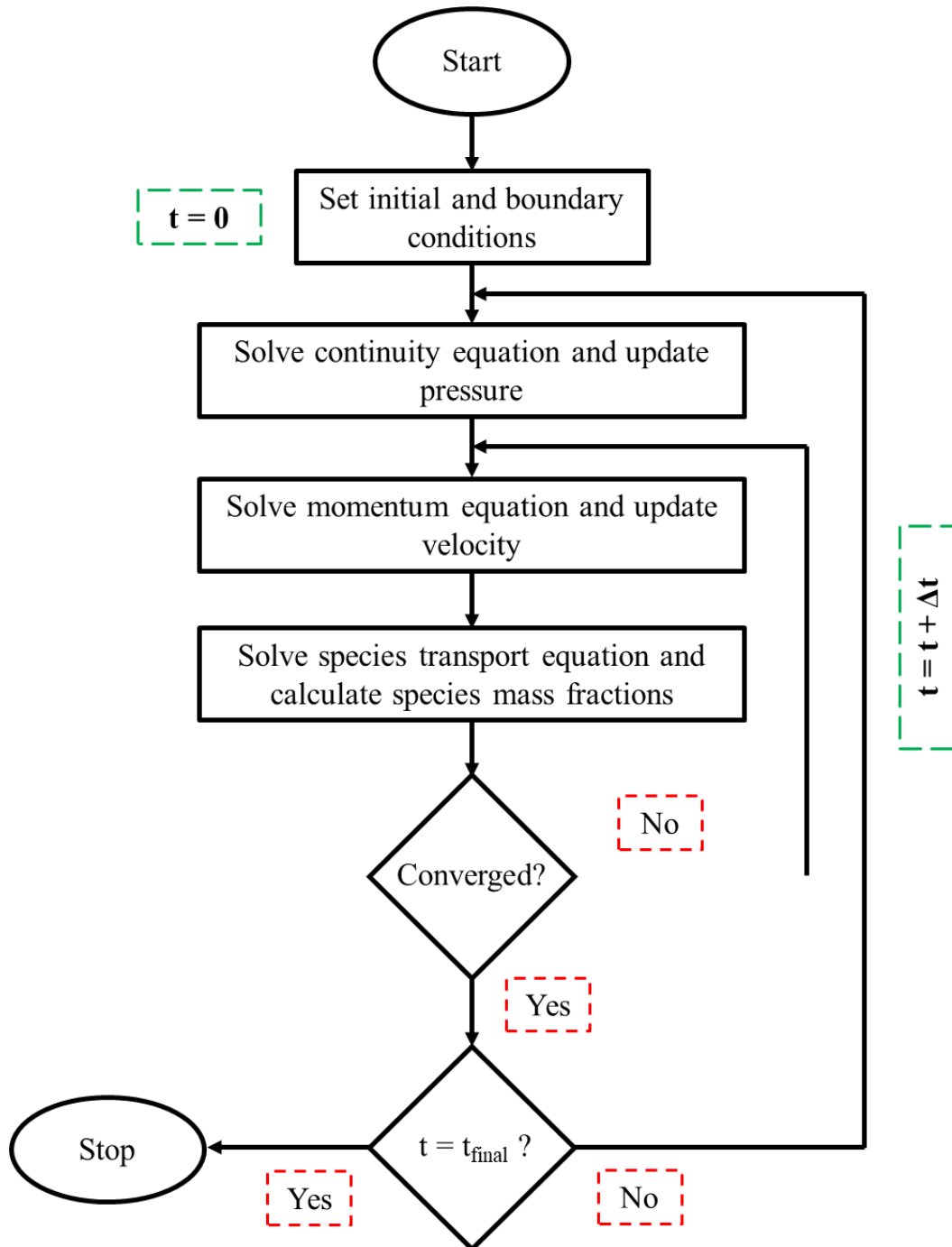


Figure A.1. Algorithm to solve hydrodynamics, single phase flow regimes, mixing and reactions in microchannels

2. Euler – Lagrangian Approach

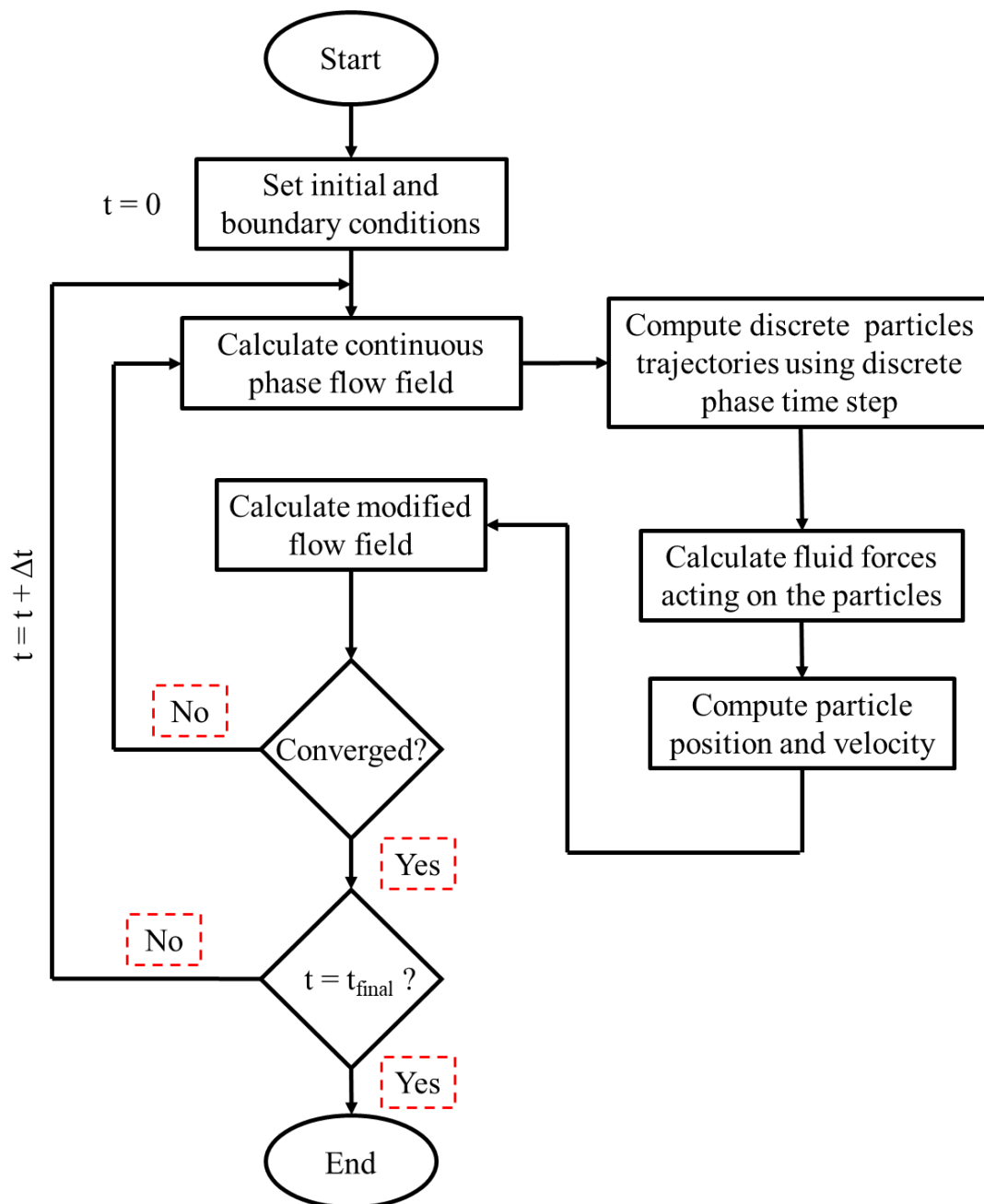


Figure A.2. Algorithm to solve discrete phase model (Euler-Lagrangian approach)

3. Antisolvent Crystallization

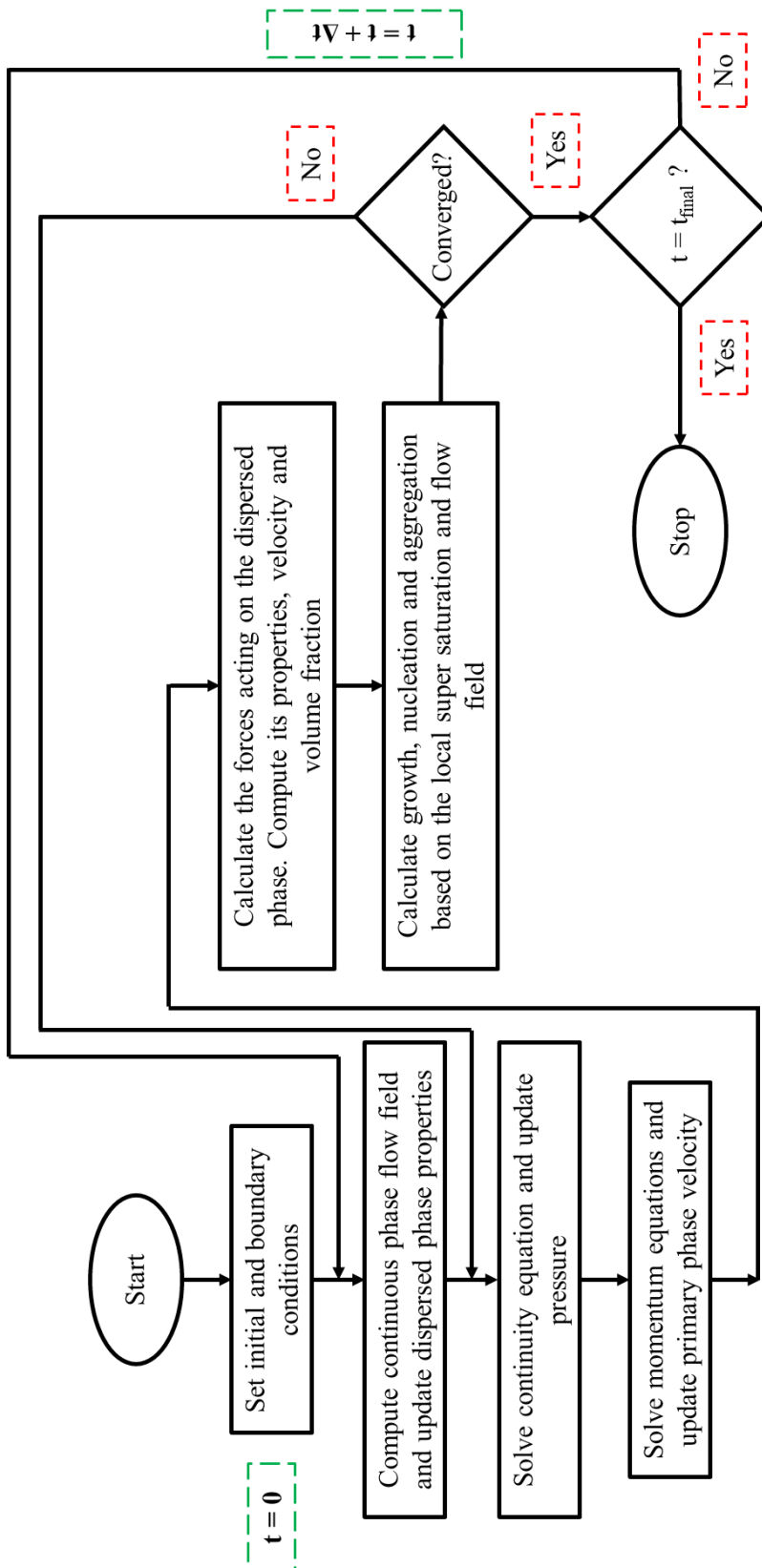


Figure A.3. Algorithm to simulate crystallization phenomena using coupled CFD - Population Balance Model approach

APPENDIX – II

USER DEFINED FUNCTIONS

1. User Defined Function to calculate nucleation rate of NaCl crystals

```

/*****
*/
#if !RP_HOST
#endif
#include "udf.h"
#include "sg_pb.h"
#include "sg_mphase.h"
DEFINE_PB_NUCLEATION_RATE(nuc_rate, cell, thread)
{
    real b = 3.606; /**nucleation exponent***/
    real kb = 1.328*pow(10,9);
    real x, nacl_mf, w_mf, ethanol_mf, sol, conc, SS, J;
    Thread *tc = THREAD_SUPER_THREAD(thread);
    Thread **pt = THREAD_SUB_THREADS(tc);
    Thread *tp = pt[P_PHASE];

    nacl_mf = C_YI(cell,tp,0); /**nacl mass fraction***/
    w_mf = C_YI(cell,tp,2); /**water mass fraction***/
    ethanol_mf = C_YI(cell,tp,1); /**anti-solvent mass fraction***/

    if (w_mf <= 0)
    {
        x = 0; /**ratio of ethanol to water in the mixture***/
        sol = 0.65; /**solubility on solvent-mixture basis***/
        conc = 1000*nacl_mf/(1-nacl_mf); /**concentration of
solute***/
        SS = (conc-sol)*(1+x);
    }
    else
    {
        x = ethanol_mf/w_mf; /**ratio of ethanol to water in the
mixture***/
        sol = 356.484*exp(-x/0.865); /**solubility on solvent-mixture
basis***/

```

```

        conc = 1000*nacl_mf/(1-nacl_mf); /**concentration of
solute***/
        SS = (conc-sol)*(1+x);
    }
/*****Nucleation Rate*****/
    if (SS <= 0)
    {
        J = 0;
    }
    else
    {
        J = (kb*pow(SS,b)*950)/(1+x);
    }
    C_UDMI(cell,tc,0) = J;
    C_UDMI(cell,tc,3) = nacl_mf;
    C_UDMI(cell,tc,4) = x;
    C_UDMI(cell,tc,5) = ethanol_mf;
    return J;
}

```

2. User Defined Function to calculate growth rate of NaCl crystals

```

/*****
*/
#if !RP_HOST
#endif
#include "udf.h"
#include "sg_pb.h"
#include "sg_mphase.h"
DEFINE_PB_GROWTH_RATE(growth_rate, cell, thread, d_1)
{
    real g = 1.079; /**growth exponent**/
    real kg = 1.885*pow(10,-7);
    real x, nacl_mf, w_mf, ethanol_mf, sol, conc, SS, G;
    Thread *tc = THREAD_SUPER_THREAD(thread);
    Thread **pt = THREAD_SUB_THREADS(tc);
    Thread *tp = pt[P_PHASE];

    nacl_mf = C_YI(cell,tp,0); /**nacl mass fraction**/
    w_mf = C_YI(cell,tp,2); /**water mass fraction**/
    ethanol_mf = C_YI(cell,tp,1); /**anti-solvent mass fraction**/

    if (w_mf <= 0)
    {
        x = 0; /**ratio of ethanol to water in the mixture**/
        sol = 0.65; /**solubility on solvent-mixture basis**/
        conc = 1000*nacl_mf/(1-nacl_mf); /**concentration of
solute**/
        SS = (conc-sol)*(1+x);
    }
    else
    {
        x = ethanol_mf/w_mf; /**ratio of ethanol to water in the
mixture**/
        sol = 356.484*exp(-x/0.865); /**solubility on solvent-mixture
basis**/
        conc = 1000*nacl_mf/(1-nacl_mf); /**concentration of
solute**/
        SS = (conc-sol)*(1+x);
    }
}

```

```
/******Growth Rate******/
if (SS <= 0)
{
    G = 0;
}
else
{
    G = kg*pow(SS,g); /**Growth Rate**/
}
C_UDMI(cell,tc,1) = G;
C_UDMI(cell,tc,2) = SS;
return G;
}
```

RESEARCH OUTCOME

SCI – Indexed Journal Publications

1. **Madana, V. S. T.** and Ashraf Ali, B. (2020). “Numerical investigation of engulfment flow at low Reynolds numbers in a T-shaped microchannel.” *Physics of Fluids*, 32(7), 72005. <https://doi.org/10.1063/5.0013957>. (IF - 4.6)
2. **Madana, V. S. T.** and Ashraf Ali, B. (2021). “Computational investigation of flow field, mixing and reaction in a T-shaped microchannel.” *Chemical Engineering Communications*, 208, 903–913. <https://doi.org/10.1080/00986445.2020.1865936>. (IF - 2.5)
3. **Madana, V. S. T.** and Ashraf Ali, B. “Computational investigation of flow regimes and micromixing in a T-shaped microchannel.” (Submitted to The Canadian Journal of Chemical Engineering)
4. **Madana, V. S. T.** and Ashraf Ali, B. “The effect of antisolvent dosing on crystallization of NaCl in a T-shaped microchannel - A numerical study.” (Submitted to Chemical Engineering Communications)

Conferences

1. **Madana, V. S. T.** and Ashraf Ali, B. “Computational investigation of liquid circulation and reaction in a microchannel.” RACEEE - 2019 held at SSN College of Engineering, Chennai, Tamil Nadu.
2. **Madana, V. S. T.** and Ashraf Ali, B. “The effect of antisolvent dosing on growth rate and CSD of NaCl crystals in a T-shaped microcrystallizer – A computational study.” ChEmference – 2023 held at BITS Pilani - Goa Campus, Goa.

BIODATA

Name : **VENKATA SAI TEJA MADANA**

PERSONAL DETAILS

Father's Name : Madana Srinivasa Rao

Date of Birth : 01-01-1992

Permanent Address : Door No. 96-6-205,
Nagarampalem, Guntur,
Andhra Pradesh, India - 522004.

Nationality : Indian

Email Id : saiteja.mv@gmail.com

Mobile : +91 7013022015

EDUCATIONAL QUALIFICATION

Ph.D. **Jul 2017 - Jul 2024**

Chemical Engineering, CGPA - 7.2

National Institute of Technology Karnataka, Surathkal, Karnataka.

M.Tech. **Aug 2013 - May 2015**

Chemical Engineering, CGPA - 8.13

Birla Institute of Technology and Science, Pilani, Rajasthan.

B.Tech. **Sep 2009 - May 2013**

Chemical Engineering, Percentage - 79.3%

Jawaharlal Nehru Technological University, Anantapur, Andhra Pradesh.

PROFESSIONAL EXPERIENCE

Research Scientist

July 2024 - Present

India Centre for Lab Grown Diamond (InCent – LGD), IIT Madras, Chennai, Tamil Nadu.

PUBLICATIONS

International Journals (SCI Indexed) : 3 (2 under review)

Conference Proceedings : 2

DECLARATION

I hereby declare that the information provided above is true to the best of my knowledge.

Venkata Sai Teja Madana